

STRUCTURAL DESIGN, ANALYSIS AND COMPOSITE MANUFACTURING
APPLICATIONS FOR A TACTICAL UNMANNED AIR VEHICLE

A THESIS SUBMITTED TO
THE GRADUATE SCHOOL OF NATURAL AND APPLIED SCIENCES
OF
MIDDLE EAST TECHNICAL UNIVERSITY

BY

SERCAN SOYSAL

IN PARTIAL FULFILLMENT OF THE REQUIREMENTS
FOR
THE DEGREE OF MASTER OF SCIENCE
IN
AEROSPACE ENGINEERING

MAY 2008

Approval of the thesis:

**STRUCTURAL DESIGN, ANALYSIS AND COMPOSITE MANUFACTURING
APPLICATIONS FOR A TACTICAL UNMANNED AIR VEHICLE**

submitted by **SERCAN SOYSAL** in partial fulfillment of the requirements for the degree of **Master of Science in Aerospace Engineering Department, Middle East Technical University** by,

Prof. Dr. Canan Özgen
Dean, Graduate School of **Natural and Applied Sciences**

Prof. Dr. İsmail Hakkı Tuncer
Head of Department, **Aerospace Engineering**

Assoc. Prof. Dr. Altan Kayran
Supervisor, **Aerospace Engineering Dept., METU**

Prof. Dr. Nafiz Alemdaroğlu
Co-Supervisor, **Aerospace Engineering Dept., METU**

Examining Committee Members:

Asst. Prof. Dr. Melin ŞAHİN
Aerospace Engineering Dept., METU

Assoc. Prof. Dr. Altan Kayran
Aerospace Engineering Dept., METU

Prof. Dr. Nafiz Alemdaroğlu
Aerospace Engineering Dept., METU

Dr. Güçlü Seber
Aerospace Engineering Dept., METU

Dr. Cevher Levent Ertürk,
Senior Chief Researcher, TÜBİTAK - UZAY

Date:

I hereby declare that all information in this document has been obtained and presented in accordance with academic rules and ethical conduct. I also declare that, as required by these rules and conduct, I have fully cited and referenced all material and results that are not original to this work.

Name, Last Name : **Sercan SOYSAL**

Signature :

ABSTRACT

STRUCTURAL DESIGN, ANALYSIS AND COMPOSITE MANUFACTURING APPLICATIONS FOR A TACTICAL UNMANNED AIR VEHICLE

Soysal, Sercan

M.Sc., Department of Aerospace Engineering

Supervisor : Assoc. Prof. Dr. Altan KAYRAN

Co-Supervisor: Prof. Dr. Nafiz ALEMDAROĞLU

May 2008, 122 pages

In this study structural design, analysis and composite manufacturing applications for a tactical UAV, which was designed and manufactured in Aerospace Engineering Department of Middle East Technical University (METU), is introduced. In order to make an accurate structural analysis, the material and loading is modeled properly. Computational fluid dynamics (CFD) was used to determine the 3D pressure distribution around the wing and then the nodal forces were exported into the finite element program by means of interpolation from CFD mesh to finite element mesh. Composite materials which are mainly used in METU TUAV are woven fabrics which are wetted with epoxy resin during manufacturing. In order to find the elastic constants of the woven fabric composites, a FORTRAN code is written which utilizes point-wise lamination theory. After the aerodynamic load calculation and material characterization steps, linear static and dynamic analysis of the METU TUAV's wing is performed and approximate torsional divergence speed is calculated based on a

simplified approach. Lastly, co-cured composite manufacturing of a multi-cell box structure is explained and a co-cured multi-cell box beam is manufactured.

Keywords: UAV, woven fabric composites, structural analysis, co-cured composite manufacturing

ÖZ

KOMPOZİT BİR TAKTİK İNSANSIZ HAVA ARACININ YAPISAL TASARIM, ANALİZ VE KOMPOZİT ÜRETİM UYGULAMALARI

Soysal, Sercan

Yüksek Lisans, Havacılık ve Uzay Mühendisliği Bölümü

Tez Yöneticisi : Doç. Dr. Altan KAYRAN

Ortak Tez Yöneticisi: Prof. Dr. Nafiz ALEMDAROĞLU

Mayıs 2008, 122 sayfa

Bu tez kapsamında bir taktik insansız hava aracının yapısal tasarımı ve analizi yapılmıştır. İncelenen taktik insansız hava aracı (Taktik İHA) Orta Doğu Teknik Üniversitesi (ODTÜ) Havacılık ve Uzay Mühendisliği'nde tasarlanmış ve üretilmiştir. Hava aracının yapısal analizini doğru yapabilmek için malzeme ve yükleme doğru bir şekilde modellenmelidir. Kanat üstündeki yükler, hesaplamalı akışkanlar dinamiği (HAD) yöntemiyle bulunmuş daha sonra HAD çözüm aşında bulunan yükler sonlu elemanlar analizi çözüm aşına ara değer bulma yöntemiyle aktarılmıştır. ODTÜ Taktik İHA'sında en çok kullanılan kompozit malzeme üretim sırasında epoksi reçine ile ıslatılan örgülü kumaş formundadır. Örgülü kumaş kompozit malzemelerin elastik sabitlerini bulmak için noktasal tabaka teorisi kullanarak hesaplama yapan bir FORTRAN kodu yazılmıştır. Yük dağılımının ve malzeme özelliklerinin bulunmasından sonra, kanadın statik ve dinamik yapısal analizleri gerçekleştirilmiş ve uçağın burulma iraksama hızı yaklaşık olarak basit bir metot kullanılarak

bulunmuştur. Bunlara ek olarak, bileşik kür olmuş çok hücreli kompozit bir kutu üretiminin detayları açıklanmış ve üretimi gerçekleştirilmiştir.

Anahtar Kelimeler: İHA, örgülü kumaş kompozit malzemeler, yapısal analiz, bütünleşik kompozit yapı üretimi

to my family...

ACKNOWLEDGEMENTS

I would like to express the deepest appreciation to Assoc. Prof. Dr. Altan Kayran for his valuable efforts throughout my thesis. His support and guidance helped me in every step of this thesis. One simply could not wish for a better or friendlier supervisor. I am also grateful to my co-supervisor Prof. Dr. Nafiz Alemdarođlu, supervisor of METU UAV Project, for financial and facility support.

I wish to state my special thanks to the other members of the UAV project, Fikri Akçalı, Volkan Kargın, Serhan Yüksel and Hüseyin Yiđitler for their incredible efforts throughout the project. I also thank to technician Murat Ceylan for his efforts during composite manufacturing steps.

I would like to thank to Buşra Akay and Özgür Demir for their guidance during CFD analyses. I definitely learned a lot from them.

I appreciate the useful advices of Levent Gür from LTG Composites about VARTM manufacturing technique.

I also thank to Prof. Dr. Zeki Kaya for providing the digital microscope in the Department of Biological Sciences of METU.

I would like to thank my dearest friends Ođuzhan Ayısıt, Tahir Turgut and Emrah Konokman for providing me such a warm home atmosphere. It is also a fact that their critics about the thesis make it better.

Finally, I would like to express my sincere thanks to my family for their thrust and understanding.

TABLE OF CONTENTS

ABSTRACT	iv
ÖZ	vi
ACKNOWLEDGEMENTS	ix
TABLE OF CONTENTS.....	x
LIST OF TABLES	xiii
LIST OF FIGURES	xv
CHAPTERS	
1. INTRODUCTION AND LITERATURE REVIEW	1
1.1. Introduction to Tactical Unmanned Air Vehicles	1
1.2. METU Tactical UAV (TUAV).....	3
2. DESIGN AND MANUFACTURING OF THE METU TUAV	4
2.1. Design Features of METU TUAV.....	4
2.2. Structural Design of METU TUAV	6
2.3. Manufacturing Methodology of METU TUAV	10
2.3.1. Preparation of Molds	11
2.3.2. Manufacturing of the Wing	14

3. DETERMINATION OF AERODYNAMIC LOADING BY COMPUTATIONAL FLUID DYNAMICS.....	23
3.1. Introduction	23
3.2. Generation of the Computational Mesh	24
3.3. CFD Analysis	26
3.4. Interpolation of Aerodynamic Forces From CFD Mesh to FE Mesh	29
4. MECHANICAL PROPERTIES OF WOVEN FABRIC COMPOSITES	33
4.1. Introduction	33
4.2. The Geometry of the Woven Fabrics	34
4.3. Elastic Constants of Woven Fabrics	37
4.3.1. Introduction to Modeling of Elastic Analysis of Woven Fabrics	37
4.3.2. Material Model of the Woven Fabrics Used in METU TUAV	38
4.3.2.1. Micro Level Analysis.....	39
4.3.2.2. Mini Level Analysis.....	44
4.3.2.2.1. Geometric Model of the Unit Cell	44
4.3.2.2.2. Point-Wise Lamination Theory.....	51
4.3.2.2.3. Averaging Schemes for the Stiffness Matrices.....	56
4.3.2.2.3.1. Series-Parallel Model.....	56
4.3.2.2.3.2. Parallel-Series Model.....	57
4.3.2.2.3.3. Series-Series Model	58

4.3.2.2.3.4. Parallel-Parallel Model	59
4.3.2.2.4. Results of the Mini-Level Analysis	60
5. STRUCTURAL ANALYSIS OF METU TUAV'S WING WITH FEA.....	62
5.1. Introduction	62
5.2. Description of the Model.....	63
5.3. Boundary Condition Selection	66
5.4. Material Properties	69
5.5. Static Analysis of METU TUAV's Wing	71
5.5.1. Results of Static Analysis at Positive Low Angle of Attack Case	72
5.5.2. Results of Static Analysis at Positive High Angle of Attack Case....	79
5.6. Dynamic Analysis of METU TUAV's Wing	85
5.7. Simplified Torsional Divergence Speed Calculation.....	89
6. INTEGRAL MANUFACTURING OF A TORQUE BOX	95
6.1. Introduction	95
6.2. Vacuum-Assisted Resin Transfer Molding (VARTM)	97
6.3. Manufacturing of a Cocured Composite Box	99
CONCLUSION.....	106
REFERENCES	109
APPENDIX	112
A. INTERPOLATION OF CFD DATA INTO FINITE ELEMENT MODEL.....	112

LIST OF TABLES

Table 1: Classification of UAVs	2
Table 2: Specifications of METU TUAV	5
Table 3: Properties of volume mesh for PLA and PHA cases.....	24
Table 4: Results of CFD analysis.....	28
Table 5: CFD case study	29
Table 6: Effect of interpolation to the force resultants	32
Table 7: Effect of FE mesh size to the force resultants after interpolation	32
Table 8: Comparison of properties for weave styles.....	36
Table 9: Geometric properties of unit cells of the woven fabrics which are used in METU TUAV	51
Table 10: Mechanical properties of fiber and matrix materials used in METU TUAV	61
Table 11: Elastic Constants for T300/Epoxy WF Composite	61
Table 12: Property table of the FE model.....	64
Table 13: Results for different mesh sizes	66
Table 14: Boundary condition cases for front and rear spar connection blocks	69
Table 15: Results for different boundary condition cases	69

Table 16: Mechanical properties of isotropic materials used in METU TUAV	70
Table 17: Mechanical properties of 2D orthotropic materials.....	70
Table 18: Comparison of results from unit cell analysis and values from literature..	71
Table 19: MoS value for front spar in PLA case	72
Table 20: MoS value for rear spar in PLA case.....	74
Table 21: MoS values for upper skin layers in PLA case.....	75
Table 22: MoS values for lower skin layers in PLA case	75
Table 23: MoS values for webs and ribs in PLA case	77
Table 24: MoS value for front spar in PHA case	79
Table 25: MoS value for rear spar in PHA case	80
Table 26: MoS values for skin layers in PHA case.....	81
Table 27: MoS values for webs and ribs in PHA case.....	83
Table 28: Comparison of peak stress and displacements for PLA and PHA cases .	85
Table 29: First three normal modes and their frequency	86

LIST OF FIGURES

Figure 1: Examples for Different UAV Types: (a) Micro, (b) Mini, (c) Tactical, (d) Medium Altitude Long Endurance (MALE), (e) High Altitude Long Endurance (HALE)	2
Figure 2: Three View of METU TUAV	6
Figure 3: V-n diagram of METU TUAV	10
Figure 4: E-Glass coated polystyrene foam used in the manufacturing of the METU TUAV wing.....	11
Figure 5: Male mold ready to be used as reference for female mold manufacturing	12
Figure 6: Covering the male mold with tool resin.....	13
Figure 7: Reinforcing the mold with woven E-glass woven fabric	13
Figure 8: Female wing molds.....	14
Figure 9: Manufacturing steps of the wing skins: (a) First e-glass layer, (b) Rohacell foam layer, (c) Last e-glass layer, (d) Spar flanges in the lower skin.....	15
Figure 10: Positioning the spars.....	16
Figure 11: Allodized aluminum section of the rear spar.....	18
Figure 12: Hornbeam section of the front spar	19
Figure 13: Manufacturing of the spars: (a) Laying up the carbon woven fiber,	20

Figure 14: Assembling the structural part of the wing: (a) Ribs, (b) Adhesive layer, (c) Releasing the wing from the mold, (d) Wings after released from female molds	22
Figure 15: Mesh around the root section of wing	25
Figure 16: Boundary Conditions for CFD Analysis	26
Figure 17: C_p distribution around root section of the wing	27
Figure 18: C_p distribution on wing surfaces	28
Figure 19: Comparison of CFD and FEA meshes	30
Figure 20: Unit cell geometry	34
Figure 21: Plain weave fabric	35
Figure 22: Twill weave fabric	35
Figure 23: Satin weave fabric	36
Figure 24: Methodology of analysis	38
Figure 25: CCA model geometry	39
Figure 26: Comparison of CCA and RoM for E_y	43
Figure 27: Comparison of CCA and RoM for G_{xy}	43
Figure 28: Comparison of CCA and RoM for v_{xy}	44
Figure 29: Dimensions in the unit cell	45
Figure 30: Digital microscope in the Department of Biological Sciences	50
Figure 31: Photograph of T300 Carbon/Epoxy under microscope	50
Figure 32: Color coded zones in wing model	63

Figure 33: Detailed view of spar-body connection areas	64
Figure 34: The detail of front spar connection in FE model	65
Figure 35: Boundary conditions for wing connection blocks	67
Figure 36: The finite element modeling of the tail boom	72
Figure 37: von Mises stress contours for front spar core material in PLA case	73
Figure 38: von Mises stress contours for rear spar in PLA case.....	74
Figure 39: von Mises stress contours for skin in PLA case	76
Figure 40: von Mises stress contours for ribs and webs in PLA case	78
Figure 41: Deformation contour of the whole wing in PLA case	78
Figure 42: von Mises stress contour for front spar in PHA case	79
Figure 43: von Mises stress contour for rear spar in PHA case.....	80
Figure 44: von Mises stress contours for skin in PHA case	82
Figure 45: von Mises stress contours for ribs and webs in PHA case	84
Figure 46: Deformation contour of the whole wing in PHA case.....	84
Figure 47: Mode shape for the first modal frequency (16.8Hz).....	86
Figure 48: Mode shape for the second modal frequency (71.7 Hz)	87
Figure 49: Mode shape for the third modal frequency (84.5 Hz).....	87
Figure 50: The locations of applied force and monitored nodes	88
Figure 51: Acceleration response of Node 658237 and Node 658553	89
Figure 52: Locations of 75% semi span section and adjacent sections	92

Figure 53: The location of shear center at 0.75 semi-span.....	93
Figure 54: Stitching of (a) stringer to skin, (b) rib to skin, (c) skin with integral spar caps.....	96
Figure 55: Integral composite skin-stringer assembly	97
Figure 56: Schematic of the VARTM process	98
Figure 57: VARTM setup before covering with vacuum bag.....	98
Figure 58: VARTM setup with vacuum bag and resin lines	98
Figure 59: Manufacturing steps of a cocured composite box	103
Figure 60: CAD model of the wing	112
Figure 61: STEP file importing in GAMBIT.....	113
Figure 62: Inner CFD domain.....	116
Figure 63: The whole CFD domain	116
Figure 64: Boundary conditions for CFD analysis	117
Figure 65: Selecting the solver properties in Fluent.	118
Figure 66: Velocity inlet boundary condition.....	118
Figure 67: Opening the residual monitors	119
Figure 68: Solution control options.....	119
Figure 69: Solution initialization	119
Figure 70: Starting the iteration process in Fluent.....	120
Figure 71: Writing the interpolation file.....	121

Figure 72: Reading the interpolation file.....	121
Figure 73: Exporting the CFD data to MSC.Patran/Nastran	121
Figure 74: Flowchart of the procedure for interpolating CFD data into FE model ..	122

CHAPTER 1

INTRODUCTION AND LITERATURE REVIEW

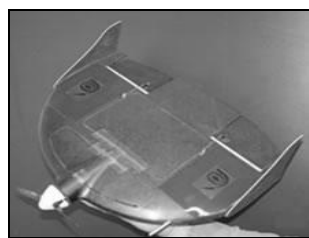
1.1. Introduction to Tactical Unmanned Air Vehicles

Unmanned Aerial Vehicle (UAV) is a remotely piloted or self-piloted (autonomous) aircraft that can carry cameras, sensors, communication equipments or other payloads. They have been used in reconnaissance and intelligence-gathering roles since the 1950s, and more challenging roles are envisioned, including combat missions [1]. Nowadays they are also used in an increasing number of civil applications such as meteorological measurements, disaster management and maritime surveillance. UAVs are becoming popular day by day because of their low cost, multi-role capabilities and ability of taking the risks from human in dangerous missions.

UAVs are classified with respect to their mission profiles which are based on range, endurance and cruise altitude. In general, endurance determines the fuel that is carried, the chosen aerial communication technology has an impact on the operational range and the cruise altitude affects the payload technology in surveillance UAVs. According to Unmanned Vehicle Systems International [2] the classification of UAVs is given in Table 1.

Table 1: Classification of UAVs [2]

		Specifications			
		Range (km)	Flight Altitude (m)	Endurance (hour)	Maximum Take-Off Weight (MTOW)
UAV Classes	Micro	<10	250	1	<5
	Mini	<10	150-300	<2	<30
	Short Range Tactical	70-200	5000	6-10	1250
	Medium Altitude Long Range	>500	14000	24-48	1500
	High Altitude Long Endurance	>2000	20000	24-48	12000



(a) IAI's "Mosquito"



(b) METU's "Güventürk"



(c) AAI's RQ-7 "Shadow 200"



(d) IAI/Malat's "Heron"



(e) Northrop Grumman's RQ-4B "Global Hawk"

Figure 1: Examples for Different UAV Types: (a) Micro, (b) Mini, (c) Tactical, (d) Medium Altitude Long Endurance (MALE), (e) High Altitude Long Endurance (HALE)

From military point of view, tactical UAVs are designed to support tactical commanders with near-real-time imagery intelligence at ranges up to 200 kilometers [1].

1.2. METU Tactical UAV (TUAV)

In Aerospace Engineering Department of Middle East Technical University (METU), a UAV Research and Development project was started with the financial support of State Planning Organization in 2005. The aim of this project was to build a mini and a tactical UAV and establish the necessary infrastructure of a UAV research center for future projects. The first output of the project, METU Mini UAV "*Güventürk*", was successfully manufactured and its flight tests were accomplished. A photograph of *Güventürk* during a flight test is shown in Figure 1. The second outcome of the project is a tactical UAV and this study is based on this tactical UAV platform. The design of METU TUAV is complete and its first prototype is under construction.

CHAPTER 2

DESIGN AND MANUFACTURING OF THE METU TUAV

2.1. Design Features of METU TUAV

Most of the time, the attempt to create an aircraft design arises simply from the need, and as a result the requirements of the end product are known. Looking at the characteristics of previous examples would be the least time consuming and the most efficient way to start a design process because it guarantees that the designer has a number of ideas to develop therefore the outline is ready for a rough preview of the conceptual design. This is how the design team of the METU TUAV including the author of this thesis, started the conceptual design. Firstly a competitor study was done and then by following the design steps of Raymer [3], the conceptual design of the METU TUAV was finalized. To give the details of the conceptual design process is beyond the scope of this thesis therefore only the results and some parts related with structural design will be mentioned.

At the end of the conceptual design, the specifications of METU TUAV were decided as shown in Table 2.

Table 2: Specifications of METU TUAV

Payload	: Daylight / FLIR Camera (TBD)
Payload Weight	: 20 kg
Wing Span	: 4.3 m
Wing Aspect Ratio	8.39
Wing Taper Ratio	0.45
Length	: 3 m
Maximum Take-off Weight	: 105 kg
Cruise Velocity	: 46 m/s
Stall Speed	: 17 m/s
Operation Altitude	: 3000 m
Operation Range	: 150 km
Propulsion	: 21 HP - Two Cycle Gasoline Engine

From the beginning of the conceptual design, CAD software CATIA V5 is used extensively. Parametric design became the rule of thumb of the design team since it decreases the man hour considerably. Once the initial 3D model of the METU TUAV is done, critical parameters such as taper ratio, aspect ratio, reference wing surface area etc are linked to it. This way when the critical parameters change during design iterations 3D model can be updated in a very short time. The three view of the METU TUAV can be seen in Figure 2. The computer aided design of the METU TUAV was performed by the author of the thesis based on the conceptual design parameters that came out after the work of the design team.

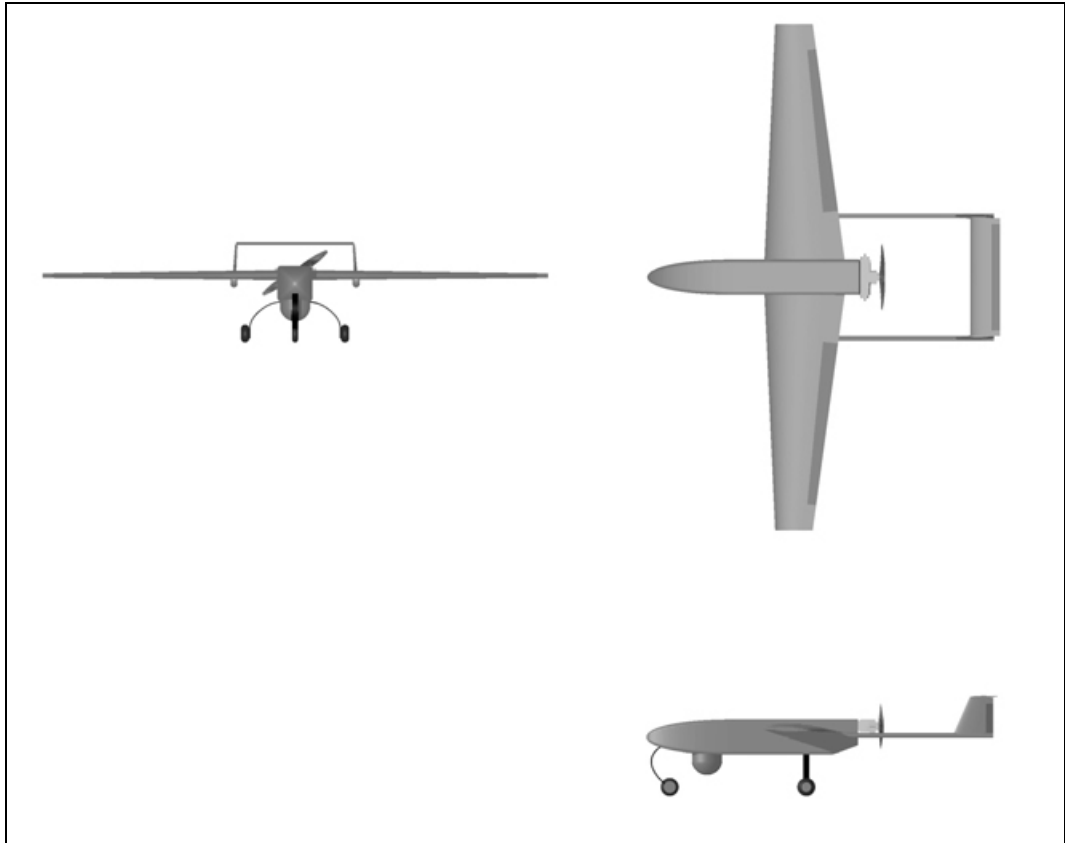


Figure 2: Three View of METU TUAV

2.2. Structural Design of METU TUAV

The first step of the airframe structural design is to determine the loads acting on the aircraft. These loads are the inertia forces due to maneuvers, pressure loads due to air flow around the aircraft and reaction forces due to ground landing [4]. The requirements for these loads are stated in related airworthiness requirements. For METU TUAV, UAV Systems Airworthiness Requirements (USAR) [5] which is prepared by USAR Working Group is used.

The loading conditions of an aircraft can be shown graphically by plotting the load factor versus the airspeed. This graph is called as V-n diagram. The procedure of constructing the V-n diagram is described below.

a. Determination of stall speed, V_{stall} :

In accelerating level flight conditions, lift produced by the aircraft is equal to the product of the load factor and the weight of the aircraft.

$$n \cdot W = L \quad (1)$$

$$n \cdot W = \frac{1}{2} \rho_{\infty} V^2 C_L S_{ref} \quad (2)$$

Therefore,

$$n = \frac{1}{2} \rho_{\infty} V^2 C_L \frac{S_{ref}}{W} \quad (3)$$

The curve constructed by using Equation (3) is a limiting condition which represents the possible lift capability. It is also called the stall line.

For unaccelerated flight at stall conditions:

$$n = 1 \text{ and } V = V_{stall}$$

$$V_{stall(1g)} = \sqrt{\frac{2 \cdot W}{\rho_{\infty} S_{ref} C_{L_{max}}}} \quad (4)$$

$$V_{stall+(1g)} = 21.7 \text{ m/s for positive angle of attack}$$

$$V_{stall-(1g)} = 27.4 \text{ m/s for negative angle of attack}$$

Values for $V_{stall+(1g)}$ and $V_{stall-(1g)}$ are different because the corresponding $C_{L_{max}}$ values are different for positive and negative angles of attack [8].

For accelerated flight at stall conditions:

$$V_{stall(ng)} = V_{stall(1g)} \cdot \sqrt{n} \quad (5)$$

b. Determination of positive and negative limit load factors:

According to "USAR.337a: Limit Maneuvering Load Factors" the positive limit maneuvering load factor n may not be less than

$$2.1 + \frac{10900}{MTOW + 4536} \quad (6)$$

where the maximum take-off weight is given in kg.

However, 'USAR.337a: Limit Maneuvering Load Factors' also specifies that the load factor need not be more than 3.8. For the particular design Equation (6) gives:

$$n = 2.1 + \frac{10900}{105 + 4536} = 4.45$$

Therefore, maximum positive load factor ($n_{\max(+)}$) is taken as 3.8.

According to USAR.337b, The negative limit maneuvering load factor may not be less than 0.4 times the positive load factor.

Therefore, maximum positive load factor ($n_{\max(+)}$) is taken as 1.52.

According to USAR.333:, the velocity at the intersection of stall line and $n_{\max(+)}$ line is the *Design Maneuvering Speed, VA*.

$$VA = V_{stall(3.8g)} = V_{stall+(1g)} \cdot \sqrt{3.8} \quad (7)$$

Thus, the design maneuvering speed is calculated as $VA = 42.3m/s = 82.2kts$. This calculation assumes that the maximum lift coefficients at 1g stall and at ng stall points are equal to each other.

The velocity at the intersection of stall line at negative angle of attacks and $n_{\max(-)}$ line is the *Negative Maneuvering Load Factor Speed, VG*.

$$VG = V_{stall(1.52g)} = V_{stall-(1g)} \cdot \sqrt{1.52} \quad (8)$$

Thus, the negative maneuvering load factor speed is calculated as $VG = 33.8 m/s = 65.7kts$

c. Determination of design airspeeds:

According to *USAR.335.a*, *VC* is the *Design Cruise Speed* which may be defined according to UAV operating requirements. In conceptual design cruise speed is determined as:

$$VC = 46.3m / s = 90kts$$

According to *USAR.335.b*, *Design Dive Speed*, *VD*, may not be less than 1.25*VC*. In addition, according to Anderson [6], the high-speed limit velocity is higher than the level flight maximum cruise velocity by a least factor of 1.2. In conceptual design of METU TUAV, maximum cruise velocity was calculated as 83*m/s*. Therefore, design dive speed is taken as:

$$VD = 1.2V_{\max} \quad (9)$$

$$VD = 100m / s = 194kts$$

There is also a velocity that UAV should not exceed for safe operation. This velocity is called as *Never Exceed Speed*, *VNE*. According to *USAR.1505.1*, never exceed speed is given as

$$VNE = 0.9VD \quad (10)$$

$$VNE = 90m / s = 175kts$$

After calculating necessary design speeds, V-n diagram of the METU TUAV is constructed as shown in Figure 3.

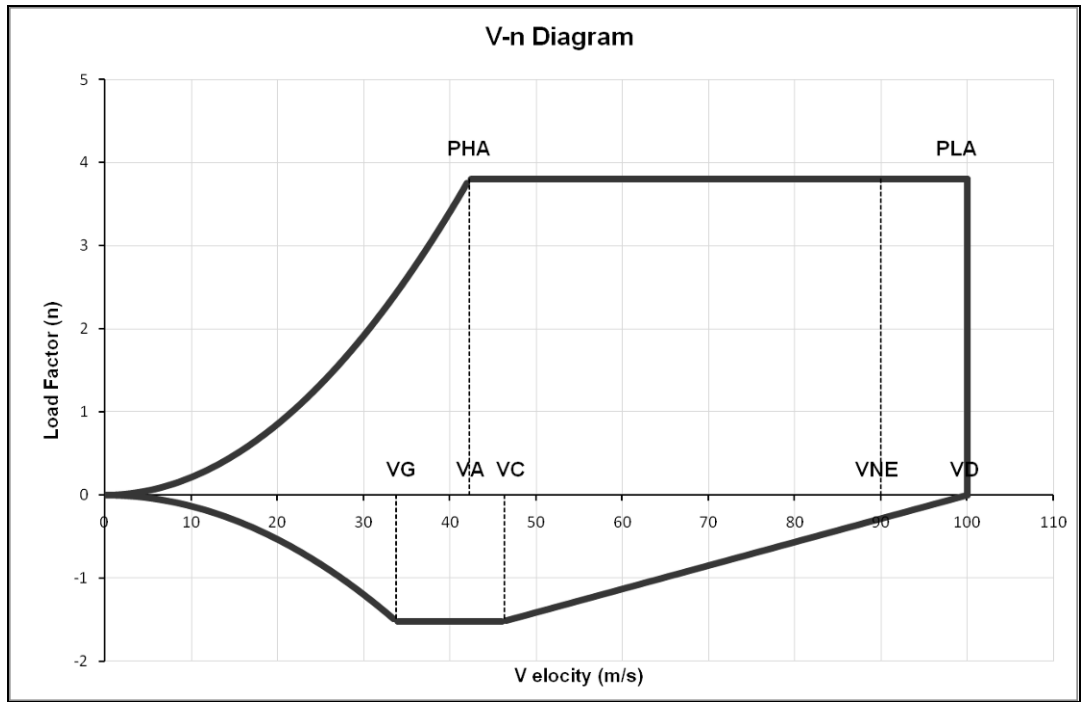


Figure 3: V-n diagram of METU TUAV [5]

The critical flight conditions are taken at positive high angle of attack (PHA) which occurs at V_A and at positive low angle attack (PLA) which occurs at V_D . In structural analysis, aerodynamic loadings will be calculated at these two flight conditions. The positive low and high angle attack values will be calculated in Chapter 3 which describes the procedure for the determination of aerodynamic loading by computational fluid dynamics.

In this thesis, structural analysis and manufacturing of METU TUAV's wing is explained since wing is the most important sub-structural part of an aircraft.

2.3. Manufacturing Methodology of METU TUAV

In scope of UAV R&D project, a composite workshop was established in the Department of Aerospace Engineering of METU. The manufacturing capability of this facility is increasing continuously. The first step of the project which was a mini UAV was manufactured here successfully by a group of aerospace engineers and technicians. The experiences gained and lessons learned in mini UAV is transferred

to the manufacturing activities of the tactical UAV. The manufacturing method used in tactical UAV is similar to the method used in mini UAV manufacturing. The manufacturing of composite airframe relies basically on the application of vacuum bagging technique on the female molds. This technique is explained in detail in a previous thesis study by Turgut [7]. Therefore a repetition of this work is not done in this thesis. However, emphasis will be given to the differences in the manufacturing methodology followed.

2.3.1. Preparation of Molds

The first step of METU TUAV's composite manufacturing is manufacturing the male molds. Male molds are manufactured by coating E-Glass woven composite with epoxy resin on polystyrene foam as shown in Figure 4. Polystyrene foams are cut with a CNC foam cutter in the form of the required shape. In Figure 4, foam used for the manufacturing of the wing is shown.



Figure 4: E-Glass coated polystyrene foam used in the manufacturing of the METU TUAV wing

The female molds are manufactured by coating E-Glass woven composite with a special laminate tool resin on male molds and reference surfaces. Figure 5 shows the finished male model whose surfaces are used as the reference surfaces in manufacturing of the female molds.



Figure 5: Male mold ready to be used as reference for female mold manufacturing

The main difference between the female molds of mini UAV and that of the tactical UAV is the materials used in manufacturing. In mini UAV's female molds, the fiber material is chopped fiber E-Glass and the resin material is polyester. Polyester cures fast and exothermically. The generated heat during the curing process may deform the mold if the heat cannot be transferred by means of ventilation. Also the molds which are manufactured using this procedure cannot withstand high temperatures. Because the chopped fiber-polyester composite material cannot withstand thermal strains which affect the dimensional tolerances of work piece in the mold. Therefore it is risky to use them in curing ovens where the molds may deform and the final end product may lose geometric accuracy. In tactical UAV's female molds, thick E-Glass woven tool fabric and a special laminate tool resin is

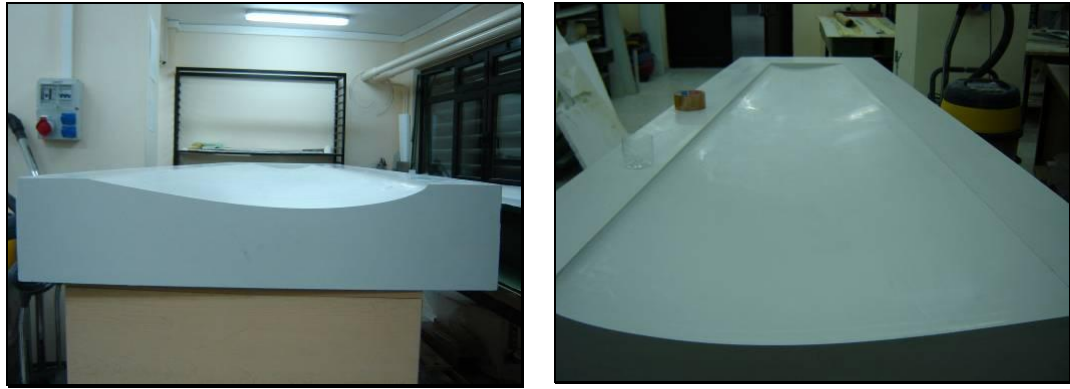
used as shown in Figure 6 and Figure 7. With the use of thick woven E-Glass woven tool fabric and special tool resin, a stiffer mold with a better surface quality is achieved. The finished female molds of METU TUAV's wing can be seen in Figure 8.



Figure 6: Covering the male mold with tool resin



Figure 7: Reinforcing the mold with woven E-glass woven fabric



(a) Side View

(b) Top View

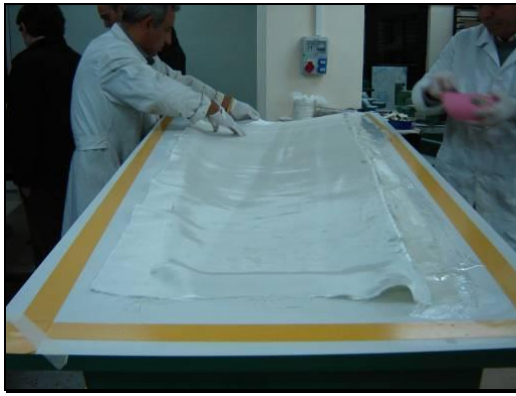
Figure 8: Female wing molds

2.3.2. Manufacturing of the Wing

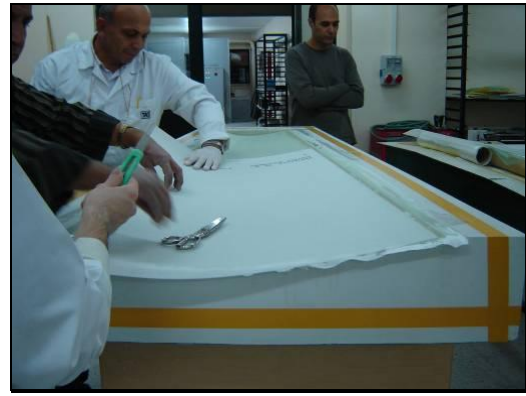
Manufacturing of the wing is done in four steps.

1. Manufacturing of the skins
2. Manufacturing of the front and rear spars
3. Manufacturing of the ribs
4. Assembling all of the components

METU TUAV's composite parts are manufactured with vacuum bagging technique. In all composite parts, Araldite LY 5052 epoxy is used as resin material. Skins are composite sandwich structure having Rohacell 31A core material between e-glass layers. Different from the manufacturing of the upper skin, in spar locations of lower skin carbon fabric layer are added which will form the lower flanges of the spar later. The manufacturing steps of the wing skins are shown in Figure 9. Figure 9d shows the placement of the carbon fabric on the lower skin. The choice of lower skin for the placement of carbon fabric to form the front and rear spar caps is due to the fact that during flight the wing will be under up-bending resulting in tensile loads in the lower skin for most of the time.



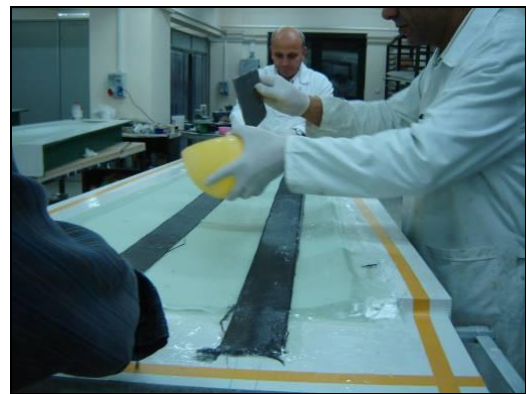
(a)



(b)



(c)



(d)

Figure 9: Manufacturing steps of the wing skins: (a) First e-glass layer, (b) Rohacell foam layer, (c) Last e-glass layer, (d) Spar flanges in the lower skin

One lesson learned from METU mini UAV was to make the structural parts as integrated as possible. The integrated manufacturing of composite parts has some advantages like weight saving by reducing adhesive material and achieving better structural integrity between the spar and the skin by the removing adhesive layer. Therefore, in the manufacturing of the wing of the tactical UAV, the spars are not simply adhesively bonded to the upper and lower skin after separate manufacturing of the spars and upper and lower skins. The goal is to manufacture the spar cap-lower skin connection by vacuum bagging of the spar fabrics, which will be laid over the spar molds, with the lower skin and overlay the spar fabric extensions with the

carbon fabric strips that were already placed on the lower skin of the wing (Figure 9d) and cured under vacuum at 50°C in curing oven



Figure 10: Positioning the spars

After manufacturing of the lower skin, styrofoams are positioned in front and rear spar locations on lower skin as shown in Figure 10. The spars are integrated to lower skin because, as explained above, the lower skin is under tensile stress during most of the flight times and the integrity of the spar and lower skin connection is crucial. The styrofoams will be the male molds for spars and layers of carbon fabric are laid on these permanent styrofoam molds. It is possible that ambient pressure may deform the styrofoam molds when they are under vacuum. Therefore, before positioning of the foam molds, they are coated on the web sides with one layer carbon-epoxy to make them stiffer. This can be seen clearly in Figure 10. As shown in Figure 10, spars are positioned on the carbon fabric strips which were placed during the manufacturing of the lower skin of the wing. It should be noted that in the current manufacturing method, lower wing skin and spar molds are manufactured

separately. However, as it will be explained in the following, spar fabrics which will be placed over the strengthened spar molds will be coated with epoxy resin and vacuum will be applied over the spar fabrics and thus the spar fabric extensions will be cured on the lower skin carbon fabric strips which were placed over the lower skin of the wing during the manufacturing of the lower skin of the wing. A better way would be to manufacture spars and the lower skin in one vacuuming operation integrally. However, in this method there is a possibility of distorting the position of the spar molds during the vacuum bagging operation. Therefore, in order not to risk the probable distortion of the wing spars during the vacuum bagging operation, lower wing skin is manufactured first, and then spars are integrated to the lower skin by a second vacuum bagging operation.

In the places near to the root of the wing styrofoams are replaced with different materials. These sections of the spars should be stronger since the wing will be attached to the fuselage from the ends of spars with bolts. In rear spar aluminum 7075-T6 is used as substitute material. Figure 11 shows the rear spar wing root reinforcement. It is known that aluminum and carbon are not compatible materials to be used together. The reason is the different electrochemical properties of these materials. In an environment with an electrolyte such as humidity, the contact of aluminum and carbon fiber results in galvanic corrosion of aluminum. To prevent the corrosion, aluminum is electroplated with alodine and a thin e-glass epoxy layer is laid between carbon and aluminum. Since both e-glass and epoxy are perfect insulators, this layer will prevent aluminum from corrosion.

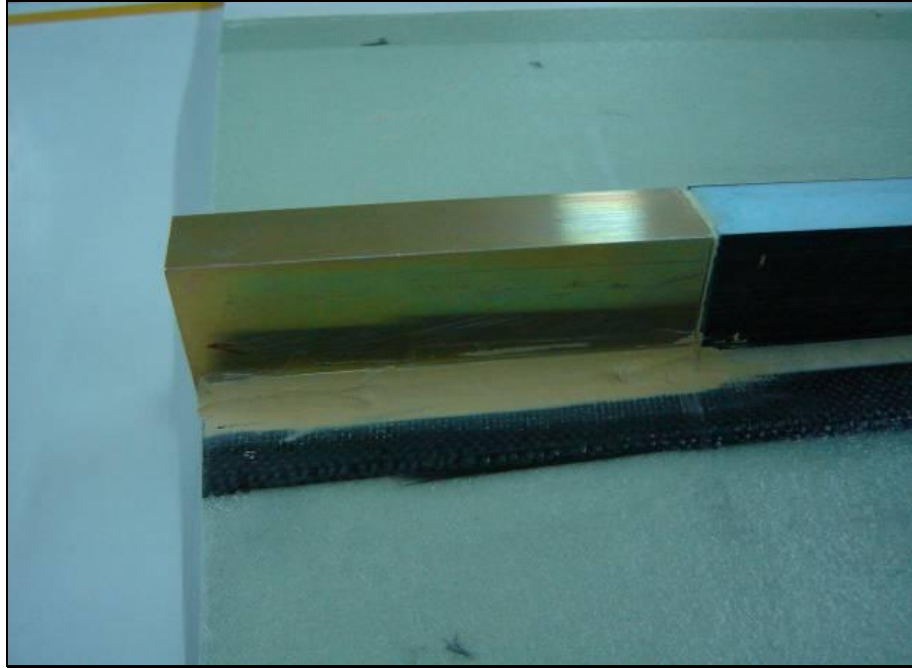


Figure 11: Allodized aluminum section of the rear spar

In front spar, laminated hornbeam wood is used as the reinforcement material at the root, and this is shown in Figure 12. Hornbeam also called “ironwood”, is a very hard wood and can give exceptional strength properties. Its ultimate strength in fiber direction is 153MPa. The thickness of the hornbeam wood is composed of layers hornbeam plies which are compacted to the required thickness. Layers of hornbeam are adhesively joined with each other with epoxy resin.



Figure 12: Hornbeam section of the front spar

Figure 11 and Figure 12 show that the rear spar wing root ends at the end of the wing, whereas, the root of the front spar extends outside the wing. With this structural design, it was intended to place the front spar in a box which will be connected to the fuselage such that the box and fuselage axes will be perpendicular to each other. The spars were designed such that the front spar was perpendicular to the chordline, but the rear spar does not intersect the chordline perpendicularly. Therefore, the extension of the rear spar outside the wing would necessitate a fuselage box which would have to be placed at an angle different from ninety degrees with respect to the fuselage axis. In addition, it was decided not to make any kinks along the length of the spars in order to prevent stress concentrations associated with the kinks. Therefore, the rear spar should preserve its direction. Thus, in the final design in order to eliminate the difficulties associated with the assembly of the wing to the fuselage, it is decided to connect the rear spar to the fuselage bulkhead on the rear spar side with two bolts through the aluminum reinforcement placed at the root of the rear spar. On the other hand, the front spar

will be placed in a box structure which will be connected to the fuselage bulkhead at the front spar side.

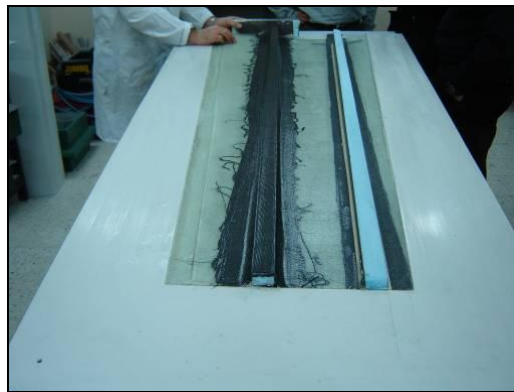
In the next step, woven carbon layers are laid on the strengthened spar molds and wing root end reinforcements and final vacuum bagging is applied locally to the spars along the full span of the wing. In this way spar and lower wing skin connection is generated under vacuum eliminating the probable formation of voids during the curing operation. The curing process is done in the curing oven at 50°C.



(a)



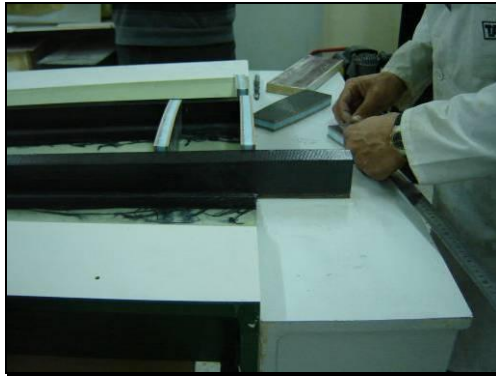
(b)



(c)

Figure 13: Manufacturing of the spars: (a) Laying up the carbon woven fiber, (b) Spars in vacuum bag, (c) Finished rear spar

The last major step of manufacturing of the wing is to close the upper skin on to the integrated spar-rib-lower skin structure. Before this operation ribs are placed in the required places along the span of the wing as shown in Figure 14a and Figure 14b. Ribs are separately manufactured as a sandwich structure which consists of two separate layers of hornbeam wood, center foam and carbon fabric layers between the wood and foam material. Ribs are first connected to the lower skin by means E-Glass fabric and epoxy resin along the lower edge of the rib which intersects with the lower skin. After the ribs are fixed in their positions on the lower skin, the upper edges of the ribs, which will face the upper skin of the wing, are trimmed and a close match is obtained between the ribs and the upper skin. The match is frequently checked by placing the upper skin over the lower skin assembly and checking the gap between the spars and ribs with the upper skin. This process is an iterative process and requires frequent checking of the gap after the upper skin is placed over the lower skin assembly. It should be noted that the thickness of the adhesive which will be placed over the spars and wing ribs has to be taken into account, and therefore small gap has to be provided between the upper faces of the spar and the ribs facing the upper skin and the upper skin itself. The upper skin is joined to the other parts with structural adhesive as shown in Figure 14. The brown color material in Figure 14b is a mixture of the adhesive and chopped wood particles. The chopped wood particles increase the strength of the adhesive by serving as discontinuous short fibers at random orientation. Assembly is completed by placing the two parts of the female wing molds over each other and clamping the molds along the circumference of the matching surfaces of the both parts of the female molds. The assembly is left for cure for twelve hours. After the cure is complete, the female molds are separated and the wing which usually remains in one part of the female mold is taken out for final trimming, surface finishing and painting operation.



(a)



(b)



(c)



(d)

Figure 14: Assembling the structural part of the wing: (a) Ribs, (b) Adhesive layer, (c) Releasing the wing from the mold, (d) Wings after released from female molds

CHAPTER 3

DETERMINATION OF AERODYNAMIC LOADING BY COMPUTATIONAL FLUID DYNAMICS

3.1. Introduction

For structural analysis of a wing, it is necessary to find the loading on the wing. This loading is due to aerodynamic forces coming from 3D pressure distribution on the wing. The distribution of these aerodynamic forces acting on the wing can be found either by experimental techniques using wind tunnel measurements or by means of numerical methods using computational fluid dynamics (CFD) or by means of empirical methods. Although the experimental techniques are the most accurate and reliable method for determining these forces, their use is restricted by their high cost and the limited availability of appropriate wind tunnels. On the other hand, numerical methods are replacing wind tunnel tests because of their increasing accuracy in determining the aerodynamic forces and moments acting on aircraft. With today's very fast and modern computers it is possible to perform numerical wind tunnel experiments in a very short time and with the precision of experimental results and with very low cost. Engineering methods based on empirical tools also give very fast results however their accuracy are not comparable to numerical techniques.

In this study, CFD method is used to calculate the flow field around the wing and the resulting 3D pressure distribution acting on the wing. Then from this pressure distribution the nodal forces are calculated and then they are exported into the finite element program by means of interpolation from the CFD mesh to finite element mesh. In this study, flow field computations are performed using the commercially available CFD tool *Fluent 6.2.16*, and the structural analyses were performed by MSC Patran/Nastran.

3.2. Generation of the Computational Mesh

The first step of the CFD calculation is to generate the computational mesh in the flow field domain. The computational mesh is generated by a commercial package program *Gambit*. First, the domain is divided into two sub-domains; inner and outer domains, with variable grid spacings and intensities. The grid spacing in the inner domain is much finer and contains ten times more elements than the outer domain. The volume of the inner domain covers only 0.25% of the outer domain. ($V_{inner}=0.25\%*V_{outer}$) The domain is nested in such a way because the pressure gradients are higher in the vicinity of the wing than the farfield zones. The CFD mesh used is given in Figure 15. Two different volume meshes are generated for cases PHA (Positive High Angle of Attack) and PLA (Positive Low Angle of Attack). Model summary for both cases is tabulated in Table 3.

Table 3: Properties of volume mesh for PLA and PHA cases

	AoA 0°	AoA 14°
Number of Cells	2,951,886	2,814,039
Number of Nodes	514,007	490,929

For PHA angle of attack is set to 14° which is the stall angle of attack for the airfoil profile of the wing. In PLA case, angle of attack is set to 0° which can be found from the following calculations.

$$n \cdot W = \frac{1}{2} \rho_{\infty} V^2 C_L S_{ref} \quad (11)$$

Therefore:

$$C_L = \frac{2 \cdot n \cdot W}{\rho_{\infty} V^2 S_{ref}} \quad (12)$$

According to USAR.337a it is found that $n_{\max(+)} = 3.8$ and velocity is set to design dive speed ($VD = 100m/s$). Inserting the rest of the variables in Equation (12) yields to a lift coefficient of:

$$C_L = 0.29$$

Although the lift coefficient of a wing is not identical to its airfoil's lift coefficient due to 3D aerodynamic effects, at low angles of attack this discrepancy is negligible. The corresponding angle of attack for $c_L = 0.29$ is 0° for NACA 63412 [8].

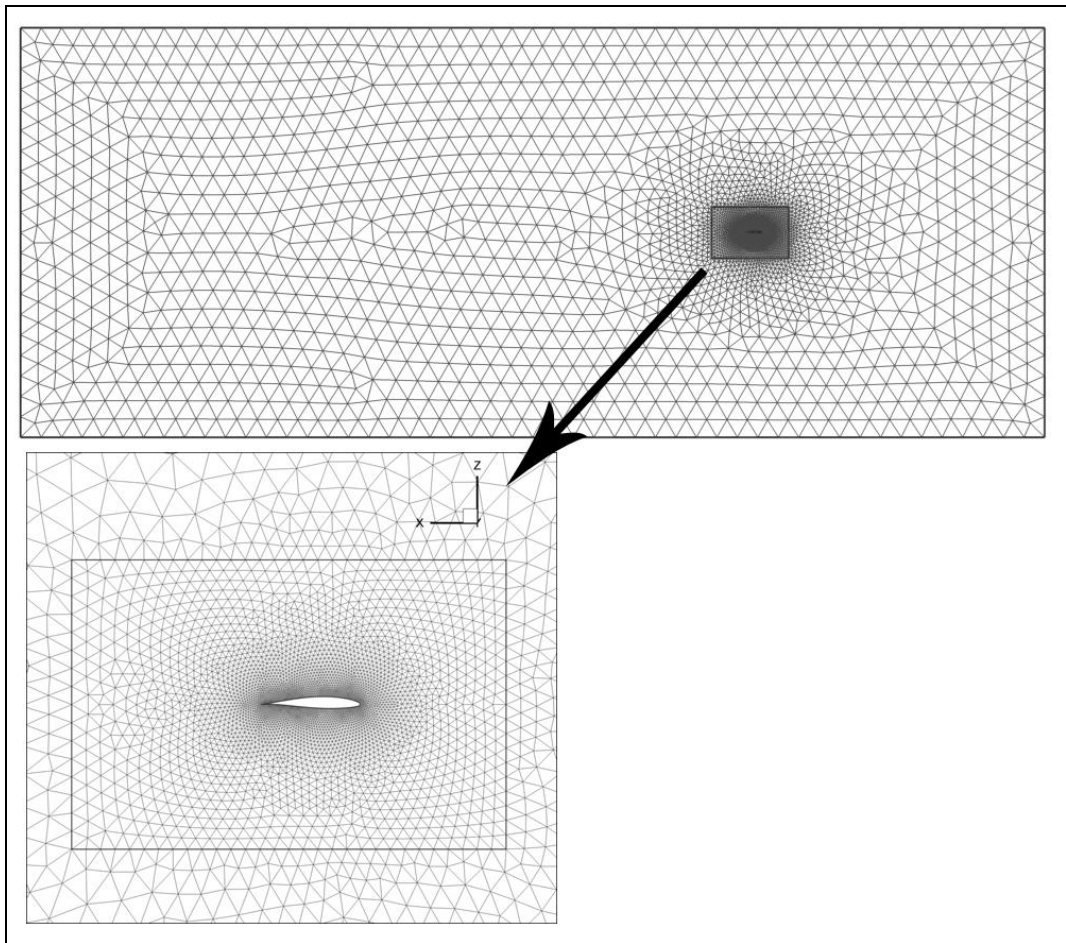


Figure 15: Mesh around the root section of wing

Lastly proper boundary conditions were set to the solution domain. Figure 16 shows the boundary conditions used in the CFD analysis. At upstream (zone 1) *Velocity Inlet* boundary condition was chosen and the velocity value was set to 100 m/s (Design Dive Speed) for PLA and 42.3 m/s (Design Maneuvering Speed) for PHA. At downstream (zone 2) *Pressure Outlet* boundary condition was chosen. Since the downstream zone is far enough from the wing the gauge pressure value at this zone could be set to 0. Zones 4 - 5 - 6 were set to *Symmetry* boundary condition. In these zones symmetry boundary condition can be assumed only if they are far enough from the wing where the pressure gradients are almost zero. Finally zone 3 was set to *Symmetry* boundary condition since half of the wing with respect to XZ plane, shown in Figure 15, is used in the model.

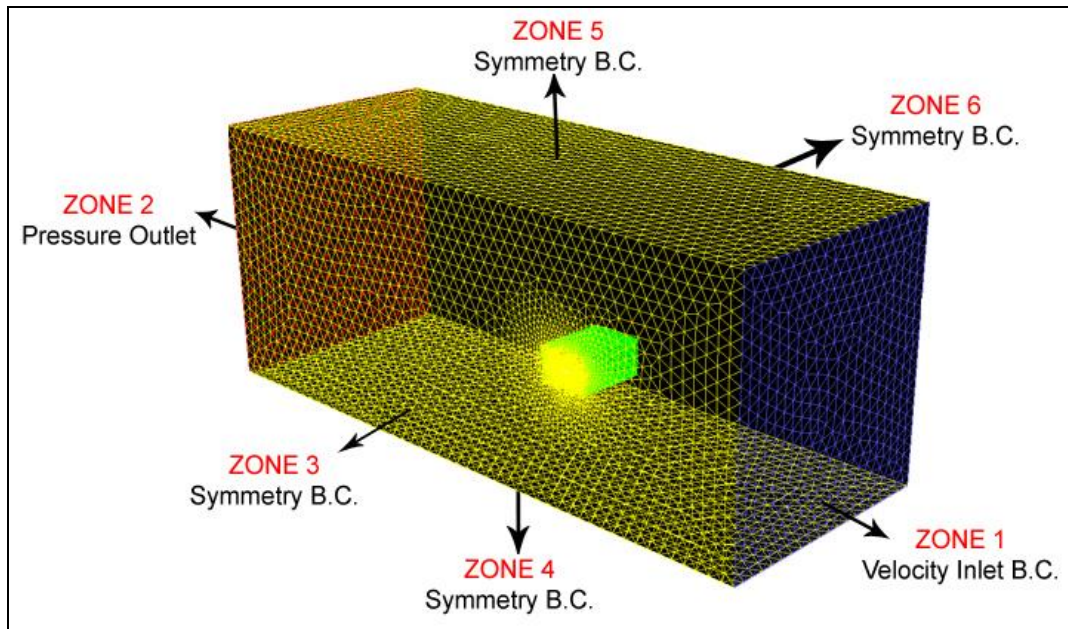


Figure 16: Boundary Conditions for CFD Analysis

3.3. CFD Analysis

CFD analysis of METU TUAV's wing was performed using the *Fluent 6.2.16* software. In the analysis, 3D Euler solver of the Fluent is used. In the solution options, incompressible and steady flow assumptions were chosen. The

incompressibility effects usually occur after Mach 0.3. In PLA case, the velocity is the dive speed of the METU TUAV, 100 m/s (Mach 0.3) therefore incompressible flow assumption is deemed to be convenient.

For both angle of attack cases, the pressure coefficient (C_p) distribution at the root section are shown in Figure 17 and C_p distribution on wing surfaces are shown in Figure 18. Calculated net forces in z-direction and lift coefficients are tabulated in Table 4. When CL values found from CFD are compared with analytical 3D lift coefficients which were found during the conceptual design phase, the results are reasonable.

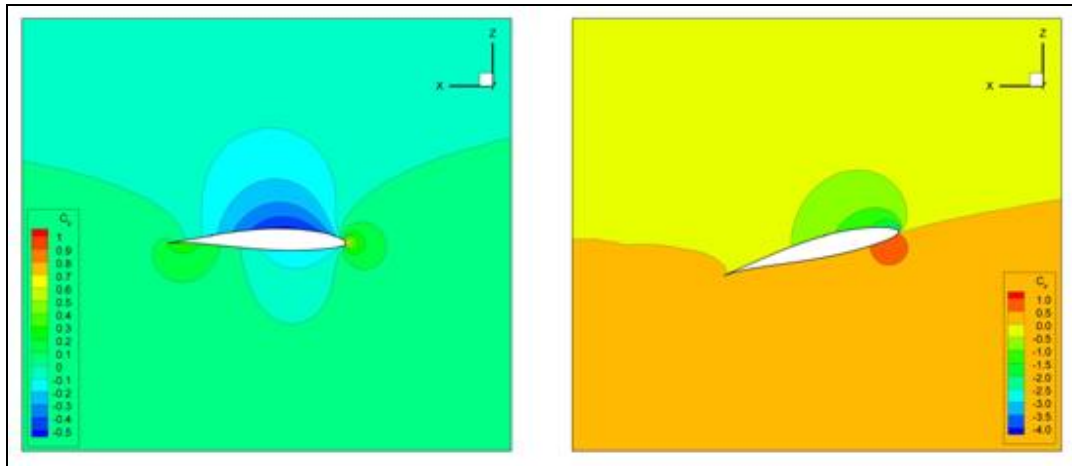


Figure 17: C_p distribution around root section of the wing

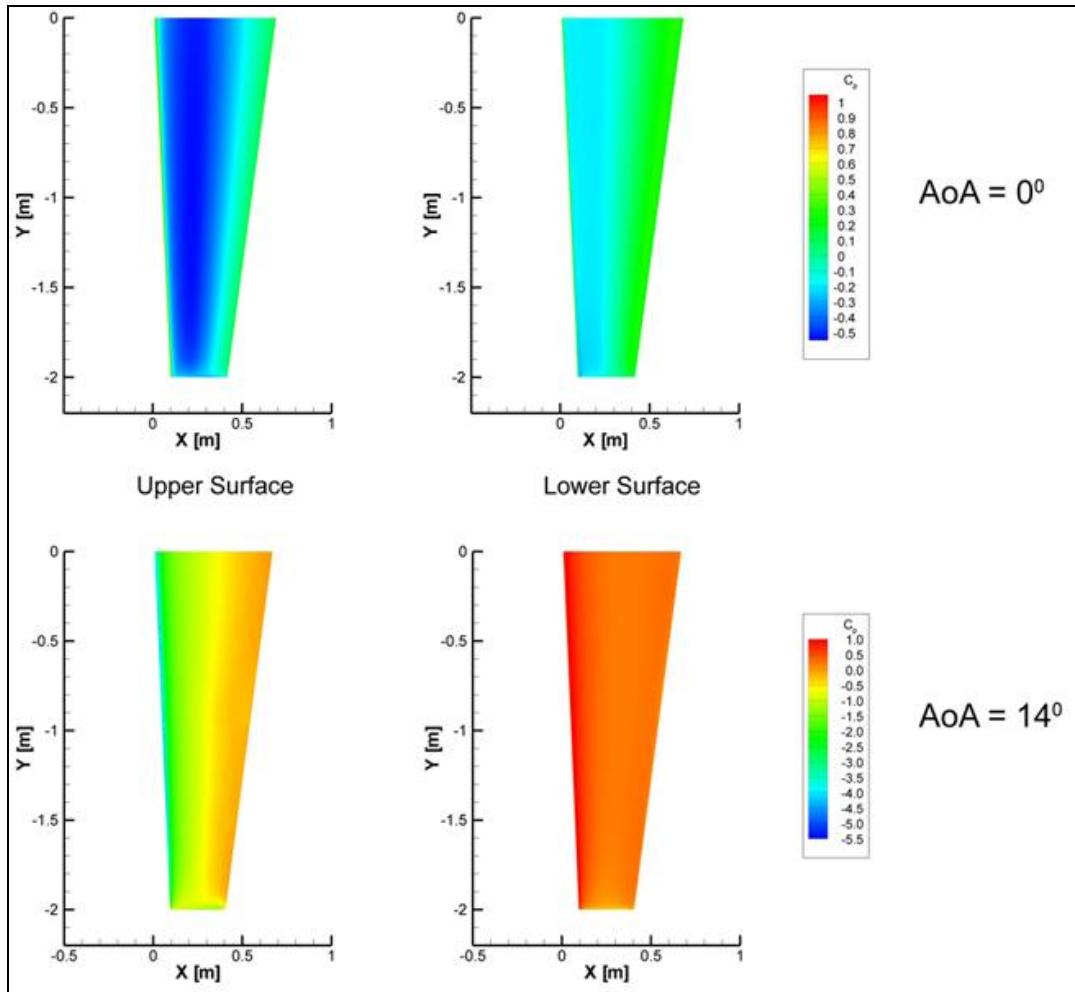


Figure 18: C_p distribution on wing surfaces

Table 4: Results of CFD analysis

	AoA = 0°	AoA = 14°
Net Force in z (N)	1737	1410
C_L from CFD	0.258	1.19
C_L theoretical [6]	0.261	1.39

The differences between the theoretical and computational C_L values can be attributed to the assumptions made in both methods of calculations. First of all in CFD calculations, the velocities at which the solutions are done are determined from

V-n diagram. When constructing the *V-n* diagram, airfoil data is used and it does not include the 3D effects. Secondly, the theoretical C_L values are not exact and they are not found from exact formulas. Nevertheless in terms of structural analysis, it is the distribution of the pressure around the wing which is important but not the resultant integrated forces found from the CFD computations. As long as the pressure distribution found from CFD reflects the actual case, the net forces can be scaled up to the desired value in finite element program.

The effects of grid size on the computational results are also studied during this work. For this purpose, two different meshes, a course and a fine mesh, were used for the PLA case. The grids used and the results obtained with these grid distributions are tabulated in Table 5. The results show that the current case gives results which are good enough to be used as loading in a structural analysis.

Table 5: CFD case study

	Number of cells	Number of Nodes	Net Force in z (N)
Course	2,658,358	450,856	1731
Current case	2,951,886	514,007	1737
Fine	5,012,101	888,543	1741

3.4. Interpolation of Aerodynamic Forces From CFD Mesh to FE Mesh

The properties of a finite element analysis mesh which is used for structural analysis and the properties of a CFD mesh are different in terms of mesh distribution. Mesh distribution is fine where high gradients of variables are seen. In CFD analysis, these gradients are pressure gradients but in FEA these gradients are stress gradients. The comparison between CFD mesh and FE mesh is shown in Figure 19.

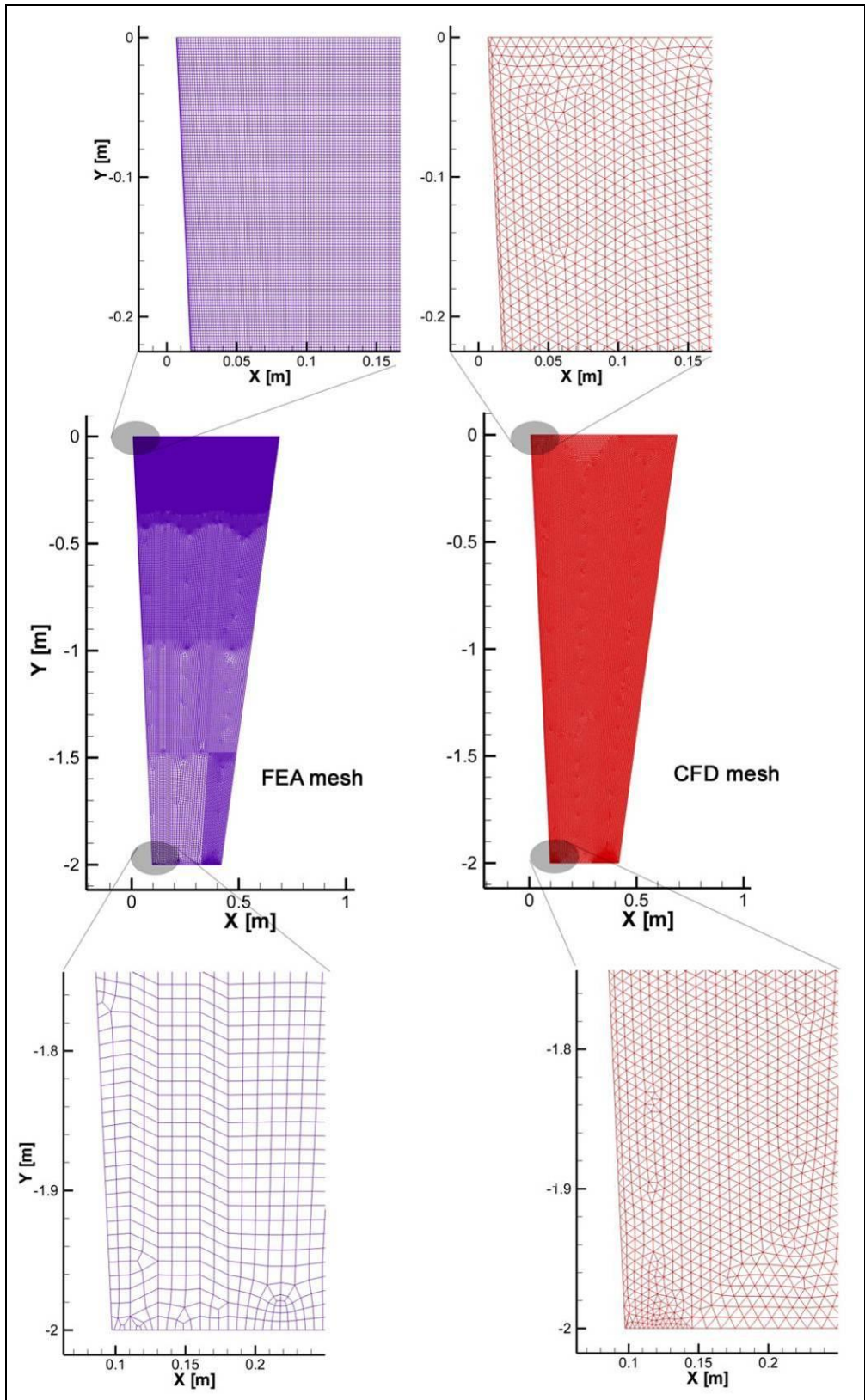


Figure 19: Comparison of CFD and FEA meshes

In CFD analysis the forces are calculated at the nodes of elements. Therefore these forces should be transferred to FE mesh in order to perform the structural analyses. In this thesis, *Fluent's interpolate* option was used to transfer these nodal forces to FE mesh. In order to do this, firstly, a surface mesh on the wing surface is created in *Gambit*, which is the identical to the mesh as used in finite element analyses. Finer mesh was used in high stress gradient areas, i.e. near to the root of wing. Using this surface mesh a 3D volume mesh was generated again in the whole computational domain. The geometrical boundaries of this 3D mesh need to be the same as the boundaries of the CFD mesh which is used to determine the pressure distribution. At this step *Fluent* can perform interpolation between these two 3D domains. Thus, grid forces calculated in the CFD mesh can be interpolated to the mesh which will be used for the structural analysis.

The whole interpolation process is described in Appendix A including the generation of the wing geometry, mesh generation by *Gambit* to be used for interpolation purposes and analysis performed by *Fluent* to accomplish the interpolation. Appendix A is prepared by presenting snapshots from the related menus of the different analysis tools to make the process more descriptive.

After the interpolation, the surface meshes together with the nodal forces are exported as MSC. Nastran *.*bdf* files which are the input files of MSC. Nastran. After this interpolation process, the net forces acting on the wing were found to be not the same as the net forces before interpolation. The net z-force comparison before and after the interpolation procedure is given in Table 6. As it can be seen from Table 6, the difference in the net force in the z- direction before and after the interpolation is very small and the interpolation process is considered to be satisfactory. As mentioned before, the force resultants can be shifted up to the desired value as long as the pressure distribution is accurate. The finite element analysis for PHA and PLA, are conducted at 3.8g and the results are indicated in Table 6.

The effect of the FE mesh size to interpolation is also investigated and the results are tabulated in Table 7.

Table 6: Effect of interpolation to the force resultants

		AoA = 0°	AoA = 14°
Net Force in Z (N)	Before Interpolation	1737	1410
	After Interpolation	1727	1394
	Used in FEA (3.8g)	1957	1957

Table 7: Effect of FE mesh size to the force resultants after interpolation

	Number of 2D elements on wing surface	Net Force in z (N)
Fine FE mesh	158487	1727
Course FE mesh	5592	1694

CHAPTER 4

MECHANICAL PROPERTIES OF WOVEN FABRIC COMPOSITES

4.1. Introduction

2D Composite fabrics are divided into three groups in terms of fiber orientation and techniques that keeps the fibers together. These are unidirectional, woven, and multiaxial. For unidirectional (UD) fabrics, the fibers go through in one direction usually 0° direction which also called the warp direction. Multiaxial fabrics consist of one or more layers of long fibers held in place by a secondary non-structural stitching tread. The main fibers can be any of the structural fibers available in any combination [9]. Woven fabrics (WF) are made of by twisting fibers in warp (0°) and weft (90°) directions in a systematic pattern and weave style.

Woven fabrics have some advantages over unidirectional fabrics. They have superior damage tolerance. WF composites provide more balanced properties in the fabric plane and higher impact resistance than UD composites. The interlacing of yarns provides higher out-of plane strength which can take up the secondary loads due to load path eccentricities, local buckling etc [10]. Also composite manufacturing using WF is easier since their handling is easier and they adapt to surfaces better than UD fabrics. Apart from these advantages, WF composites have inferior in-plane stiffness and strength properties compared to UD ones because of the undulation of yarns.

The use of WF composites has been mostly limited to the secondary structures because of lack of understanding on their mechanical behavior [11]. Classical Laminate Theory (CLT) is widely used to calculate the elastic properties of the flat composite plies which have homogenous fiber distribution and arrangement. For WF composites, the fibers are concentrated in yarns which results a non-homogenous

fiber distribution. Therefore CLT should be modified in order to find elastic properties of WF composites.

4.2. The Geometry of the Woven Fabrics

Woven fabrics are fabricated by weaving which is the interlacing of two sets of yarns at right angle to each other. Warp yarn is the lengthwise yarn system parallel to selvedge of the fabric. Weft yarn (filling) is perpendicular to the warps and lies across the width of the fabric.

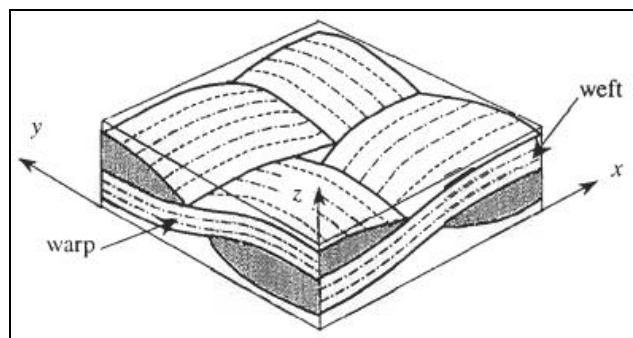


Figure 20: Unit cell geometry

Woven fabrics can be fabricated with different weave styles and patterns for different purposes. Woven fabrics can be classified by these patterns of repeat. The minimum sized periodic sample is chosen as the unit cell of the material. Unit cell contains all individual constituents and micro-structural features [12]. Unit cells will be useful when analyzing the meso-structure of the laminate.

Three commonly used weave styles are plain, twill and satin.

Plain weave style is a commonly used basic and balanced reinforcement for woven composites [13]. Each warp fibre passes alternately under and over each weft fibre making the fabric symmetrical. Plain woven fabrics have a good stability and reasonable porosity. They also have a tighter interlacing among other weave styles which makes them the most difficult to drape. The definition of drape is the ability of

a fabric to fold on itself and to conform to the shape of the article it covers [14]. This disadvantage may cause difficulties in manufacturing during preparing the preform or lay-up process. Also the high level of fibre crimp results inferior mechanical properties compared with the other weave styles.

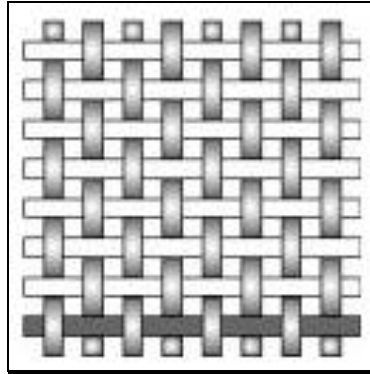


Figure 21: Plain weave fabric

In Twill weave style one or more warp fibres varyingly weave over and under two or more weft fibres in a regular recurring way. With little sacrificing in the stability they provide better wet-out and drape properties than plain weave style. Also fibre crimp levels are lower which results better mechanical properties and smoother surfaces.

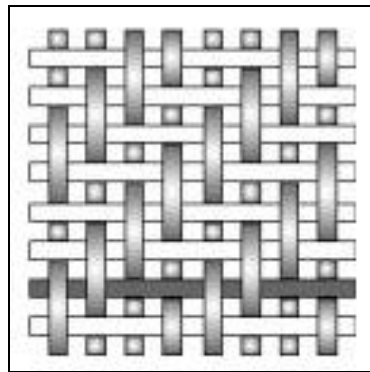


Figure 22: Twill weave fabric

When twill weaves are modified to produce fewer interlaces of warp and weft, Satin weave pattern style is generated. The total number of fibres crossed and passed under, before the fibre repeats the pattern designates the harness number of satin woven fabric. Satin weaves provide good wet-out and drape. Since they are flat they have low crimp angle values in weaves. This results good mechanical properties. Satin weaves have some disadvantages because of the asymmetry in warp and weft directions. In case of manufacturing a multi layer part, this property of the satin woven fabric should be kept in mind and asymmetry should be avoided. Table 8 compares the properties of the three common woven fabrics [15].

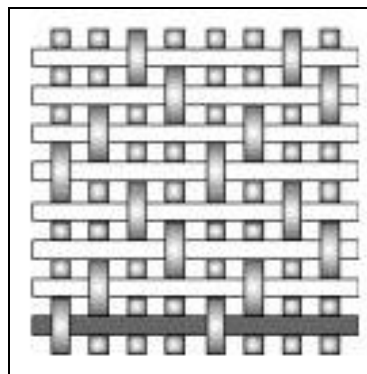


Figure 23: Satin weave fabric

Table 8: Comparison of properties for weave styles [15]

	Plain	Twill	Satin
Good Stability	****	***	**
Good Drape	**	****	*****
Low Porosity	***	****	*****
Smoothness	**	***	*****
Balance	****	****	**
Symmetrical	*****	***	*
Low Crimp	**	***	*****

4.3. Elastic Constants of Woven Fabrics

4.3.1. Introduction to Modeling of Elastic Analysis of Woven Fabrics

Concentrated fibers in the yarn makes woven fabrics highly non-homogenous. As a result the fibre volume fraction is distributed in the weave heterogeneously. Since the fibre volume fraction affects the stiffness of the composite material significantly, it is important to construct a proper material model in order to find the elastic properties. In literature there are three different approaches that deal with elastic properties of woven fabrics.

1. The Elementary Models
2. Numerical Methods
3. Laminate Theory

The elementary models give crude estimation of elastic properties of WF composites. Modeling WF composite as a laminate of UD laminae is an example for elementary model.

Numerical models consist of modeling the unit cell geometry and analyzing this geometry using mostly finite element method. Numerical models can give detailed information about stress and strain inside the unit cell but they are complex models and for different woven fabric new geometry and mesh should be constructed in order to predict the mechanical properties of the WF composite.

Another approach to predict the elastic properties of a WF lamina is using analytical methods based on classical laminate theory. Firstly Halpin et al. [16] used laminate analogy by modeling the weft and warp yarn as angle-ply laminates and combine them to form symmetrical laminates. Ishikawa and Chou [17-18-19] have developed three models called mosaic model, crimp model and bridging model. In the mosaic model a woven composite is idealized as an assemblage of pieces of asymmetric cross-ply laminates. The crimp model is developed in order to consider the continuity and undulations of the fiber in a fabric composite. Lastly in bridging model the interactions between an undulated region and its surrounding regions with

straight threads were considered [20]. All these models are one dimensional models and these models are further improved by Naik and Shembekar [10]. Naik and Shembekar extended Ishikawa and Chou's crimp model to 2D by considering undulations in both warp and weft directions. Falzon et.al [21] has presented a similar model but this time considering continuity of the fibre structure which was neglected before.

4.3.2. Material Model of the Woven Fabrics Used in METU TUAUV

In order to make the finite element analysis of the METU TUAUV, material properties should be found. Since it is not always possible to find the elastic properties of the woven composite fabrics, in this thesis elastic properties were found via analysis.

The methodology of the analysis is to make a micro level analysis firstly and find the UD lamina properties of the composite. After this analysis, at mini level geometry of the yarns are described and finally meso level analysis was done to get the elastic properties of WF composite which were entered to the finite element program. Macro level analysis which considers the complete laminate was handled by the FE program. The modeling methodology is depicted schematically in Figure 24.

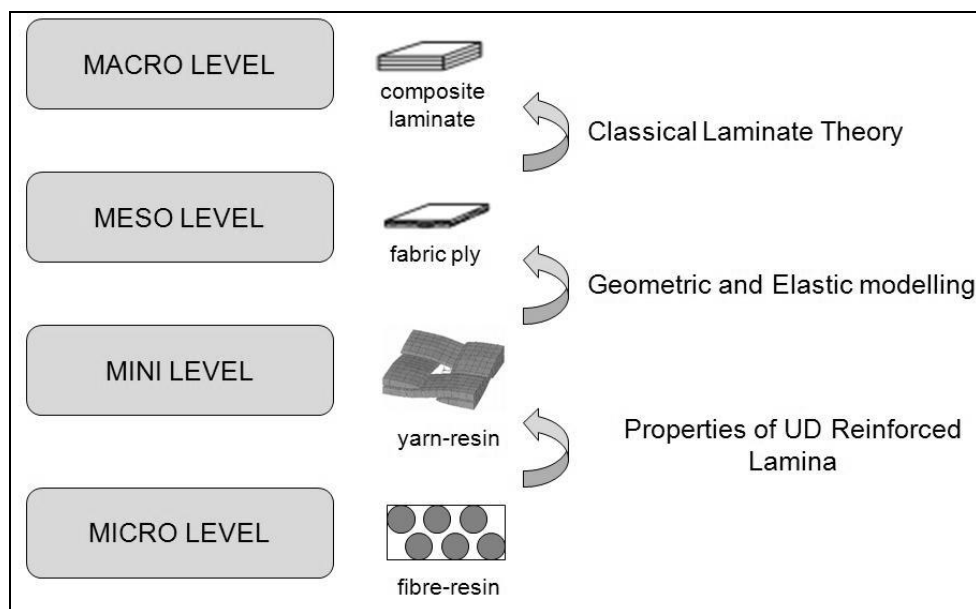


Figure 24: Methodology of analysis

4.3.2.1. Micro Level Analysis

In analytical method developed to analyze the WF composites, yarns can be taken as equivalent UD composites. In the literature there are various methods to calculate UD elastic properties from fibre volume fraction and mechanical properties of fibre and resin. The simplest and the most known method is the Rule of Mixtures. It gives good predictions in the fibre direction underestimates the transverse properties of the composite material. There are also methods of Chamis, Puck, Halpin-Tsai, Christensen and Hashin.

Among all these methods only Hashin's model admits anisotropy in the fibers themselves; all the other models assume the fibers and resin are separately isotropic. Assuming glass fibers are isotropic is very plausible. But the anisotropy in common carbon fibers is substantial and Hashin's model should then be preferred [22].

Hashin's model which is also known as Composite Cylinder Assemblage (CCA) model [23,24], considers a collection of composite cylinders, each with a circular fiber core in a concentric hollow matrix cylinder. The matrix and fiber volume fractions are assumed to be same in each composite cylinder.

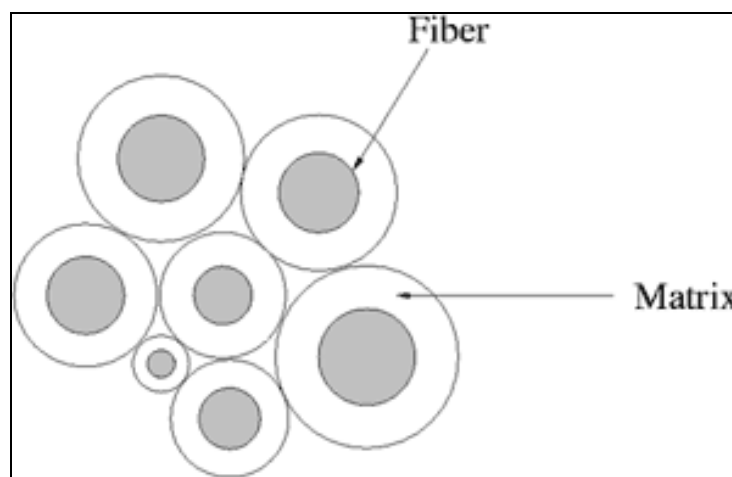


Figure 25: CCA model geometry

In the CCA model, the transverse bulk modulus of the UD lamina is given by [23,24]:

$$k = \frac{k^m (k^f + G_{TT}^m)(1 - V_f) + k^f (k^m + G_{TT}^m)V_f}{(k^f + G_{TT}^m)(1 - V_f) + (k^m + G_{TT}^m)V_f} \quad (13)$$

with,

$$\frac{1}{k^f} = -\frac{1}{G_{TT}^f} - \frac{4\nu_{LT}^{f2}}{E_L^f} + \frac{4}{E_T^f} \quad (14)$$

$$\frac{1}{k^m} = -\frac{1}{G_{TT}^m} - \frac{4\nu_{LT}^{m2}}{E_L^m} + \frac{4}{E_T^m} \quad (15)$$

The longitudinal modulus is given by [23,24],

$$E_L = E_L^f V_f + E_L^m V_m + \frac{4(\nu_{LT}^f - \nu_{LT}^m)^2 V_m V_f}{\frac{V_m}{k^f} + \frac{V_f}{k^m} + \frac{1}{G_{TT}^m}} \quad (16)$$

In-plane poisson's ratio and in-plane shear modulus are given by [23,24],

$$\nu_{LT} = \nu_{LT}^f V_f + \nu_{LT}^m V_m + \frac{(\nu_{LT}^f - \nu_{LT}^m)(1/k^m - 1/k^f) + V_f V_m}{\frac{V_m}{k^f} + \frac{V_f}{k^m} + \frac{1}{G_{TT}^m}} \quad (17)$$

$$G_{LT} = G_{LT}^m \frac{G_{LT}^m V_m + G_{LT}^f (1 + V_f)}{G_{LT}^m (1 + V_f) + G_{LT}^f V_m} \quad (18)$$

The bounds for shear modulus transverse/transverse are given by [23,24],

The lower bound:

$$G_{TT(-)} = G_{TT}^m + \frac{V_f}{\frac{1}{G_{TT}^f - G_{TT}^m} + \frac{k^m + 2G_{TT}^m V_m}{2G_{TT}^m k^m + G_{TT}^m}} \quad (19)$$

The bounds for shear modulus transverse/transverse are given by [23,24],

The upper bound:

$$G_{TT(+)} = G_{TT}^m \left(1 + \frac{1 + \beta_1 V_f}{\partial - V_f \left\{ 1 + \frac{3\beta_1^2 V_m^2}{\alpha V_f^3 + 1} \right\}} \right) \quad (20)$$

When,

$$G_{TT}^f > G_{TT}^m \text{ and } k^f > k^m$$

and,

$$G_{TT(+)} = G_{TT}^m + \frac{V_f}{\frac{1}{G_{TT}^f - G_{TT}^m} + \frac{k^m + 2G_{TT}^m V_m}{2G_{TT}^m k^m + G_{TT}^m}} \quad (21)$$

$$G_{TT(-)} = G_{TT}^m \left(1 + \frac{1 + \beta_1 V_f}{\partial - V_f \left\{ 1 + \frac{3\beta_1^2 V_m^2}{\alpha V_f^3 - \beta_1} \right\}} \right) \quad (22)$$

When,

$$G_{TT}^f < G_{TT}^m \text{ and } k^f < k^m$$

Here,

$$\alpha = \frac{\beta_1 - \gamma\beta_2}{1 + \gamma\beta_2} \quad (23)$$

$$\partial = \frac{\gamma + \beta_1}{\gamma - 1} \quad (24)$$

$$\beta_1 = \frac{k^m}{k^m + 2G_{TT}^m} \quad (25)$$

$$\beta_2 = \frac{k^f}{k^f + 2G_{TT}^f} \quad (26)$$

$$\gamma = \frac{G_{TT}^f}{G_{TT}^m} \quad (27)$$

$$V_m = 1 - V_f \quad (28)$$

The bounds of E_T are given by [23,24],

$$E_{T(\pm)} = \frac{4kG_{TT(\pm)}}{k + mG_{TT(\pm)}} \quad (29)$$

where,

$$m = 1 + \frac{4k\nu_{LT}^2}{E_L} \quad (30)$$

One can see how Rule of Mixtures underestimates the transverse properties of a composite material by plotting the results versus fiber volume fraction. The following example is for T300 Carbon / Araldite LY5052.

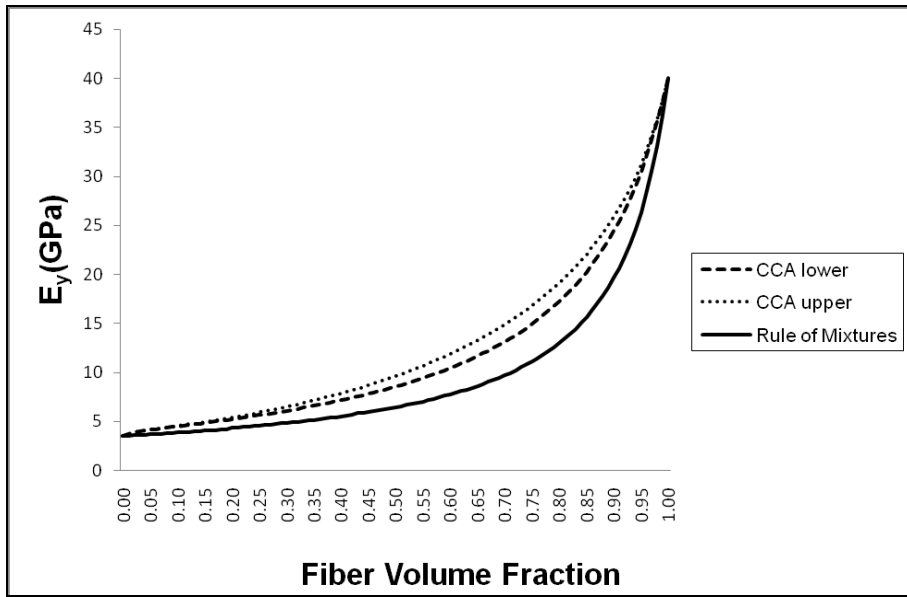


Figure 26: Comparison of CCA and RoM for E_y

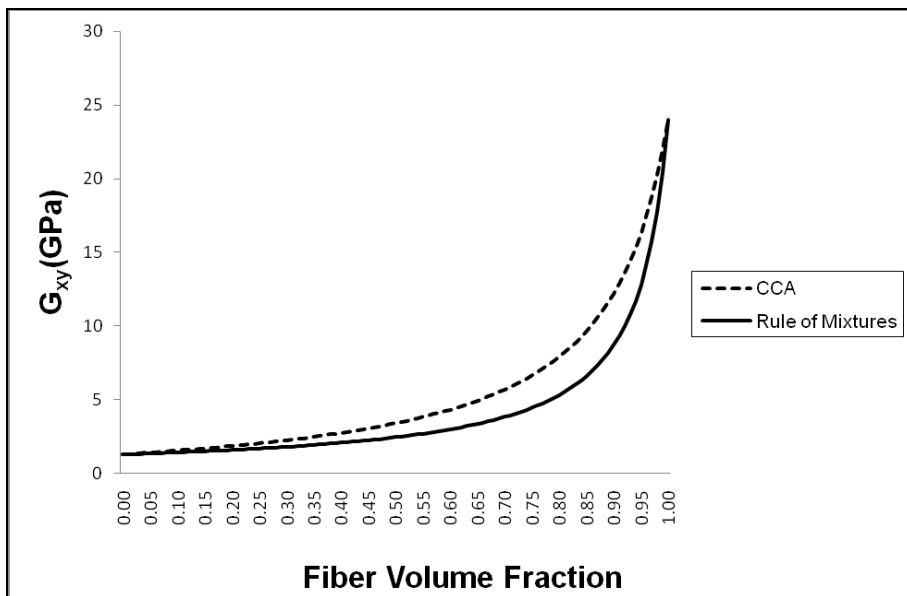


Figure 27: Comparison of CCA and RoM for G_{xy}

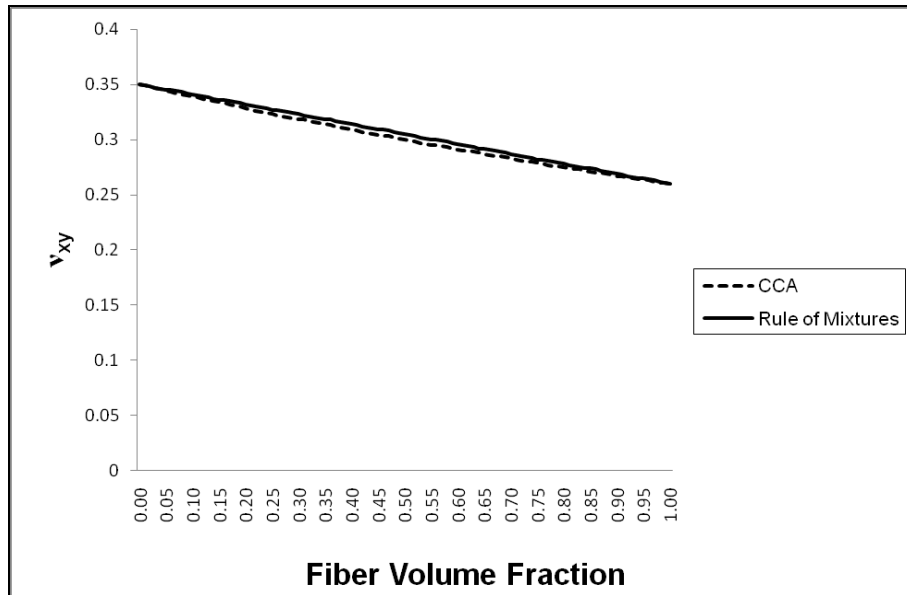


Figure 28: Comparison of CCA and RoM for v_{xy}

4.3.2.2. Mini Level Analysis

4.3.2.2.1. Geometric Model of the Unit Cell

The minimum sized periodic sample is called the unit cell of the woven fabric composite. It is also called Repetitive Volume Element in literature. Unit cell distinguishes the areas of resin and yarns and describes the undulation of the yarns. When describing the geometry of the fabric composite, it is considered as a flat ply with constant thickness. In an idealized plain weave WF composite there are three regions. They are impregnated weft and warp yarns having nonundulated and undulated regions and also resin regions. Figure 29 shows the typical geometric parameters of the unit cell of a woven fabric. For instance, in Figure 29, a_1 and b_1 represent the nonundulated region of the fill and warp yarns, respectively. In this thesis, to quantify the elastic properties of the woven fabric, the geometric shape functions of the warp and weft yarns are obtained from Falzon et.al [21].

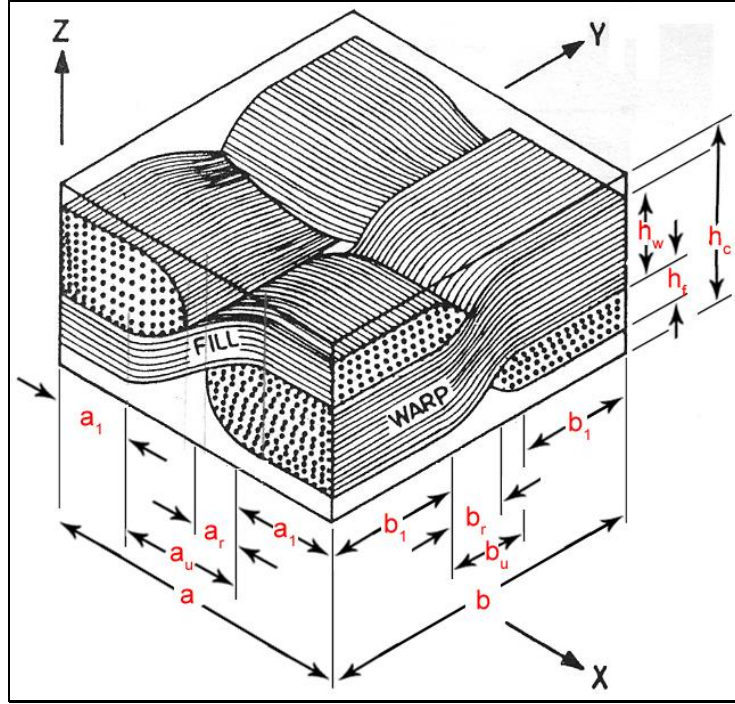


Figure 29: Dimensions in the unit cell

Warp Direction:

$$t_1(y) = \frac{-h_c}{2} \quad y: 0 \rightarrow b \quad (31)$$

$$t_2(y) = \begin{cases} \frac{-(h_f + h_w)}{2} & y: 0 \rightarrow b_1 \\ \frac{-(h_f + h_w)}{2} + \frac{h_f}{2} \left[1 + \sin \left\{ (y - b_1) \frac{\pi}{b_u} - \frac{\pi}{2} \right\} \right] & y: b_1 \rightarrow b_1 + b_u \\ \frac{-(h_w - h_f)}{2} & y: b_1 + b_u \rightarrow b \end{cases} \quad (32)$$

$$t_3(y) = \begin{cases} \frac{(h_w - h_f)}{2} & y: 0 \rightarrow b_1 \\ \frac{(h_w - h_f)}{2} + \frac{h_f}{2} \left[1 + \sin \left\{ (y - b_1) \frac{\pi}{b_u} - \frac{\pi}{2} \right\} \right] & y: b_1 \rightarrow b_1 + b_u \\ \frac{(h_w + h_f)}{2} & y: b_1 + b_u \rightarrow b \end{cases} \quad (33)$$

$$t_4(y) = \begin{cases} t_2(b_1 + b_r) - \frac{h_f}{2} \left[1 + \sin \left\{ \pi \left(\frac{b_r}{b_u} - \frac{1}{2} \right) \right\} \right] \\ \quad \times \left[\sin \left\{ (y - b_r - b_1) \frac{\pi}{2(b_u - b_r)} \right\} \right] & y: b_1 + b_r \rightarrow b_1 + b_u \quad (34) \\ -\frac{(h_w + h_f)}{2} & y: b_1 + b_u \rightarrow b \end{cases}$$

$$t_5(y) = \begin{cases} \frac{(h_w + h_f)}{2} & y: 0 \rightarrow b_1 \\ t_3(b_1 + b_u - b_r) + \frac{h_f}{2} \left[1 + \sin \left\{ \pi \left(\frac{b_r}{b_u} - \frac{1}{2} \right) \right\} \right] \\ \quad \times \left[\sin \left\{ (y - b_1) \frac{\pi}{2(b_u - b_r)} + \frac{\pi}{2} \right\} \right] & y: b_1 \rightarrow b_1 + b_u - b_r \end{cases} \quad (35)$$

$$t_6(y) = \frac{h_c}{2} \quad (36)$$

In equations (31) to (36), the main assumption is the sinusoidal variation of the warp and fill yarns in a unit cell. In Figure 29 and equations (31) to (36) the geometric parameters are defined as:

- b_u is the undulation length of the warp yarn
- b_1 is the nonundulated length of the warp yarn
- b is the warp length of the unit cell
- h_f is the maximum thickness of the weft yarn
- h_w is the maximum thickness of the warp yarn
- h_c is the overall thickness of the composite layer

Crimp angle for warp yarn is defined as [21]:

$$\theta_w(y) = \tan^{-1} \left(\frac{dt_3(y)}{dy} \right) \quad (37)$$

$$= \begin{cases} 0 & y: 0 \rightarrow b_1 \\ \left(\frac{h_f \cdot \pi}{2 \cdot b_u} \cos \left\{ (y - b_1) \frac{\pi}{b_u} - \frac{\pi}{2} \right\} \right) & y: b_1 \rightarrow b_1 + b_u \\ 0 & y: b_1 + b_u \rightarrow b \end{cases} \quad (38)$$

Weft Direction:

For the region $0 \leq y \leq b_1 + b_u - b_r$, the shape functions are given as [21]:

$$h_1(x, y) = t_1(y) \quad x: 0 \rightarrow a \quad (39)$$

$$h_2(x, y) = \begin{cases} -t_5(y) & x: 0 \rightarrow a_1 \\ -t_5(y) + \frac{(t_5(y) + t_3(y))}{2} & \\ \times \left[1 + \sin \left\{ (x - a_1) \frac{\pi}{a_u} - \frac{\pi}{2} \right\} \right] & x: a_1 \rightarrow a/2 \end{cases} \quad (40)$$

$$h_3(x, y) = \begin{cases} -t_3(y) & x: 0 \rightarrow a_1 \\ -t_3(y) + \frac{(t_5(y) + t_3(y))}{2} & \\ \times \left[1 + \sin \left\{ (x - a_1) \frac{\pi}{a_u} - \frac{\pi}{2} \right\} \right] & x: a_1 \rightarrow a/2 \end{cases} \quad (41)$$

$$h_5(x, y) = \begin{cases} -t_2(y) & x: 0 \rightarrow a_1 \\ h_3(a_1 + a_u - a_r, y) + \left[1 + \sin \left\{ (x - a_1) \frac{\pi}{2(a_u - a_r)} + \frac{\pi}{2} \right\} \right] & \\ \times \left[t_3(y) - t_2(y) - \left(\frac{t_5(y) + t_3(y)}{2} \right) \right] & \\ \times \left(1 + \sin \left\{ \pi \left(\frac{a_r}{a_u} + \frac{1}{2} \right) \right\} \right) & x: a_1 \rightarrow a_1 + a_u - a_r \end{cases} \quad (42)$$

$$h_6(x, y) = t_6(y) \quad x: 0 \rightarrow a/2 \quad (43)$$

In Figure 29 and Equations (39) to (43) the geometric parameters are defined as:

- a_u is the undulation length of the weft yarn
- a_1 is the nonundulated length of the weft yarn
- a is the weft length of the unit cell

For the region $b_1 + b_u - b_r \leq y \leq b/2$ the shape functions are given as [21]:

$$h_1(x, y) = t_1(y) \quad x: 0 \rightarrow a \quad (44)$$

$$h_3(x, y) = \begin{cases} -t_3(y) & x: 0 \rightarrow a_1 \\ -t_3(y) + \left[\frac{(t_5(b_1 + b_u - b_r) + t_3(y) - \xi(y))}{2} \right] & \\ \times \left[1 + \sin \left\{ (x - a_1) \frac{\pi}{a_u - 2\delta(y)} - \frac{\pi}{2} \right\} \right] & x: a_1 \rightarrow a/2 \end{cases} \quad (45)$$

$$h_5(x, y) = \begin{cases} -t_2(y) & x: 0 \rightarrow a_1 \\ h_3(a_1 + a_u - a_r, y) + \left[\sin \left\{ (x - a_1) \frac{\pi}{2(a_u - a_r)} + \frac{\pi}{2} \right\} \right] & \\ \times \left[\frac{t_3(y) - t_2(y)}{- \left(\frac{t_5(b_1 + b_u - b_r) + t_3(y) - \xi(y)}{2} \right)} \right] & x: a_1 \rightarrow a_1 + a_u - a_r \\ \times \left(1 + \sin \left\{ \pi \left(\frac{(a_u - a_r)}{a_u - 2\delta(y)} + \frac{1}{2} \right) \right\} \right) & \end{cases} \quad (46)$$

$$h_6(x, y) = t_6(y) \quad x: 0 \rightarrow a \quad (47)$$

where

$$\xi(y) = (t_5(b_1 + b_u - b_r) - t_3(y)) \left(\sin \left\{ (b_1 + b_u - b_r - y) \frac{\pi}{b_u - 2b_r} \right\} \right) \quad (48)$$

and

$$\delta(y) = \left[a_r - \frac{a_u}{2} \right] \left(\sin \left\{ (b_1 + b_u - b_r - y) \frac{\pi}{b_u - 2b_r} \right\} \right) \quad (49)$$

Crimp angle for weft yarn is defined as [21]:

$$\theta_w(y) = \tan^{-1} \left(\frac{dh_3(y)}{dy} \right) \quad (50)$$

$$= \begin{cases} \left(\frac{(t_5(y) + t_3(y)) \cdot \pi}{2} \cos \left\{ (x - a_1) \frac{\pi}{a_u} - \frac{\pi}{2} \right\} \right) & y: 0 \rightarrow b_1 \\ 0 & y: b_1 \rightarrow b_1 + b_u - b_r \end{cases} \quad (51)$$

Using the shape functions given above the geometric model of the WF composite used in METU TUAV was constructed. First of all, the geometric parameters of the woven carbon fiber/epoxy used in the manufacturing of the wing were obtained by digital microscope photography in the Department of Biological Sciences in METU. The digital microscope is shown in Figure 30 and taken photograph for graphite/epoxy composite is shown in Figure 31.



Figure 30: Digital microscope in the Department of Biological Sciences

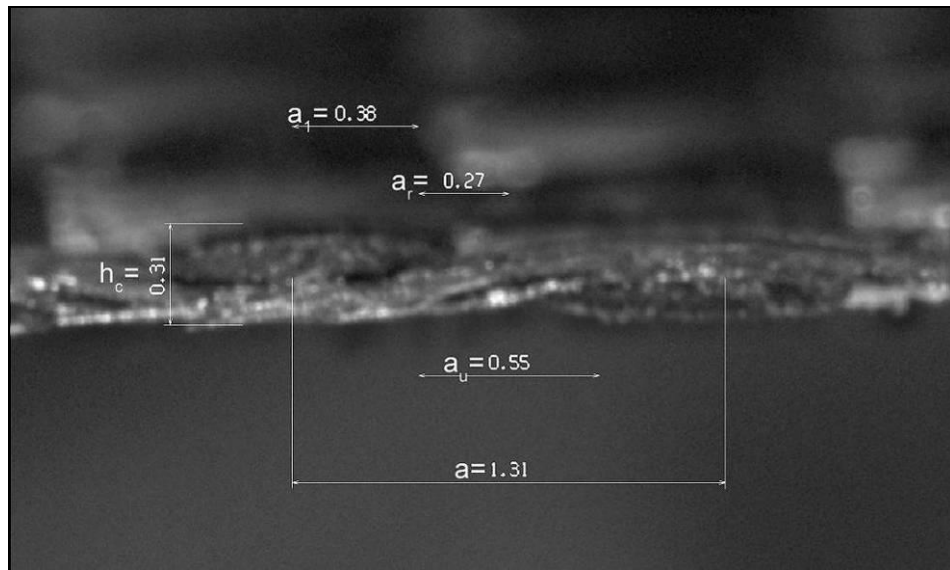


Figure 31: Photograph of T300 Carbon/Epoxy under microscope

According to measurements, the geometric parameters are tabulated in Table 9. The symbols corresponding to the lengths in unit cell can be recalled from Figure 29.

Table 9: Geometric properties of unit cells of the woven fabrics which are used in METU TUAV

		WF Composite Type		
		T300 Carbon/Epoxy		
Geometric Properties (in mm.)	h_c	0.31	b	1.31
	h_w	0.155	a_u	0.55
	h_f	0.155	a_1	0.38
	b_u	0.55	a_r	0.27
	b_1	0.38	a	1.31
	b_r	0.27		

4.3.2.2.2. Point-Wise Lamination Theory

Point-Wise Lamination Theory is based on the assumption that the Classical Lamination Theory (CLT) can be applied to the unit cell of the WF composite in a point-wise fashion. Unit cells are characteristic repetitive units of the WF composites therefore one can determine the mechanical properties of the WF composite by determining the mechanical properties of its unit cell. The constitutive equation for the in-plane mechanical properties for the unit cell is:

$$\begin{Bmatrix} N_i \\ M_i \end{Bmatrix} = \begin{bmatrix} A_{ij}(x, y) & B_{ij}(x, y) \\ B_{ij}(x, y) & D_{ij}(x, y) \end{bmatrix} \begin{Bmatrix} \varepsilon_j^0 \\ \kappa_j \end{Bmatrix} \quad (i, j = 1, 2, 6) \quad (52)$$

where;

N_i are membrane stresses

M_i are moment resultants

ε_j^0 are midsurface strains

κ_j^0 are curvatures of the laminate's geometrical mid-plane

Extensional stiffness matrix $A_{ij}(x, y)$ is obtained from

$$A_{ij}(x, y) = \int_{-h/2}^{h/2} Q_{ij}^{\alpha} \cdot dz \quad (i, j = 1, 2, 6) \quad (53)$$

Bending-extensional coupling stiffness matrix $B_{ij}(x, y)$ is obtained from

$$B_{ij}(x, y) = \int_{-h/2}^{h/2} z \cdot Q_{ij}^{\alpha} \cdot dz \quad (i, j = 1, 2, 6) \quad (54)$$

Bending Stiffness matrix $D_{ij}(x, y)$ is obtained from

$$D_{ij}(x, y) = \int_{-h/2}^{h/2} z^2 \cdot Q_{ij}^{\alpha} \cdot dz \quad (i, j = 1, 2, 6) \quad (55)$$

Q_{ij}^{α} is the plane stress-reduced stiffness matrix and is obtained from

$$Q_{ij}^{\alpha} = \begin{bmatrix} \frac{E_x^{\alpha}}{D} & \frac{\nu_{xy}^{\alpha} E_x^{\alpha}}{D} & 0 \\ \frac{\nu_{xy}^{\alpha} E_x^{\alpha}}{D} & \frac{E_y^{\alpha}}{D} & 0 \\ 0 & 0 & G_{xy}^{\alpha} \end{bmatrix} \quad (i, j = 1, 2, 6) \quad (56)$$

Where $D = 1 - \nu_{xy}^{\alpha} \cdot \nu_{yx}^{\alpha}$ and α refers for weft yarn, warp yarn or matrix medium.

Effective elastics constants for impregnated weft yarn [25],

$$E_x^f(\theta_f) = \left[\frac{l_{\theta}^4}{E_1} + \left(\frac{1}{G_{13}} - \frac{2\nu_{13}}{E_1} \right) l_{\theta}^2 m_{\theta}^2 + \frac{m_{\theta}^4}{E_3} \right]^{-1} \quad (57)$$

$$E_y^f(\theta_f) = E_2 \quad (58)$$

$$\nu_{xy}^f(\theta_f) = E_x^f(\theta_f) \left[\frac{l_{\theta}^2 \cdot \nu_{12}}{E_1} + \frac{m_{\theta}^2 \cdot \nu_{32}}{E_3} \right] \quad (59)$$

$$G_{xy}^f(\theta_f) = \left[\frac{m_\theta^2}{G_{23}} + \frac{l_\theta^2}{G_{12}} \right]^{-1} \quad (60)$$

where

$$l_\theta = \cos(\theta_f(x, y))$$

$$m_\theta = \sin(\theta_f(x, y))$$

Effective elastic constants for impregnated warp yarn [25],

$$E_y^w(\theta_w) = \left[\frac{l_\theta^4}{E_1} + \left(\frac{1}{G_{13}} - \frac{2\nu_{13}}{E_1} \right) l_\theta^2 m_\theta^2 + \frac{m_\theta^4}{E_3} \right]^{-1} \quad (61)$$

$$E_y^w(\theta_w) = E_2 \quad (62)$$

$$\nu_{xy}^w(\theta_w) = E_x^w(\theta_w) \left[\frac{l_\theta^2 \cdot \nu_{12}}{E_1} + \frac{m_\theta^2 \cdot \nu_{32}}{E_3} \right] \quad (63)$$

$$G_{xy}^w(\theta_w) = \left[\frac{m_\theta^2}{G_{23}} + \frac{l_\theta^2}{G_{12}} \right]^{-1} \quad (64)$$

where

$$l_\theta = \cos(\theta_w(x, y))$$

$$m_\theta = \sin(\theta_w(x, y))$$

Equations (53) (54) (55) can be written as a superposition of weft yarn, warp yarn and matrix regions.

$$A_{ij}(x, y) = \int_{h_4(x, y)}^{h_2(x, y)} Q_{ij}^m \cdot dz + \int_{h_2(x, y)}^{h_3(x, y)} Q_{ij}^f(\theta_f) \cdot dz + \int_{h_3(x, y)}^{h_5(x, y)} Q_{ij}^w(\theta_w) \cdot dz + \int_{h_5(x, y)}^{h_6(x, y)} Q_{ij}^m \cdot dz \quad (65)$$

$$\begin{aligned}
B_{ij}(x, y) &= \int_{h_1(x, y)}^{h_2(x, y)} Q_{ij}^m \cdot z \cdot dz + \int_{h_2(x, y)}^{h_3(x, y)} Q_{ij}^f(\theta_f) \cdot z \cdot dz \\
&+ \int_{h_3(x, y)}^{h_5(x, y)} Q_{ij}^w(\theta_w) \cdot z \cdot dz + \int_{h_5(x, y)}^{h_6(x, y)} Q_{ij}^m \cdot z \cdot dz
\end{aligned} \tag{66}$$

$$\begin{aligned}
D_{ij}(x, y) &= \int_{h_1(x, y)}^{h_2(x, y)} Q_{ij}^m \cdot z^2 \cdot dz + \int_{h_2(x, y)}^{h_3(x, y)} Q_{ij}^f(\theta_f) \cdot z^2 \cdot dz \\
&+ \int_{h_3(x, y)}^{h_5(x, y)} Q_{ij}^w(\theta_w) \cdot z^2 \cdot dz + \int_{h_5(x, y)}^{h_6(x, y)} Q_{ij}^m \cdot z^2 \cdot dz
\end{aligned} \tag{67}$$

For region $0 \leq y \leq b_1 + b_u - b_r$ and $0 \leq x \leq a_1 + a_u - a_r$,

$$\begin{aligned}
A_{ij}(x, y) &= Q_{ij}^f(\theta_f) [h_3(x, y) - h_2(x, y)] + Q_{ij}^w(\theta_w) [h_5(x, y) - h_3(x, y)] \\
&+ Q_{ij}^m [h_2(x, y) - h_1(x, y) + h_6(x, y) - h_5(x, y)]
\end{aligned} \tag{68}$$

$$\begin{aligned}
B_{ij}(x, y) &= \frac{Q_{ij}^f(\theta_f)}{2} [h_3^2(x, y) - h_2^2(x, y)] + \frac{Q_{ij}^w(\theta_w)}{2} [h_5^2(x, y) - h_3^2(x, y)] \\
&+ \frac{Q_{ij}^m}{2} [h_2^2(x, y) - h_1^2(x, y) + h_6^2(x, y) - h_5^2(x, y)]
\end{aligned} \tag{69}$$

$$\begin{aligned}
D_{ij}(x, y) &= \frac{Q_{ij}^f(\theta_f)}{3} [h_3^3(x, y) - h_2^3(x, y)] + \frac{Q_{ij}^w(\theta_w)}{3} [h_5^3(x, y) - h_3^3(x, y)] \\
&+ \frac{Q_{ij}^m}{2} [h_2^3(x, y) - h_1^3(x, y) + h_6^3(x, y) - h_5^3(x, y)]
\end{aligned} \tag{70}$$

For region $0 \leq y \leq b_1 + b_u - b_r$ and $a_1 + a_u - a_r \leq x \leq a/2$,

$$\begin{aligned}
A_{ij}(x, y) &= Q_{ij}^f(\theta_f) [h_3(x, y) - h_2(x, y)] \\
&+ Q_{ij}^m [h_2(x, y) - h_1(x, y) + h_6(x, y) - h_5(x, y)]
\end{aligned} \tag{71}$$

$$\begin{aligned}
B_{ij}(x, y) &= \frac{Q_{ij}^f(\theta_f)}{2} [h_3^2(x, y) - h_2^2(x, y)] \\
&+ \frac{Q_{ij}^m}{2} [h_2^2(x, y) - h_1^2(x, y) + h_6^2(x, y) - h_5^2(x, y)]
\end{aligned} \tag{72}$$

$$\begin{aligned}
D_{ij}(x, y) &= \frac{Q_{ij}^f(\theta_f)}{3} [h_3^3(x, y) - h_2^3(x, y)] \\
&+ \frac{Q_{ij}^m}{2} [h_2^3(x, y) - h_1^3(x, y) + h_6^3(x, y) - h_5^3(x, y)]
\end{aligned} \tag{73}$$

For region $b_1 + b_u - b_r \leq y \leq b/2$ and $0 \leq x \leq a_1 + a_u - a_r$,

$$\begin{aligned}
A_{ij}(x, y) &= Q_{ij}^w(\theta_w) h_5(x, y) - h_3(x, y) \\
&+ Q_{ij}^m h_2(x, y) - h_1(x, y) + h_6(x, y) - h_5(x, y)
\end{aligned} \tag{74}$$

$$\begin{aligned}
B_{ij}(x, y) &= \frac{Q_{ij}^w(\theta_w)}{2} [h_5^2(x, y) - h_3^2(x, y)] \\
&+ \frac{Q_{ij}^m}{2} [h_2^2(x, y) - h_1^2(x, y) + h_6^2(x, y) - h_5^2(x, y)]
\end{aligned} \tag{75}$$

$$\begin{aligned}
D_{ij}(x, y) &= \frac{Q_{ij}^w(\theta_w)}{3} [h_5^3(x, y) - h_3^3(x, y)] \\
&+ \frac{Q_{ij}^m}{2} [h_2^3(x, y) - h_1^3(x, y) + h_6^3(x, y) - h_5^3(x, y)]
\end{aligned} \tag{76}$$

For region $b_1 + b_u - b_r \leq y \leq b/2$ and $a_1 + a_u - a_r \leq x \leq a/2$,

$$A_{ij}(x, y) = Q_{ij}^m h_2(x, y) - h_1(x, y) + h_6(x, y) - h_5(x, y) \tag{77}$$

$$B_{ij}(x, y) = \frac{Q_{ij}^m}{2} [h_2^2(x, y) - h_1^2(x, y) + h_6^2(x, y) - h_5^2(x, y)] \tag{78}$$

$$D_{ij}(x, y) = \frac{Q_{ij}^m}{2} \left[h_2^3(x, y) - h_1^3(x, y) + h_6^3(x, y) - h_5^3(x, y) \right] \quad (79)$$

4.3.2.2.3. Averaging Schemes for the Stiffness Matrices

In the previous section stiffness matrices are obtained for different regions. In order to get unique constants for the woven fabric composite, these matrices should be averaged inside the unit cell. This procedure can be done in different ways; by averaging stiffness matrices, by averaging compliance matrices or by averaging both of them. Elastic constants are obtained from averaging extensional stiffness matrix $A_{ij}(x, y)$ only.

4.3.2.2.3.1. Series-Parallel Model

In Series-Parallel Model which was used by Naik and Shembekar [10], the elements along the loading direction are assembled with an iso-stress condition. This condition is satisfied by averaging the in-plane compliance matrix in the direction of the applied uniform stress.

Here $a_{ij}(x, y)$ is the in-plane compliance matrix which can be calculated by matrix inversion of the extensional stiffness matrix, $A_{ij}(x, y)$.

$$a_{ij}(x, y) = A_{ij}(x, y)^{-1} \quad (80)$$

Spatial averaging the compliance matrix in x-direction gives,

$$\bar{a}_{ij}^{-s}(y) = \frac{1}{a} \int_0^a a_{ij}(x, y) \cdot dx \quad (81)$$

Then by taking the inverse of the averaged compliance matrix and by spatial averaging (in y-direction) the stiffness matrix which is obtained from matrix inversion,

$$\bar{A}_{ij}^{-s}(y) = \bar{a}_{ij}^{-s}(y)^{-1} \quad (82)$$

$$\bar{A}_{ij}^{-sp} = \frac{1}{b} \int_0^b \bar{A}_{ij}^{-s}(y) \cdot dy \quad (83)$$

By means of these double averaging, averaged stiffness matrix is obtained. Matrix inversion of the averaged stiffness matrix yields to averaged compliance matrix.

$$\bar{a}_{ij}^{-sp} = \bar{A}_{ij}^{-sp-1} \quad (84)$$

Thus, one can find the elastic constants of the WF composite using compliance matrix through Equations (85) to (88) [21].

$$E_x = \frac{1}{h_c \cdot \bar{a}_{11}^{-sp}} \quad (85)$$

$$E_y = \frac{1}{h_c \cdot \bar{a}_{22}^{-sp}} \quad (86)$$

$$\nu_{xy} = -\frac{\bar{a}_{12}^{-sp}}{\bar{a}_{11}^{-sp}} \quad (87)$$

$$G_{xy} = \frac{1}{\bar{a}_{66}^{-sp}} \quad (88)$$

4.3.2.2.3.2. Parallel-Series Model

Similarly Parallel-Series Model which was used by Naik and Shembekar [10], the elements normal to the loading direction are assembled with an iso-strain condition. This condition is satisfied by averaging the coefficients of the in-plane stiffness matrix in the direction of the applied uniform stress.

Spatial averaging the compliance matrix in y-direction gives,

$$\bar{A}_{ij}^p(x) = \frac{1}{b} \int_0^b A_{ij}(x, y) \cdot dy \quad (89)$$

Then, by taking the inverse of the averaged stiffness matrix and spatial averaging (in x-direction) the compliance matrix is obtained from matrix inversion,

$$\bar{a}_{ij}^p(x) = \bar{A}_{ij}^p(x)^{-1} \quad (90)$$

$$\bar{a}_{ij}^{-ps} = \frac{1}{a} \int_0^a \bar{a}_{ij}^p(x) \cdot dx \quad (91)$$

Once the averaged compliance matrix is found, elastic constants of the WF can be found similarly to the previous model.

$$E_x = \frac{1}{h_c \cdot \bar{a}_{11}^{-ps}} \quad (92)$$

$$E_y = \frac{1}{h_c \cdot \bar{a}_{22}^{-ps}} \quad (93)$$

$$\nu_{xy} = -\frac{\bar{a}_{12}^{-ps}}{\bar{a}_{11}^{-ps}} \quad (94)$$

$$G_{xy} = \frac{1}{\bar{a}_{66}^{-ps}} \quad (95)$$

4.3.2.2.3.3. Series-Series Model

Series-Series Model assumes iso-stress condition in both direction and elastic constants are obtained on the basis of principle of minimum complementary energy. Thus it gives the lower bound of the elastic constants. The procedure is based on double averaging the compliance matrix which is found by matrix inversion of the stiffness matrix. Once the averaged compliance matrix is found, elastic constants of the WF composite can be found.

$$a_{ij}(x, y) = A_{ij}(x, y)^{-1} \quad (96)$$

$$\bar{a}_{ij}^{-ss} = \frac{1}{a \cdot b} \int_0^a \int_0^b a_{ij}(x, y) \cdot dy \cdot dx \quad (97)$$

Therefore,

$$E_x = \frac{1}{h_c \cdot \bar{a}_{11}^{-ss}} \quad (98)$$

$$E_y = \frac{1}{h_c \cdot \bar{a}_{22}^{-ss}} \quad (99)$$

$$v_{xy} = -\frac{\bar{a}_{12}^{-ss}}{\bar{a}_{11}^{-ss}} \quad (100)$$

$$G_{xy} = \frac{1}{\bar{a}_{66}^{-ss}} \quad (101)$$

4.3.2.2.3.4. Parallel-Parallel Model

Parallel-Parallel Model assumes iso-strain condition in both direction and elastic constants are obtained on the basis of principle of minimum potential energy. Thus it gives the upper bound of the elastic constants. The procedure is based on double averaging the stiffness matrix. Once the averaged stiffness matrix is found, taking the matrix inversion of it yields to the averaged compliance matrix. Elastic constants of the WF composite can be found using averaged compliance matrix.

$$\bar{A}_{ij}^{pp} = \frac{1}{a \cdot b} \int_0^a \int_0^b A_{ij}(x, y) \cdot dy \cdot dx \quad (102)$$

$$\bar{a}_{ij}^{-pp} = \bar{A}_{ij}^{pp-1} \quad (103)$$

Therefore,

$$E_x = \frac{1}{h_c \cdot a_{11}^{-pp}} \quad (104)$$

$$E_y = \frac{1}{h_c \cdot a_{22}^{-pp}} \quad (105)$$

$$\nu_{xy} = -\frac{a_{12}^{-pp}}{a_{11}^{-pp}} \quad (106)$$

$$G_{xy} = \frac{1}{a_{66}^{-pp}} \quad (107)$$

4.3.2.2.4. Results of the Mini-Level Analysis

In order to calculate the elastic constants of the woven fabric composites, using the geometric shape functions and averaging schemes presented in the previous sections, a FORTRAN 77 code was written. By using the shape functions given in section 4.3.2.2.1, the elastic coefficients are calculated by numerically integrating the averaged stiffness and compliance coefficients for different averaging schemes described in the previous section. Trapezoidal numerical integration scheme was used to perform the numerical integrations, and the step sizes were chosen small enough to have a little numerical error. The effects of the integration order in series-parallel and parallel-series are also investigated and it is found that starting the integrations shown in Equation (81) and Equation (89) in $-x$ direction or $-y$ direction creates different results. The results form the upper and lower bounds for parallel-series and series-parallel schemes.

The material property inputs for the developed program are tabulated in Table 10 and the results of the program are tabulated in Table 11 for T300/Epoxy WF composite. In the structural analysis of the wing, elastic constants calculated by the upper bounds of parallel-series averaging scheme, which is the recommended model in the literature [10], has been used. The results of the numerical integrations for the elastic constants E_x , E_y , ν_{xy} , G_{xy} , were used as inputs to the FE program MSC. Patran directly when creating the 2D orthotropic material.

Table 10: Mechanical properties of fiber and matrix materials used in METU TUAV

	E_L (GPa)	E_T (GPa)	G_{LT} (GPa)	G_{TT} (GPa)	ν_{LT}
Carbon (T300)	230	40	24	14.3	0.26
Epoxy (LY5052)	3.5	3.5	1.3	1.3	0.35

Table 11: Elastic Constants for T300/Epoxy WF Composite

		E_x, E_y (GPa)	ν_{xy}	G_{xy} (GPa)
Averaging Scheme	Series-Parallel (-x integration first)	46.248	0.0614	3.393
	Series-Parallel (-y integration first)	31.456	0.0869	3.387
	Parallel-Series (-y integration first)	47.475	0.0606	3.394
	Parallel-Series (-x integration first)	31.551	0.0884	3.388
	Series-Series	26.144	0.1002	3.347
	Parallel-Parallel	47.920	0.0513	3.433

CHAPTER 5

STRUCTURAL ANALYSIS OF METU TUAV'S WING WITH FEA

5.1. Introduction

Finite element analysis is a popular numerical method for solving structural mechanics problems. With the growing computational capabilities of computers, more complex finite element models can be constructed nowadays. Structural analysis of METU TUAV's wing is done using MSC. MD Nastran 2006 solver. Preprocessing and post processing of the model is done using MSC. Patran 2006. The success of the finite element analysis depends on how much the created finite element model and inputs reflect the real life cases. In Chapter 3, the aerodynamic loading around the wing was found via CFD which gave accurate force resultants and distributions. In Chapter 4, the material properties of the woven composites layers, which are used in manufacturing, are found by a detailed unit cell analysis. Last but not the least boundary conditions should be chosen very carefully. Although loading and materials are modeled very good, without proper boundary conditions the analysis will become inconsistent with the real case. To understand the response of the structure to boundary conditions, different boundary condition sets are tried and the most proper one, which is deemed to reflect the real case, is selected. In structural analysis of the wing, static analysis of the wing is done in two different loading conditions. These loading conditions are Positive High Angle of Attack (PHA) and Positive Low Angle of Attack (PLA) conditions which are explained in Chapter 2 in details. In addition, a dynamic analysis of the composite wing has also been performed. Firstly a modal analysis has been done to determine the natural frequencies and the related mode shapes. Secondly a frequency response analysis of the wing has done to see responses to a varying force at different locations. Apart from static and dynamic analysis of the wing, finite element model has been used for determining the torsional stiffness of the wing. Then using this

value and other parameters the torsional divergence velocity of METU TUAV has been found.

5.2. Description of the Model

The geometric model of the wing is prepared using a CAD program CATIA V5. Then these geometries are exported to Gambit for meshing purposes in STEP file format. After the interpolation procedure which is explained in Chapter3 in detail, the model is imported into MSC. Patran. In order to handle the different zones of the wing easily, grouping is done. The groups used in the model can be seen in Figure 32 and Figure 33 and the details are tabulated in Table 12.

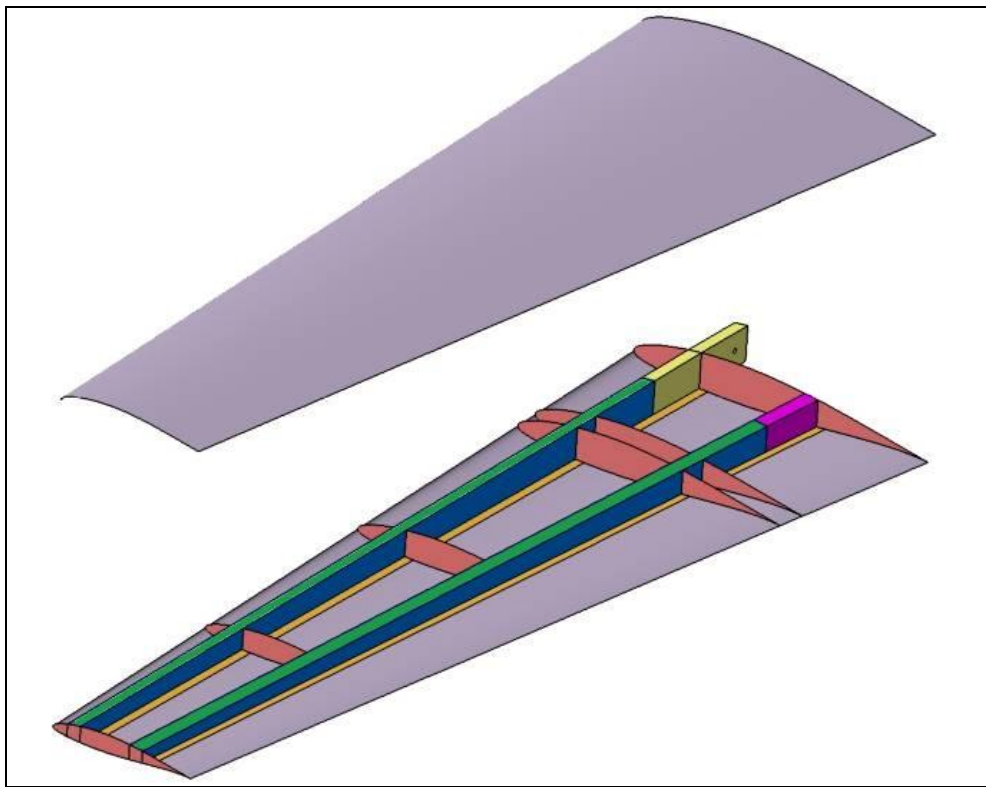


Figure 32: Color coded zones in wing model

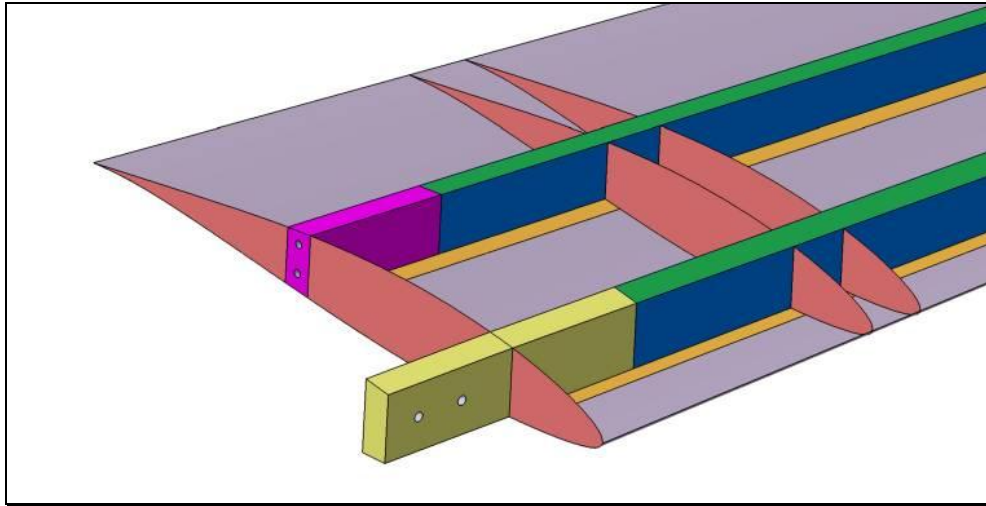


Figure 33: Detailed view of spar-body connection areas

Table 12: Property table of the FE model

Color	Group	Material	Element Type
Yellow	Front spar-body connection	Hornbeam	Solid / Tetrahedron / Tet4
Pink	Rear spar-body connection	Aluminum 7075-T6	Solid / Tetrahedron / Tet4
Blue	Spar webs	Carbon-epoxy composite	Shell / Quadrilateral / Quad4
Green	Upper spar flanges	Carbon-epoxy composite	Shell / Quadrilateral / Quad4
Purple	Lower and upper skins	E-glass-epoxy / Rohacell sandwich construction	Shell / Quadrilateral / Quad4
Orange	Lower spar flanges (includes the lower skin sandwich layers)	E-glass-epoxy / Rohacell sandwich construction + Carbon-epoxy composite	Shell / Quadrilateral / Quad4
Red	Ribs	Carbon-epoxy composite	Shell / Triangular / Tri3 & Shell / Quadrilateral / Quad4

In the model, spar flanges (green) and spar webs (blue) extend on solid connection blocks (pink and yellow) but they are not shown in Figure 32 and Figure 33 for a clearer visualization. The detail for front spar connection is shown in Figure 34.

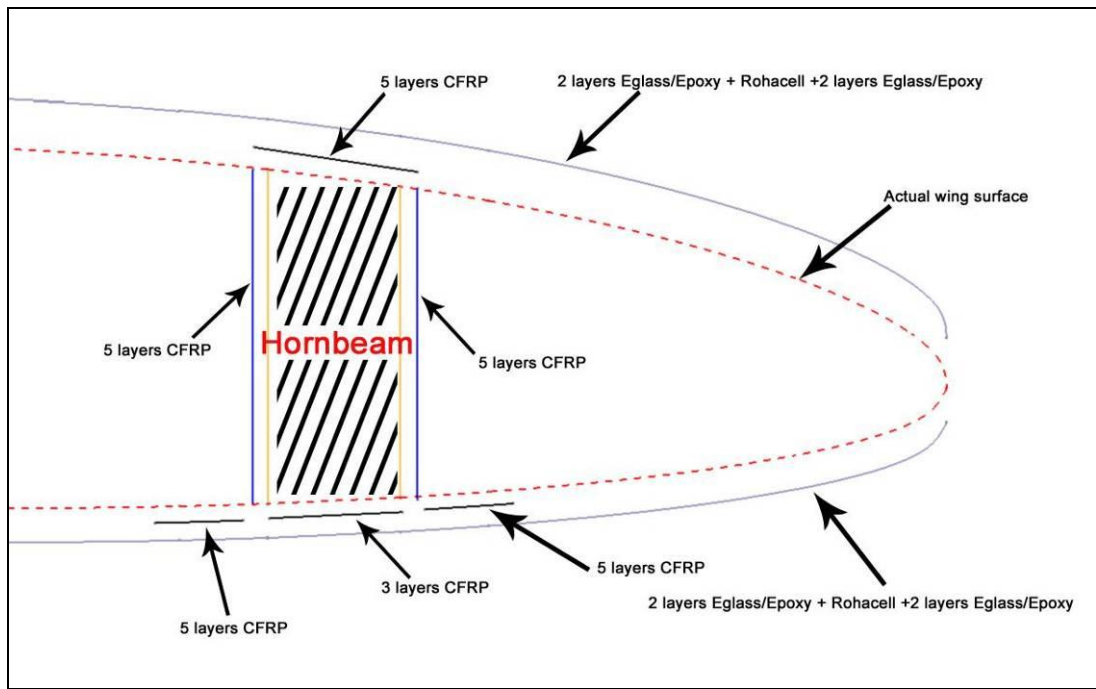


Figure 34: The detail of front spar connection in FE model

In Figure 33, the front spar extension, which is made of aluminum, goes inside a box which is fixed to the main bulkhead in the fuselage. On the other hand, the rear spar end, shown in pink color, is flush with the fuselage, and it is bolted to a rear bulkhead inside the fuselage through the two holes shown in Figure 33.

The effects of element size to the results are investigated via case study for static analysis in PLA case. The number of elements, maximum stresses and maximum tip deflections for fine and course meshes are tabulated in Table 13. As expected, the maximum deflections for both cases are close to each other but maximum stress values at elements are very different. Also at elements where intermediate stress values are seen, the stress values close to each other but to be in the safe side in terms of material failure fine mesh is used for the structural analyses in FEA.

Table 13: Results for different mesh sizes

CASE	Number of shell elements	Maximum stress at shell elements (MPa)	Intermediate stress value at shell elements on upper flange (MPa)	Number of solid elements	Maximum stress at solid elements (MPa)	Maximum deflection (mm)
Fine mesh	249,268	224	35	1,594,664	104	54.0
Course mesh	7,941	68	30	3,183	32	54.8

5.3. Boundary Condition Selection

METU TUAV's wing is attached to the fuselage bulkheads via cap screws. In rear spar connection, two M8 helical coils are inserted to the threaded holes of aluminum section of the rear spar. In the finite element model, translations of nodes inside these holes are constrained. In principal, helical coils are not inserted up to the end of holes. Therefore, only those nodes which are in the in the helical coil areas are constrained. In addition, the nodes on the aluminum part's free face which is in contact with fuselage in $-y$ direction are constrained in this direction because in the actual mounting, the rear spar is bolted to a bulkhead in the fuselage. During the installation when the bolts are tightened, the rear spar, shown in pink color in Figure 33, is pulled against the fuselage and the rear spar aluminum becomes constrained along the wing span direction. However, there always remains a small gap between the rest of the wing root rib and the fuselage. Therefore, except for the rear spar end, the rest of the wing root surface is left free.

Front spar is connected to the fuselage by inserting it into a box which is fixed to fuselage bulkhead. In addition, through two holes, shown in Figure 33, box and the front spar root are bolted to each other with two fasteners. When the nuts at the ends of the fasteners are tightened, the box walls are pushed against the spar end causing almost perfect contact between the box wall and the spar end. Moreover,

box is manufactured by wrapping several layers of carbon-epoxy composite on the surface of front spar. So, the outer surface of the front spar end is used as a mold to manufacture the box and this process essentially leaves no gap between the spar root and the inner mating surface of the box. Thus, the manufacturing method of the box and the tightening provided by the two bolts provide almost perfect mating of the spar root entering into the fuselage with the inner surface of the box. In the manufacturing process of the box, after the curing process ends, the box is removed from the surface of front spar by the virtue of the release agent which was applied over the spar surface before the wrapping process started. In finite element model, translation of the nodes on the surfaces which are in contact with this box is constrained but the rotations are left free. The boundary conditions for wing connection blocks are shown in Figure 35.

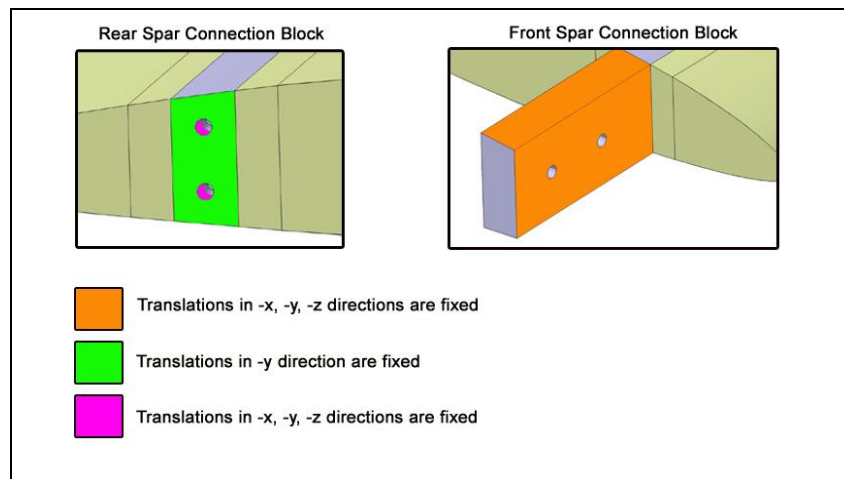


Figure 35: Boundary conditions for wing connection blocks

The choices for the boundary conditions are decided on after analyzing several cases. Two possible boundary conditions are deemed to be convenient for both front spar and rear spar. For front spar connection block, the translations are fixed but the rotations of the nodes on the surface could be either fixed or free. In addition for rear spar connection block, only the translations inside the helical coil zones are fixed but the translations of the nodes on the surface which is contact with fuselage could be either be taken as fixed or free. Two possibilities for two different zones

yield four combinations. These combinations are tabulated in Table 14 and the results are tabulated in Table 15. The results given in Table 15 were obtained for PLA load case which was not finalized at the time of calculation so these results should be taken as for comparison purposes. Some modifications in loading and material properties are done after proper boundary condition is chosen. By looking at Table 15, one can see that for Case 1 and Case 3 the maximum stresses for solid elements are high when compared to the other cases. For Case 1 and Case 3, the face in contact with the fuselage is freed and the end face of the aluminum block of the rear spar is fixed only at the helical coil areas. Therefore, high stresses occur around the helical coil holes. But as it was explained before, when the bolts fixing rear spar to the fuselage are tightened, the end aluminum block in rear spar, shown in Figure 33, is pushed against the fuselage and the y displacements along the span of the wing are constrained. For this reason, fixing the translations of the root end face of the rear spar in $-y$ direction is deemed to be convenient. On the other hand, only the displacements on the faces of the front spar root inside the box are fixed and rotations are left free. This decision was based on the assumption that after several installations and removals of the wing, there will be slight loosening in the tightness of the front spar root-fuselage box connection, and therefore it would be appropriate to let the rotations free. It should also be noted that in the front spar mating with the fuselage box, there are shell elements representing the carbon fabrics placed over the hornbeam which is modeled by solid elements. Therefore, since shell and solid elements use the same node it would also be more appropriate to let the rotations free because solid elements used in the modeling in this thesis do not have rotational degree of freedom.

Table 14: Boundary condition cases for front and rear spar connection blocks

CASE	B.C. in Front Spar Connection Block	B.C. in Rear Spar Connection Block
1	The rotations and translations are fixed	The translations in $-y$ direction of the nodes in contact with fuselage are free
2	The rotations and translations are fixed	The translations in $-y$ direction of the nodes in contact with fuselage are fixed
3	Only the translations are fixed	The translations in $-y$ direction of the nodes in contact with fuselage are free
4	Only the translations are fixed	The translations in $-y$ direction of the nodes in contact with fuselage are fixed

Table 15: Results for different boundary condition cases

CASE	Maximum stress at shell elements (MPa)	Maximum stress at solid elements (MPa)	Maximum deflection (mm)
1	160	290	62
2	157	156	61.2
3	180	291	62
4	174	157	61.2

5.4. Material Properties

Structural members of METU TUAV are constructed mostly from composite materials. The properties of carbon-epoxy composites are found from the analysis which is described in Chapter 3. The unit cells for e-glass/epoxy composite materials that are used in manufacturing are so small that they cannot be cut properly to reveal their cross-section which would be observed under microscope. Therefore the same method cannot be applied to the e-glass/epoxy composite material. Mechanical properties of similar e-glass/epoxy configurations are found from literature [26] and used in the analysis.

One assumption made in the structural analysis is about the elastic modulus of hornbeam wood. The hornbeam region in the front spar is modeled as isotropic

material although it is not. The hornbeam part which is shown in Figure 12, is composed of stacks of hornbeam layers whose fiber direction is along the wing span. In literature [27], elastic modulus of hornbeam parallel to the grain direction is found and it is used as the elastic constant of hornbeam in MSC. Patran.

Mechanical properties of the materials used in the structural analysis of METU TUAV are tabulated in Table 16 and Table 17.

Table 16: Mechanical properties of isotropic materials used in METU TUAV

	E (GPa)	ν	S_U (MPa)	ρ (tonne/mm ³)
Aluminum 7075-T6	70	0.33	524	2.71×10^{-9}
Rohacell 31A [28]	0.026	0.49	-	3.20×10^{-11}
Hornbeam	15.26	0.35	48.3	1.54×10^{-9}

Table 17: Mechanical properties of 2D orthotropic materials

	E_x (GPa)	E_y (GPa)	G_{xy} (GPa)	ν_{xy}	S_U (MPa)	ρ (tonne/mm ³)
Carbon/epoxy	47.48	47.48	3.39	0.061	403	1.21×10^{-9}
E-glass/epoxy [26]	26.40	26.40	4.82	0.125	275	1.66×10^{-9}

Table 18: Comparison of results from unit cell analysis and values from literature

	E_x (GPa)	E_y (GPa)	G_{xy} (GPa)	ν_{xy}
Carbon/epoxy used in METU TUAV	47.5	47.5	3.4	0.061
T-300 3k/934 plain weave fabric [26]	62.7	62.0	-	-
Celion 3000/E7K8 plain weave fabric [26]	63.6	65.5	-	-
HITEX 33 6k/E7K8 plain weave fabric [26]	62.8	59.6	-	0.046
AS4 6k/3502 5-harness satin weave fabric [26]	-	-	3.5	-
AS4 6k/PR 500 RTM 5-harness satin weave fabric [26]	-	-	4.4	-

The mechanical properties of carbon/epoxy laminate, which are found via unit cell analysis in Chapter 4, are compared with similar specimen results available in literature [26] and it is observed that the results from analyses are close to the specimen results as shown in Table 18.

5.5. Static Analysis of METU TUAV's Wing

The first structural analysis of METU TUAV's wing is linear static analysis which is performed using MSC. Nastran's linear static solver (NAS101). As described in Chapter 3, the net forces found from CFD analysis don't give desired 3.8g loading condition which is determined in structural design. The desired 3.8g loading condition is obtained by multiplying the load case with the necessary factor. Addition to this correction factor, 1.5 safety factor is applied to the loading condition.

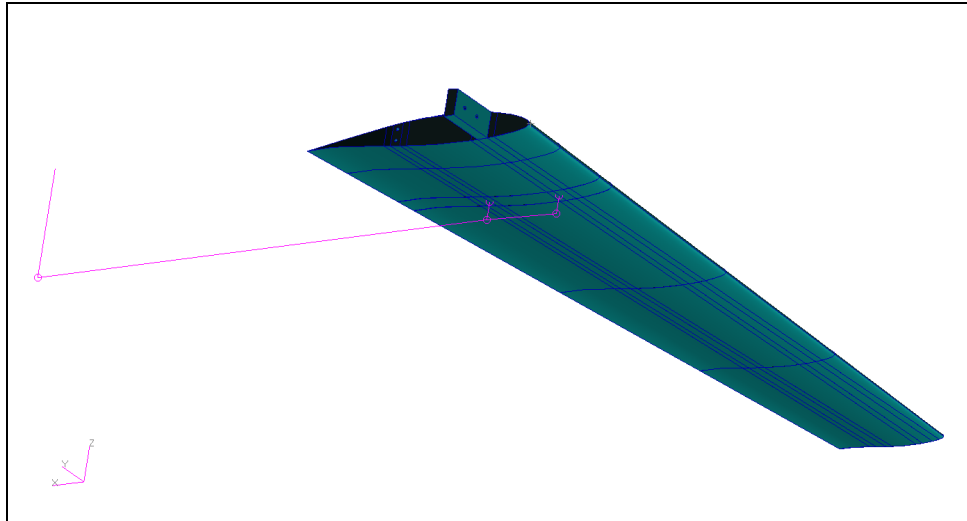


Figure 36: The finite element modeling of the tail boom

Moreover, as it is shown in Figure 2, there is also loading from horizontal tail transferred to the wing via tail boom. For PLA and PHA loading cases loading from horizontal tail is calculated with simple aerodynamic equations. For simplicity, the tail boom is modeled with rigid elements (RBE2) available in MSC. Patran's library. Then they are connected to the wing at rear spar and front spar as shown in Figure 36. The calculated horizontal tail load is applied from the tip of the tail boom. The results are given as contour plots and they are grouped according to the materials. In composite materials, the result of the layer in which the greatest stress value occurs, is shown. For each group the margin of safety (MoS) values are calculated and tabulated.

5.5.1. Results of Static Analysis at Positive Low Angle of Attack Case

Table 19 gives the margin of safety for the front spar. The most critical stress is seen to occur on the hornbeam at the corner where the spar enters into the box.

Table 19: MoS value for front spar in PLA case

Group	Material	Margin of Safety (%)
Front Spar	Hornbeam	10

Figure 37 shows the von Mises stress contours for the front spar core material in PLA case. It can be seen that maximum stress is below the ultimate tensile strength of the hornbeam. As Figure 37 shows, the peak stresses occur at the junction where the front spar enters into the box in the fuselage. The location for the peak stress was expected because just outside the box the displacements are relaxed on the outer periphery of the front spar resulting in high displacement gradient which in turn generates high stresses.

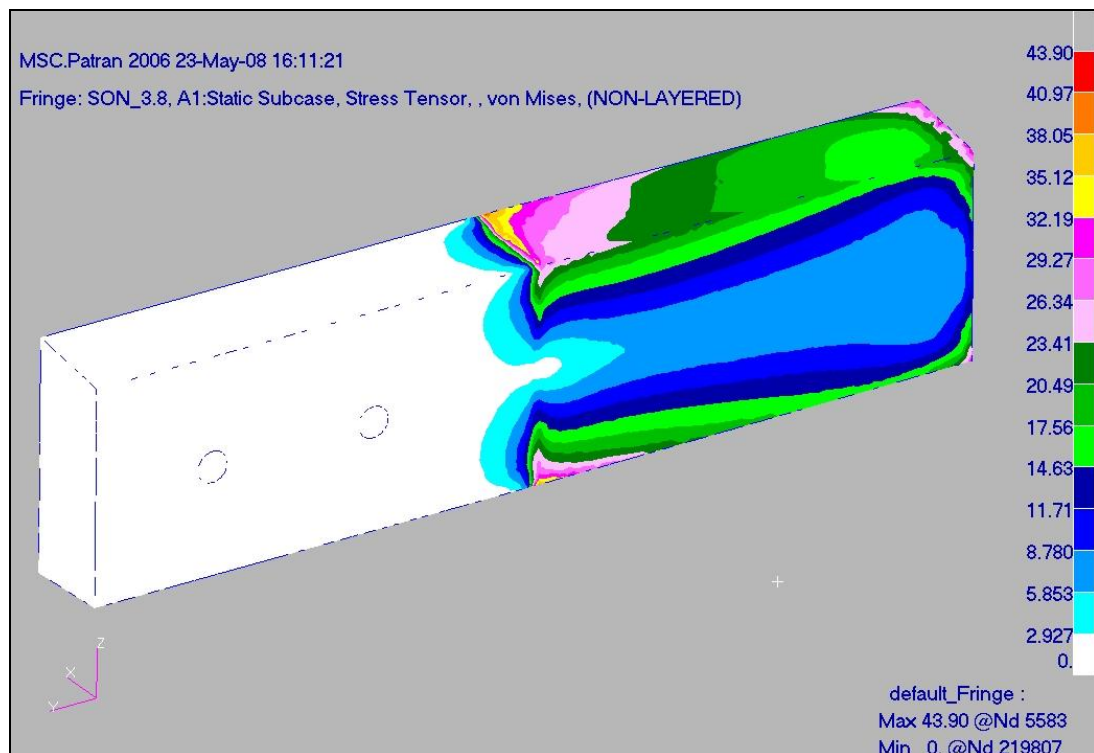


Figure 37: von Mises stress contours for front spar core material in PLA case

Table 20 gives the margin of safety for the rear spar. The most critical stress is seen to occur on the end aluminum which is used as the core material at the root part of the rear spar as shown in Figure 33. The critical stress point was at the corner where the aluminum ends and this is shown in the von Mises stress plot given in Figure 38. The location of the maximum stress was expected because at that section there is sudden change in the stiffness in the rear spar. The composite layers which are wrapped around the aluminum end block extend all the way to the

tip forming the box structure of the rear spar of the wing. Thus, there is sudden change in the core material and this account for a sudden change in the stiffness of the rear spar resulting in peak stresses.

Table 20: MoS value for rear spar in PLA case

Group	Material	Margin of Safety (%)
Rear Spar	Aluminum 7075-T6	353

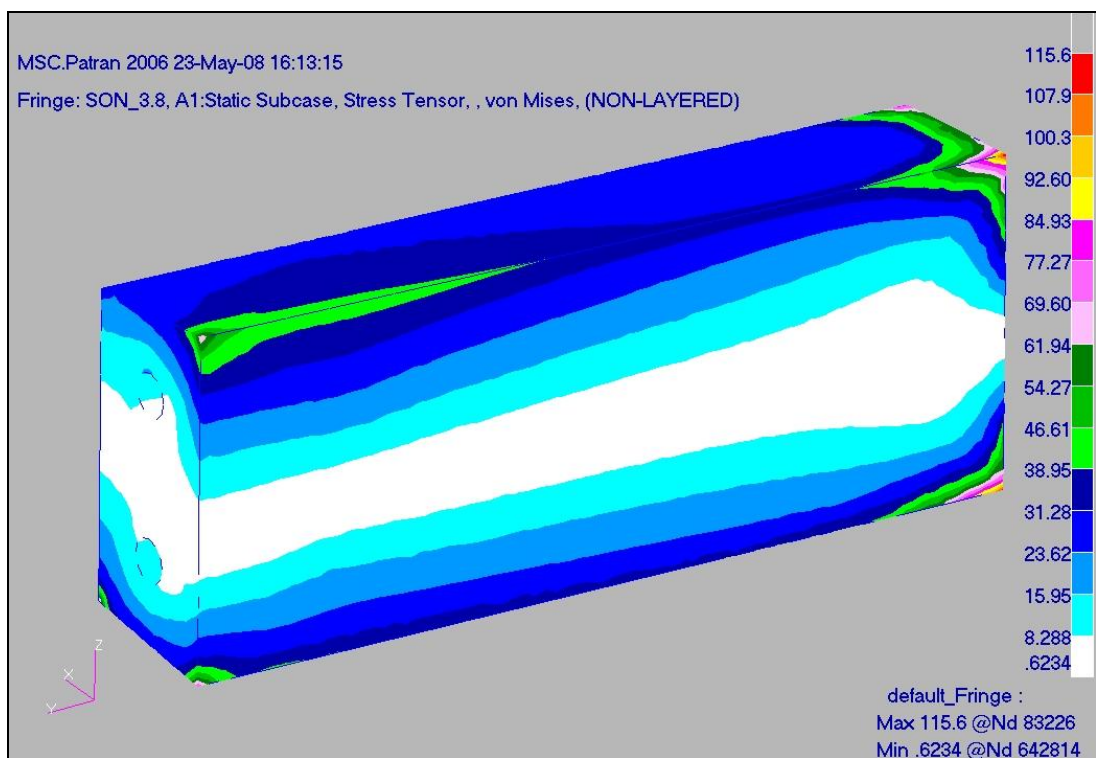


Figure 38: von Mises stress contours for rear spar in PLA case

Table 21 and Table 22 present the MoS values for the skin layers for the PLA case.

Table 21: MoS values for upper skin layers in PLA case

Group	Material	Margin of Safety (%)
Upper skin (layer1)	E-glass/epoxy	115
Upper skin (layer2)	E-glass/epoxy	110
Upper skin (layer3)	E-glass/epoxy	131
Upper skin (layer4)	E-glass/epoxy	133

Table 22: MoS values for lower skin layers in PLA case

Group	Material	Margin of Safety (%)
Lower skin (layer1)	E-glass/epoxy	18
Lower skin (layer2)	E-glass/epoxy	23
Lower skin (layer3)	E-glass/epoxy	35
Lower skin (layer4)	E-glass/epoxy	41

Figure 39 shows the von Mises stress contours for the skin for the PLA case. The maximum stresses occur in the nodes at which the RBE2 elements are connected to the wing. The stresses are also high at the corners at which spar flanges extending from the wing and root rib intersects. The geometrical discontinuity is the reason for high stresses at these locations.

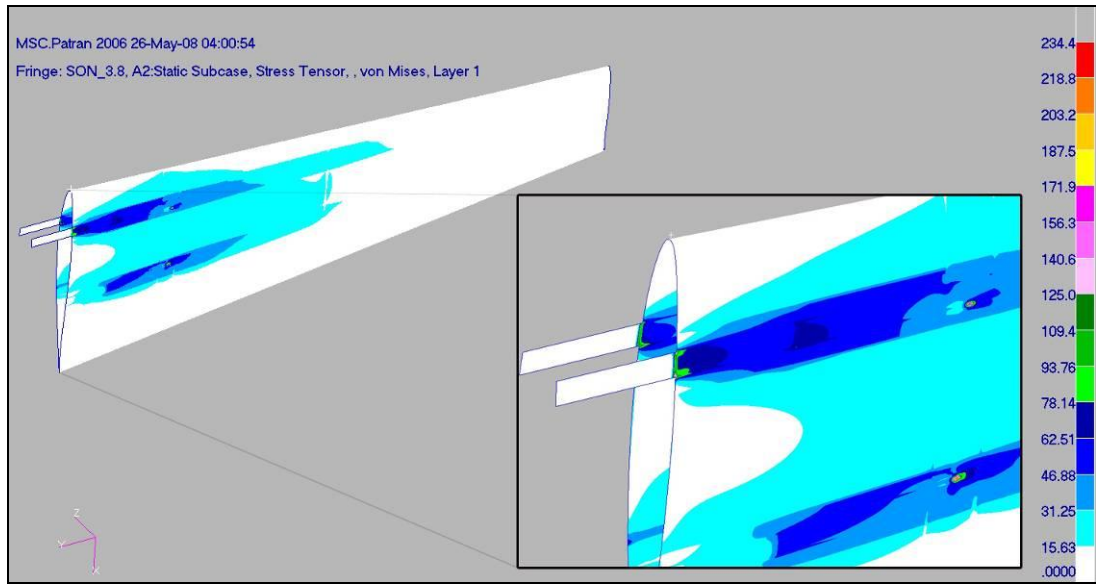


Figure 39: von Mises stress contours for skin in PLA case

Table 23 presents the margin of safety values for the spar webs and the ribs for the PLA case. One can see that +x face of front spar and -x face of rear spar have lower MoS values than the remaining faces by looking at Table 23. The rigid RBE2 elements, which represent the tail boom, are connected to the wing at these locations. Therefore high stress values were expected at these locations. Figure 40 shows the von Mises stress contours for ribs and spar webs in PLA case. It can be seen that the first three ribs from root section are more critical than the other outer ribs.

Table 23: MoS values for webs and ribs in PLA case

Group	Material	Margin of Safety (%)
<i>Front Spar -x face</i>		
Web (layer1)	Carbon/epoxy	205
Web (layer2)	Carbon/epoxy	247
Web (layer3)	Carbon/epoxy	241
Web (layer4)	Carbon/epoxy	239
Web (layer5)	Carbon/epoxy	236
<i>Front Spar +x face</i>		
Web (layer1)	Carbon/epoxy	25
Web (layer2)	Carbon/epoxy	28
Web (layer3)	Carbon/epoxy	32
Web (layer4)	Carbon/epoxy	36
Web (layer5)	Carbon/epoxy	39
<i>Rear Spar -x face</i>		
Web (layer1)	Carbon/epoxy	10
Web (layer2)	Carbon/epoxy	11
Web (layer3)	Carbon/epoxy	13
Web (layer4)	Carbon/epoxy	14
Web (layer5)	Carbon/epoxy	15
<i>Rear Spar +x face</i>		
Web (layer1)	Carbon/epoxy	360
Web (layer2)	Carbon/epoxy	359
Web (layer3)	Carbon/epoxy	357
Web (layer4)	Carbon/epoxy	355
Web (layer5)	Carbon/epoxy	351
<i>Ribs</i>		
Ribs (layer1)	Carbon/epoxy	182
Ribs (layer2)	Carbon/epoxy	233

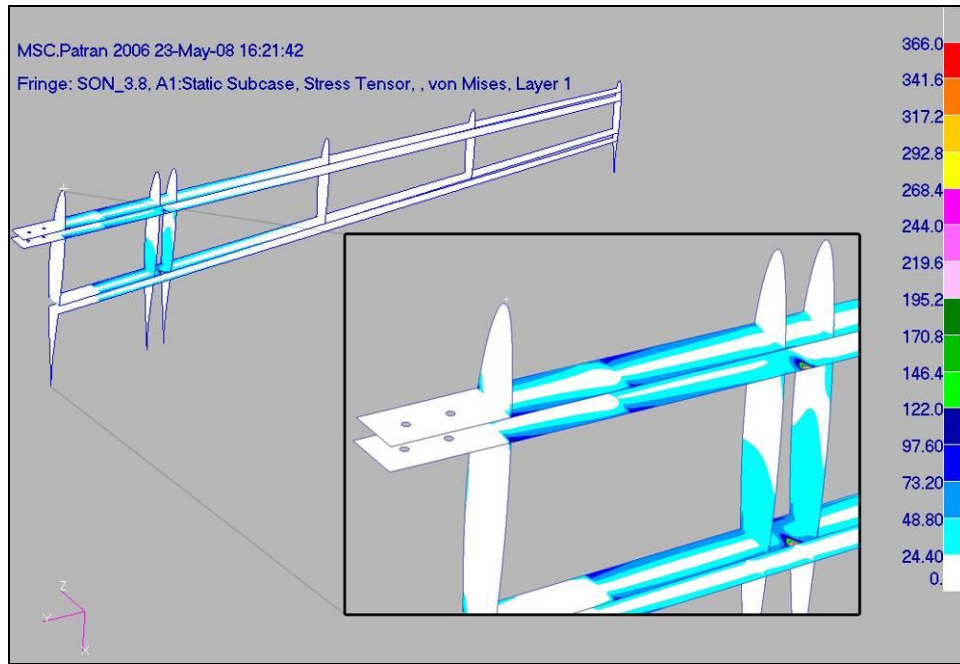


Figure 40: von Mises stress contours for ribs and webs in PLA case

Figure 41 shows the deformation contour for the PLA case. It can be seen that the tip displacement is 54 mm and this figure is deemed to be a small value owing to the high stiffness of the wing.

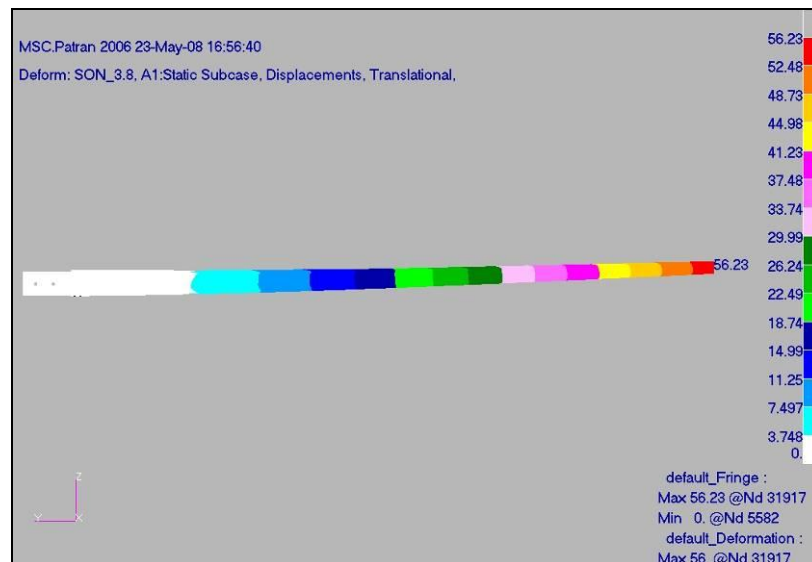


Figure 41: Deformation contour of the whole wing in PLA case

5.5.2. Results of Static Analysis at Positive High Angle of Attack Case

Table 24 gives the margin of safety for the front spar. The most critical stress is seen to occur on the hornbeam at the corner where the spar enters into the box as in the PLA case.

Table 24: MoS value for front spar in PHA case

Group	Material	Margin of Safety (%)
Front Spar	Hornbeam	43

Figure 42 shows the von Mises stress contours for the front spar core material in PHA case. It can be seen that maximum stress is below the ultimate tensile strength of the hornbeam. Similar arguments for the peak stress locations are also valid for the PHA case as the PLA case.

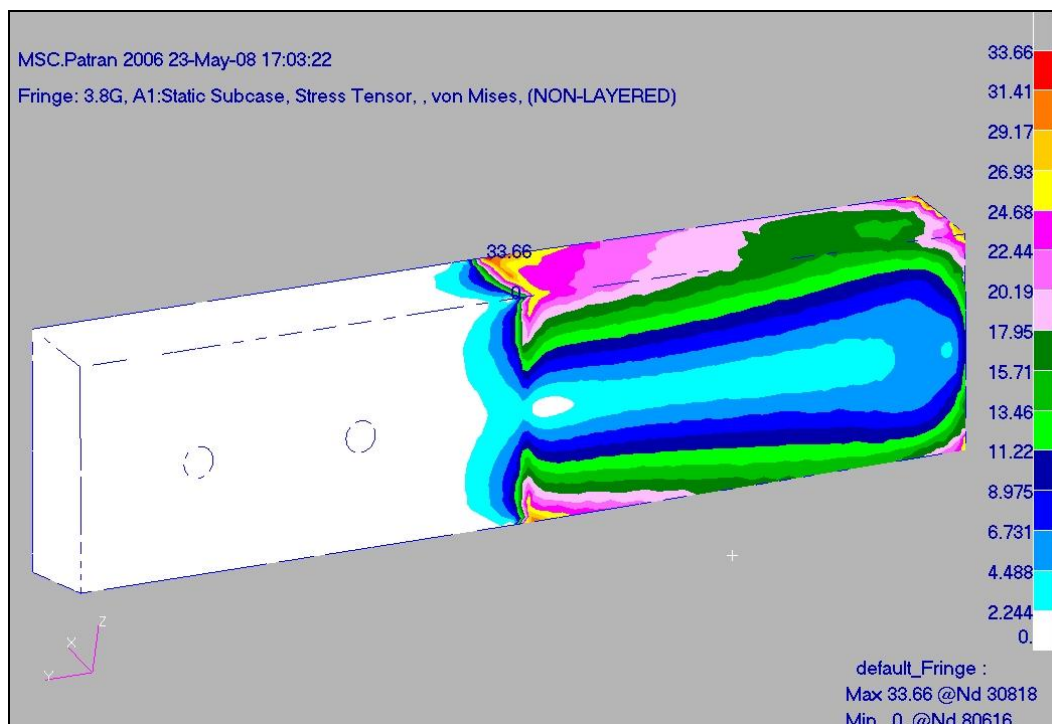


Figure 42: von Mises stress contour for front spar in PHA case

Table 25 gives the margin of safety for the rear spar. The most critical stress is seen to occur on the end aluminum which is used as the core material at the root part of the rear spar as shown in Figure 33. The critical stress point was at the corner where the aluminum ends and this is shown in the von Mises stress plot given in Figure 43. The arguments made for the location of the maximum stress point for the PLA case is also valid for the PHA case.

Table 25: MoS value for rear spar in PHA case

Group	Material	Margin of Safety (%)
Rear Spar	Aluminum 7075-T6	252

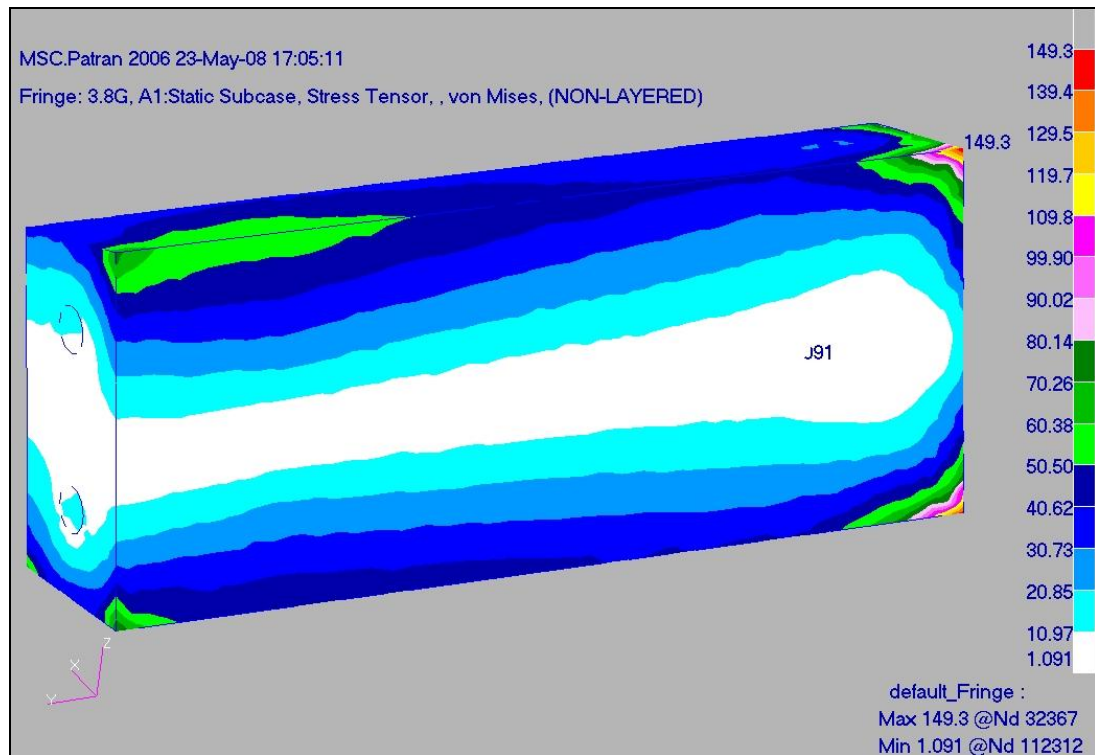


Figure 43: von Mises stress contour for rear spar in PHA case

Table 26 presents the margin of safety values for the skin layers for the PHA case.

Table 26: MoS values for skin layers in PHA case

Group	Material	Margin of Safety (%)
Upper skin (layer1)	E-glass/epoxy	159
Upper skin (layer2)	E-glass/epoxy	164
Upper skin (layer3)	E-glass/epoxy	190
Upper skin (layer4)	E-glass/epoxy	194
Lower skin (layer1)	E-glass/epoxy	172
Lower skin (layer2)	E-glass/epoxy	170
Lower skin (layer3)	E-glass/epoxy	196
Lower skin (layer4)	E-glass/epoxy	193

Figure 43 shows the von Mises stress contours for the skin for the PHA case. For the PHA case it is seen that the peak stresses occur in the regions where the end aluminum block for the rear spar and hornbeam for the front spar ends inside the wing. These peak stress locations are reasonable because of the geometric discontinuity. It should also be noted that as Table 26 shows the lowest margins of safety occur at the first layers which are the inner layers of the wing skin.

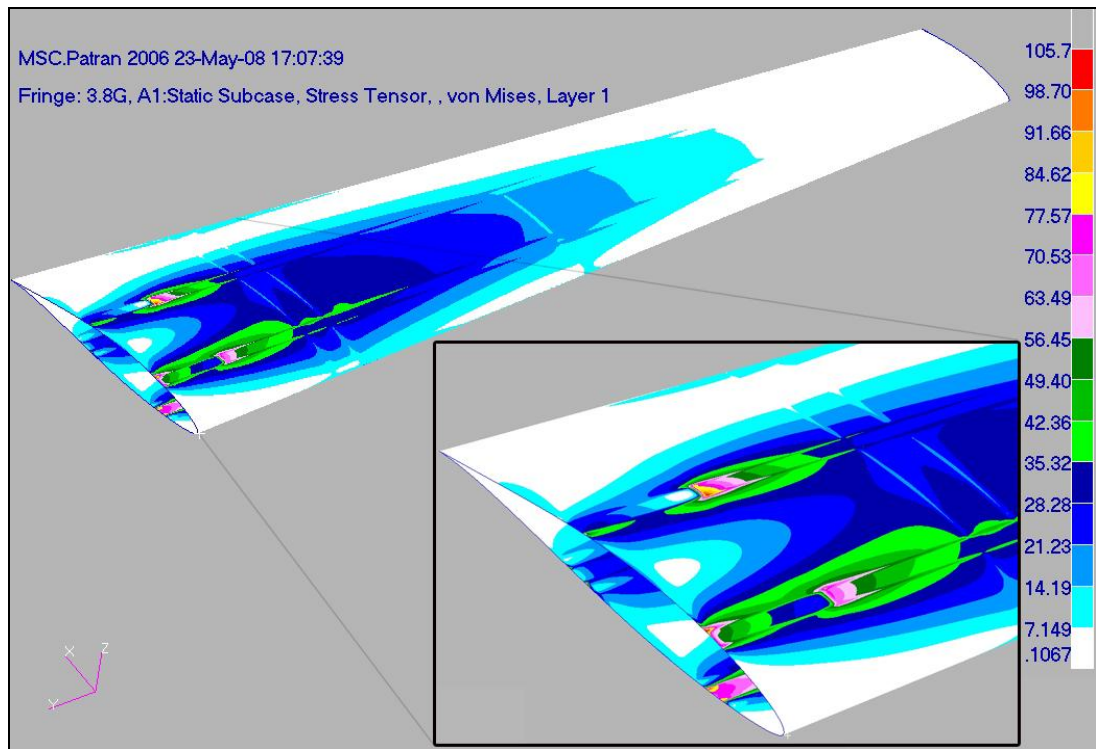


Figure 44: von Mises stress contours for skin in PHA case

Table 27 presents the margin of safety values for the spar webs and the ribs for the PHA case. One can see that the MoS values for PHA are not as low as in PLA case by looking Table 27. In PLA case, the high stresses occur at tail boom connection areas whereas in PHA case high stresses occur around areas where the aluminum and hornbeam blocks start. Tail load is a function of the square of the velocity therefore it is consistent that tail load for the low velocity PHA case is less than the one in PLA case. Thus, lower margins of safety for the PLA case is deemed to be due to higher tail load which would be generated at high velocity.

Table 27: MoS values for webs and ribs in PHA case

Group	Material	Margin of Safety (%)
<i>Front Spar -x face</i>		
Web (layer1)	Carbon/epoxy	284
Web (layer2)	Carbon/epoxy	284
Web (layer3)	Carbon/epoxy	287
Web (layer4)	Carbon/epoxy	291
Web (layer5)	Carbon/epoxy	295
<i>Front Spar +x face</i>		
Web (layer1)	Carbon/epoxy	253
Web (layer2)	Carbon/epoxy	253
Web (layer3)	Carbon/epoxy	250
Web (layer4)	Carbon/epoxy	253
Web (layer5)	Carbon/epoxy	253
<i>Rear Spar -x face</i>		
Web (layer1)	Carbon/epoxy	212
Web (layer2)	Carbon/epoxy	207
Web (layer3)	Carbon/epoxy	205
Web (layer4)	Carbon/epoxy	201
Web (layer5)	Carbon/epoxy	196
<i>Rear Spar +x face</i>		
Web (layer1)	Carbon/epoxy	277
Web (layer2)	Carbon/epoxy	287
Web (layer3)	Carbon/epoxy	295
Web (layer4)	Carbon/epoxy	295
Web (layer5)	Carbon/epoxy	295
<i>Ribs</i>		
Ribs (layer1)	Carbon/epoxy	215
Ribs (layer2)	Carbon/epoxy	287

Figure 45 shows the Von Mises plot for the rib and spar webs. Figure 45 clearly shows that the peak stresses occur at the location where the front and rear spar end blocks ends in the wing. The corners give the peak stresses as expected.

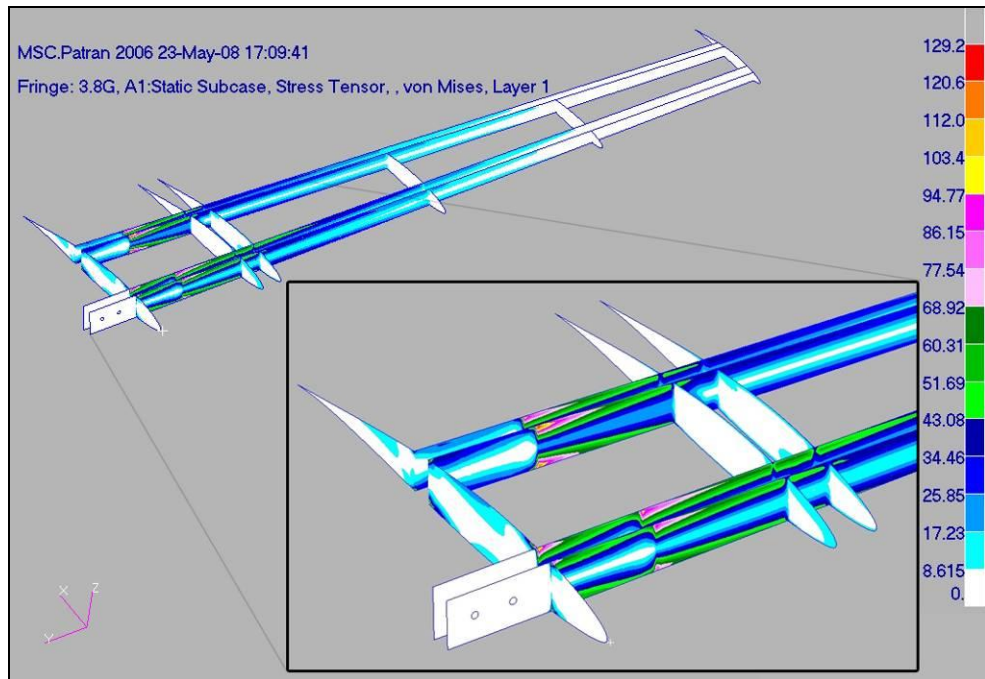


Figure 45: von Mises stress contours for ribs and webs in PHA case

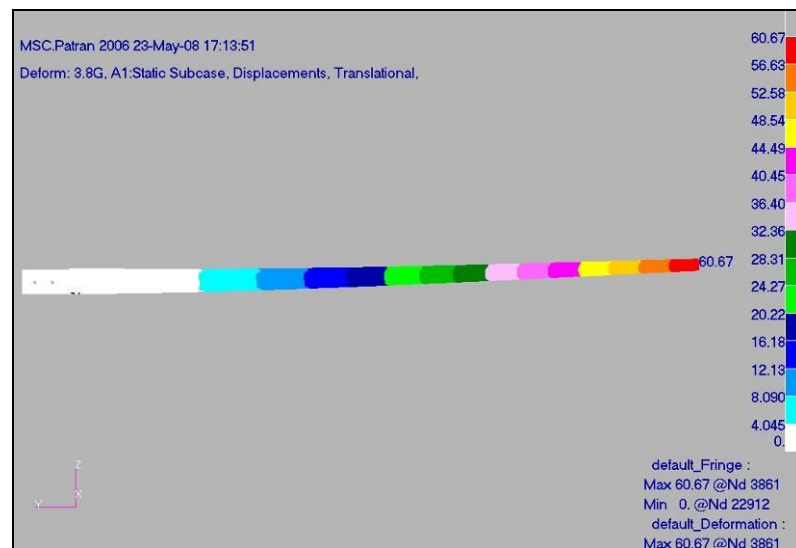


Figure 46: Deformation contour of the whole wing in PHA case

Figure 46 shows the deformation contour for the PLA case. It can be seen that the tip displacement is approximately 58 mm and this figure is deemed to be a small value owing to the high stiffness of the wing.

To sum up, for both PLA and PHA cases, maximum stress values do not exceed the strength of the materials in corresponding areas. However, the elements at which the maximum stresses occur are different for each case. Thus, the importance of load case study can be understood from these results. The comparison of PLA and PHA case is tabulated in Table 28.

Table 28: Comparison of peak stress and displacements for PLA and PHA cases

CASE	Maximum Stress (MPa)	Material	Zone	Maximum Displacement (mm)
PLA	366	Carbon/epoxy	Tail boom-wing connection	56.2
PHA	149	Aluminum	At the corner where the aluminum ends	60.7

5.6. Dynamic Analysis of METU TUAV's Wing

In order to determine the dynamic characteristics of METU TUAV's wing, modal and frequency response analyses were performed. The results from a normal mode analysis can be used to guide further possible vibration experiments that may be conducted on the METU TUAV's wing. When planning the vibration testing, best location for accelerometers can be determined and placing them to nodal points can be avoided by the help of results from modal analysis. In addition, experimental vibration results can be compared to the finite element results for mutual verification of the results. The natural frequencies are also good indicators of the stiffness of the wing since natural frequencies are directly proportional with stiffness.

In modal analysis, MSC. Nastran's NAS103 solver is used and natural frequencies are determined along with the corresponding mode shapes. The results are tabulated in Table 29 which shows the first three modes and natural frequencies. It can be seen that the fundamental frequency 16.8 Hz is a high value for the fundamental frequency of typical wing structures. The low tip deflection for the PLA and PHA load cases and the high fundamental natural frequency are indication of high stiffness of the wing.

Table 29: First three normal modes and their frequency

Order	Frequency (Hz)	Type
1	16.8	First bending
2	71.7	Torsion + Bending
3	84.5	Torsion

The mode shapes of the wing, corresponding to first three natural frequencies, are shown in Figure 47, Figure 48 and Figure 49, respectively.

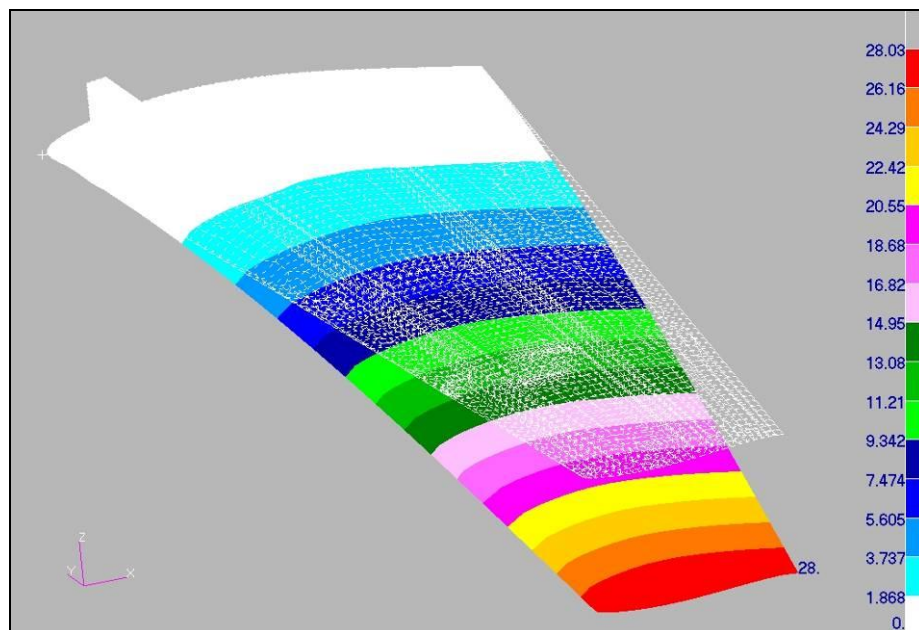


Figure 47: Mode shape for the first modal frequency (16.8Hz)

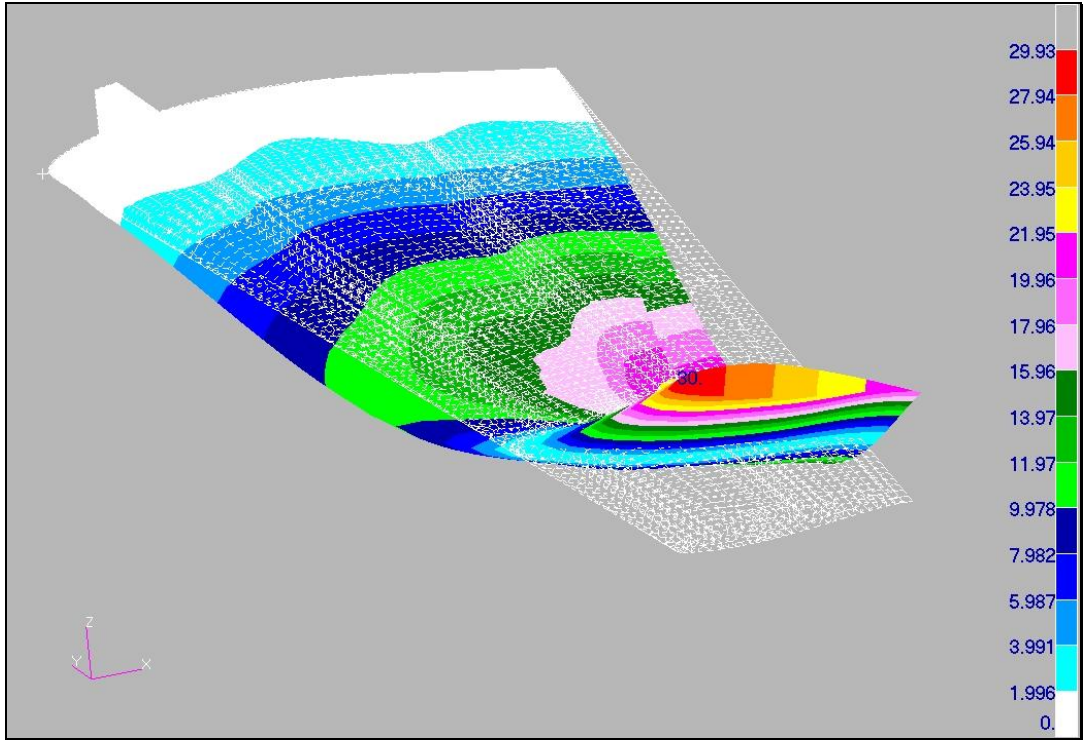


Figure 48: Mode shape for the second modal frequency (71.7 Hz)

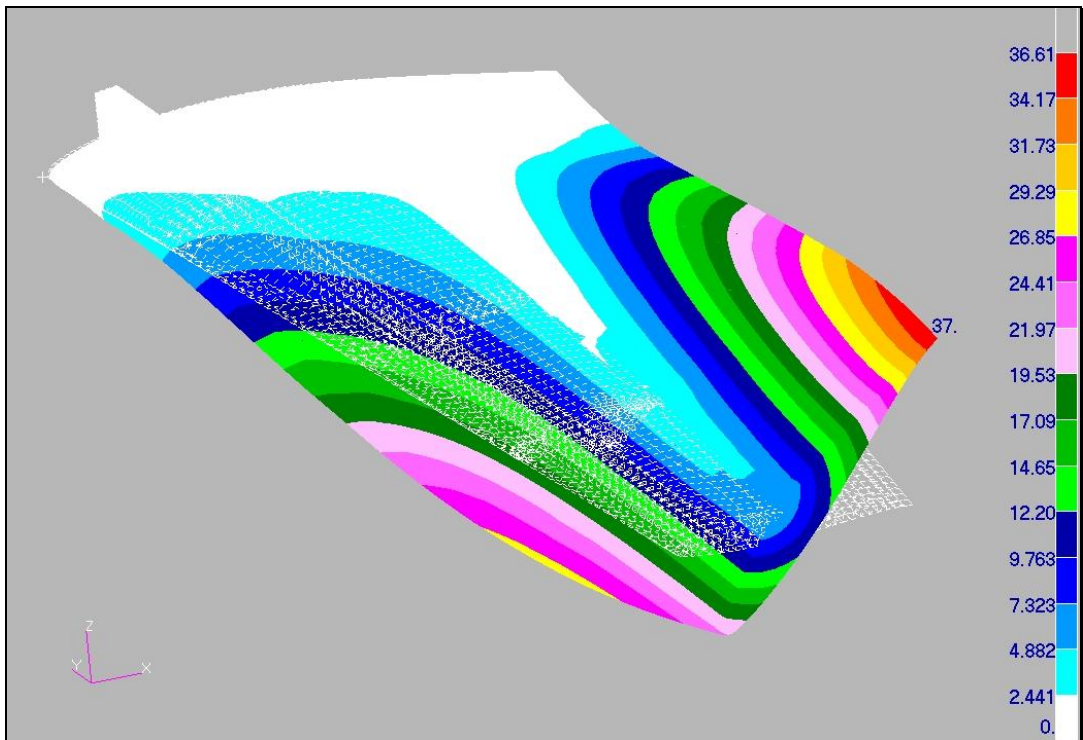


Figure 49: Mode shape for the third modal frequency (84.5 Hz)

In order to further substantiate the results of modal analysis, frequency response analysis has also been performed. In the frequency response analysis, MSC. Nastran has two different numerical methods. The direct method (NAS 108) solves the coupled equations of motion by direct integration in response to a harmonic force in terms of forcing frequency. The modal method (NAS 111) utilizes the mode shapes of the structure to reduce and uncouple the equations of motion and the solution for a particular harmonic forcing frequency is obtained through the summation of the individual modal responses [29]. The modal method is more suitable for large models since it is a solution of smaller system of uncoupled equations. Therefore MSC. Nastran's NAS 111 solver is used for the frequency response analysis of METU TUAV's wing.

In the frequency response analysis, a unit force with a variable frequency is applied from the tip of the wing and responses at two locations are monitored as shown in Figure 50. The analysis is done in a frequency range of 1Hz-250Hz. In other words frequency is swept from a low value to a sufficiently high value, and essentially the frequency response analysis is performed just like a vibration test.

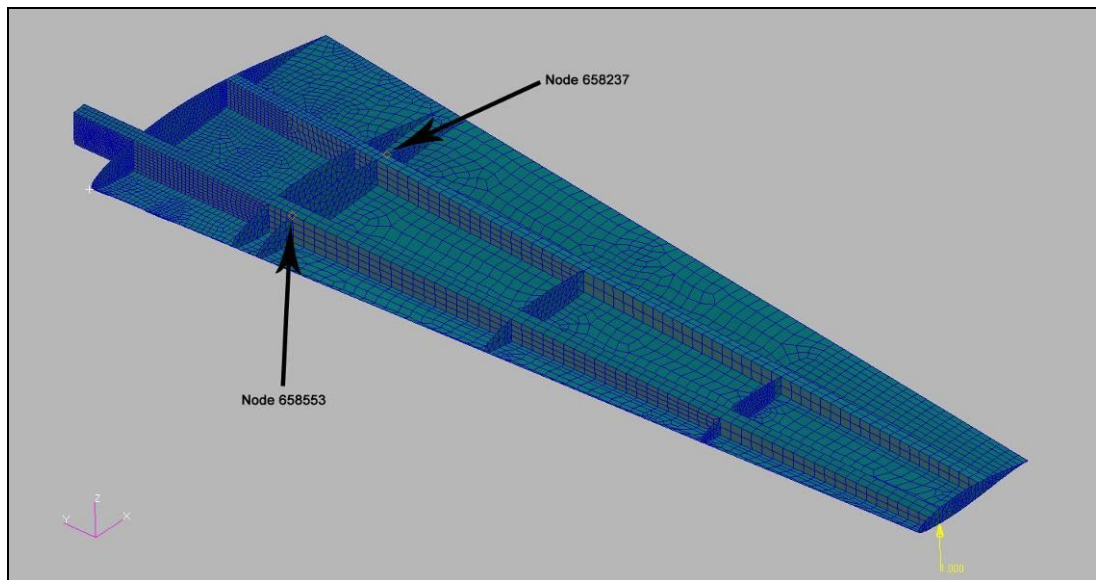


Figure 50: The locations of applied force and monitored nodes

The acceleration responses in $-z$ direction at these locations are shown graphically in Figure 51. As expected, the corresponding frequencies at the peak of response curves coincide with the natural frequencies found in modal analysis. It is deemed that the results of the frequency response analysis can be used in evaluating the results of vibration test which may be conducted on the wing. Especially, in updating the finite element model the results of the frequency response analysis can be used together with the results of experimental vibration analysis.

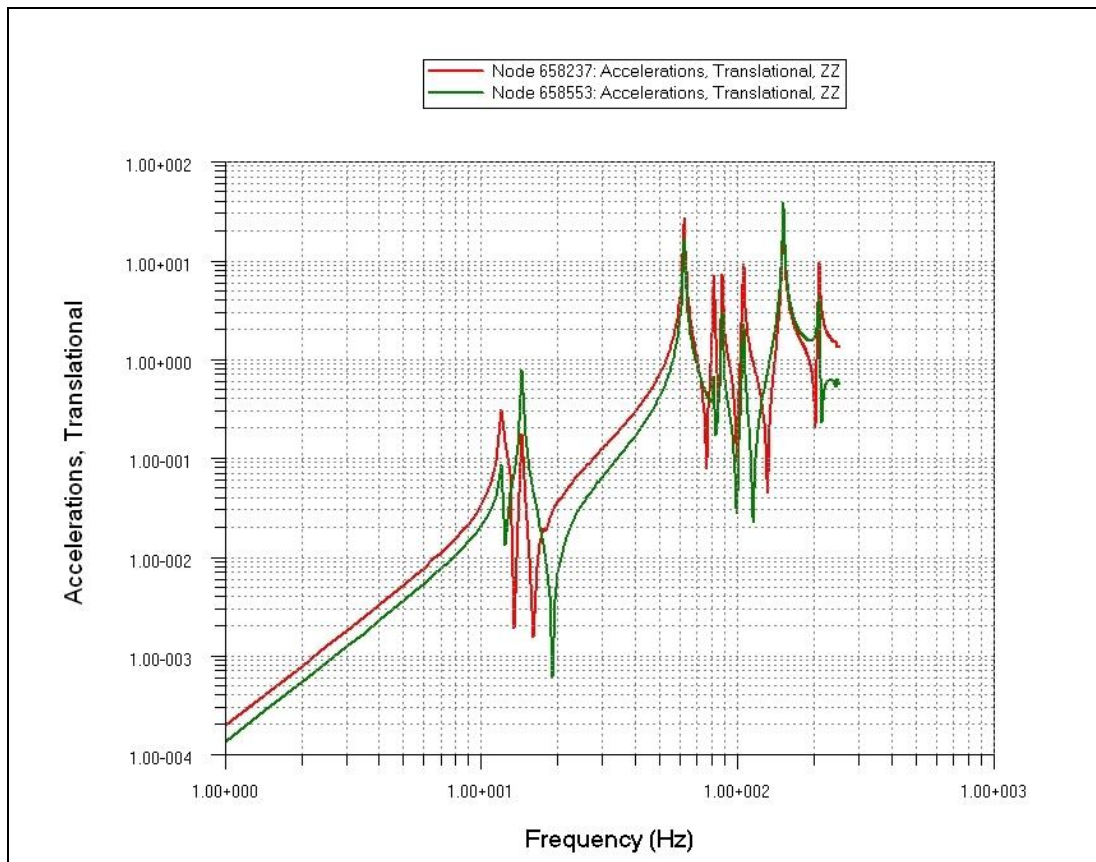


Figure 51: Acceleration response of Node 658237 and Node 658553

5.7. Simplified Torsional Divergence Speed Calculation

Torsional divergence is a static aeroelastic instability which results in catastrophic failure of a sub-structure of an aircraft such as wing or fin. During flight incremental

changes in the aerodynamic pitching moment cause incremental changes in the twist which induces an incremental angle of attack which in turn causes incremental change in the pitching moment. Below a certain speed these incremental changes in the pitching moment and the incremental changes in the angle of attack decrease until a steady angle of attack value is reached. At low speeds the aerodynamic moment is resisted by the elastic restoring moment about the elastic axis of the wing. However, the aerodynamic moment is a function of the square of the flight velocity whereas the elastic restoring moment is a function of torsional stiffness of the wing, thus it is independent of the velocity. Therefore, as the flight velocity increases, a velocity may be reached and at this velocity the elastic restoring moment can barely resist the aerodynamic moment at the disturbed state. Thus, at this critical speed wing can disintegrate because it cannot resist the aerodynamic moment. Beyond the critical speed the incremental changes in the aerodynamic moment and twist do not decrease but they continuously increase resulting in catastrophic failure. In this thesis, torsional divergence speed is calculated based on the slender beam model with the following main assumptions [30]:

- Slender straight wing
- Elastic axis which is nearly perpendicular to the plane of symmetry of the airplane
- Rigid chordwise segments of the wing; no camber bending

With these basic assumptions the lowest torsional divergence speed for a rectangular wing with straight elastic axis can be calculated by Equation (108) [30].

$$U_D = \frac{\pi}{2l} \cdot \sqrt{\frac{2GJ}{\rho c e C_{L_{\alpha}}}} \quad (108)$$

Here:

- l is the semi-span of the wing ($2m$)
- GJ is the torsional stiffness of the wing at 75% semi-span
- c is the mean aerodynamic chord ($0.54m$)

- e is the distance between aerodynamic center and the elastic axis of the wing
- $C_{L_{\alpha}}$ is the lift curve slope of the wing ($5.245rad^{-1}$)
- ρ is the air density (taken at sea level $1.225kg / m^3$)

Equation (108) gives the torsional speed for a wing with uniform chord and torsional stiffness. Early works on aeroelasticity was based on two dimensional representations of true lifting surfaces. Theodersen used a model of this kind in analyzing the flutter problem, designating it the ‘typical section’ and choosing its properties to match a cross section 70-75 % of the distance from the root to tip of the actual wing [31].

Although Equation (108) gives the torsional divergence speed for a rectangular wing, in this thesis the same formula is used to get an idea of the range of the torsional divergence speed for the tapered unswept wing. For this purpose, a typical section is taken at a distance close to 75% of the semi-span measured from the root of the wing and the properties given in Equation (108) are calculated at this section except the chord length c . In Equation (108) mean aerodynamic chord, which is consistent with the derivation of Equation (108), is used.

Mean aerodynamic center at 75% semi-span of METU TUAV’s wing is found using document ESDU TD MEMO 6309 from ESDU database which is available at the Department of Aerospace Engineering of METU.

The structural terms, torsional stiffness GJ and the location of the elastic axis of the wing can be found using the existing finite element model of the wing.

In order to calculate the GJ at 75% span location, Equation (109), which relates the sectional torque to rate of twist, is used.

$$T = GJ \cdot \frac{d\phi}{dy} \quad (109)$$

One can calculate GJ value at 0.75 semi-span, by applying a known moment, T , at 0.75 semi-span and calculate the rate of twist $\frac{d\phi}{dy}$ value at this position. In order to, calculate the GJ value, in the finite element model, a 1000 Nmm is applied to a node which is at the geometric center of the rib which is located very close to 0.75 span position. The rib location is shown in Figure 52 as station B . After a linear static analysis in MSC. Patran, the deformations of all the nodes at the 75% semi span section and adjacent sections towards the tip and the root of the can be determined. Typical sections (E, A, C, D) are shown in Figure 52.

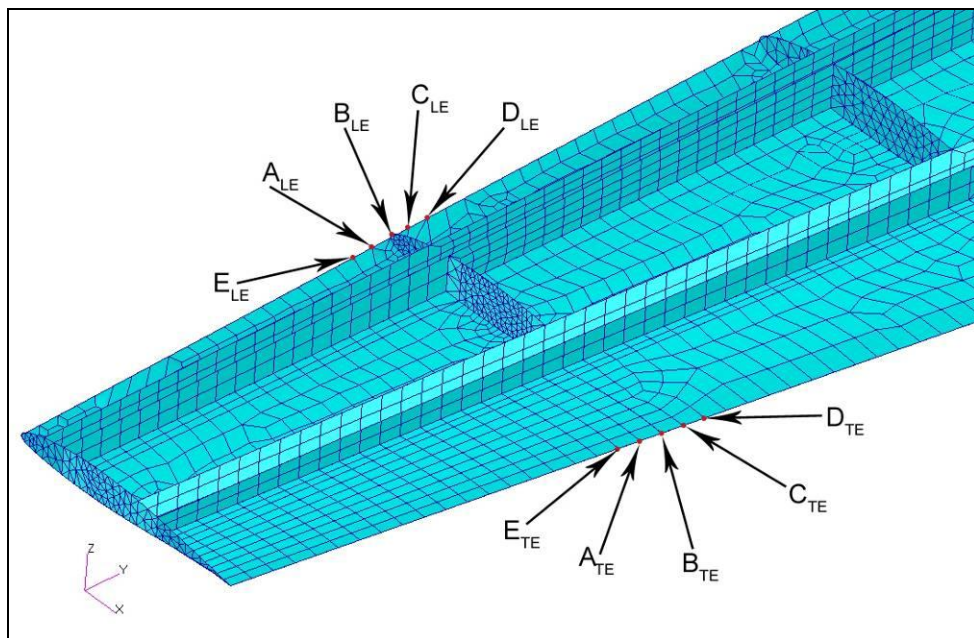


Figure 52: Locations of 75% semi span section and adjacent sections

At a particular section, by using leading edge and trailing edge translations, rotations (ϕ) at neighbor stations can be determined. The rate of change of the angle of twist ($\frac{d\phi}{dy}$) at 0.75 semi-span position can then be found using a high order central difference formula used for derivative calculations. The central difference formula is given by Equation (110).

$$f' = \frac{-f_2 + 8f_1 - 8f_{-1} + f_{-2}}{12h} \quad (110)$$

Applying Equation (110) to the current case yields Equation (111)

$$\left. \frac{d\phi}{dy} \right|_{0.75span} = \frac{-\phi_E + 8\phi_A - 8\phi_C + \phi_D}{12\Delta y} \quad (111)$$

Inserting $\frac{d\phi}{dy}$ and T values into the Equation (109) gives GJ value at 0.75 semi-span location. It is found that:

$$GJ = 1.22 \cdot 10^4 \text{ Nm}^2$$

The second elastic property, which is required for the calculation of the torsional divergence speed, is the position of the elastic axis of the wing at 0.75 semi-span location. The translations of the nearest node to the elastic axis would be almost zero and this node can be identified by looking to the deformation fringe plot found from deformation contour plots obtained in post-processing module in MSC. Patran. The deformation contour plot is shown in Figure 53.

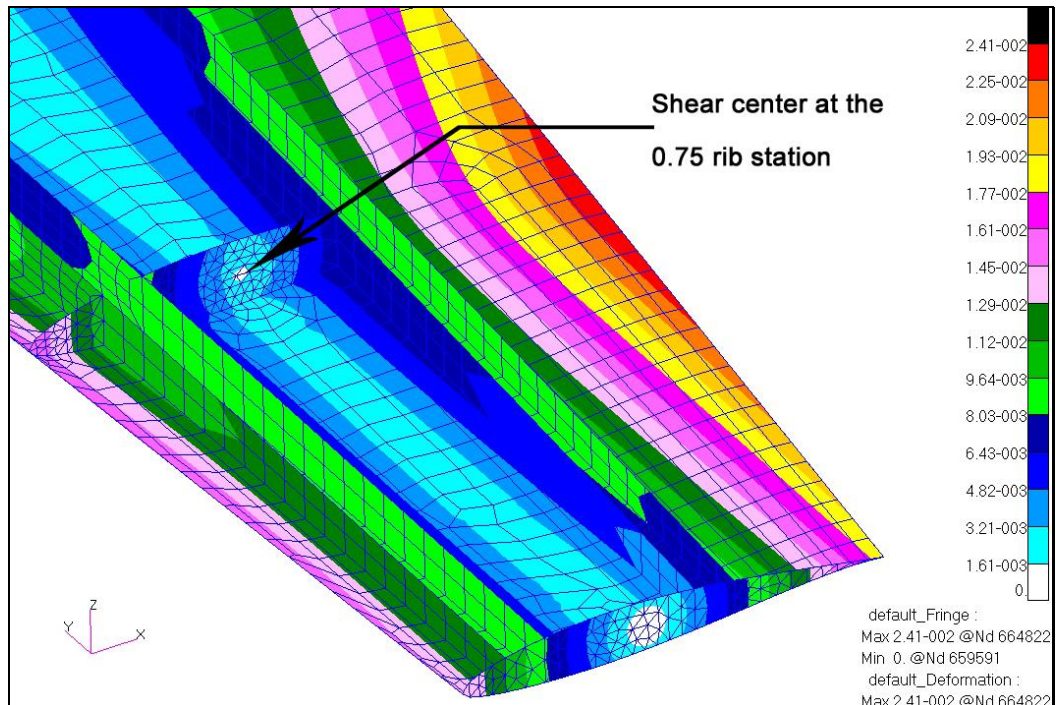


Figure 53: The location of shear center at 0.75 semi-span

As one can see, the little white point in the rib which is the section of interest, indicates that in response to the torque applied at that rib location, there exist almost no deformation. Therefore, the center location of this zero deformation region is taken as the shear center location at the 75 % semi span location. The distance between aerodynamic center and shear center at the 75 % semi span location is then calculated as 62.49mm.

$$e = 62.49mm$$

After substituting all the values in Equation (108), with the air density being the sea level density and lift curve slope calculated in conceptual design, the torsional divergence speed is calculated as 263 m/s.

The divergence speed calculated from Equation (108) is a very approximate speed because Equation (108) is valid for a rectangular wing. In this study, by taking a section at %75 wing span, it is tried to get a rough estimate for the magnitude of the torsional divergence speed. The estimated speed of 263 m/s is seen to be very high compared to the dive speed of the unmanned air vehicle. It can be assumed that from a practical engineering point of view, the true torsional divergence speed will also be very high compared to the dive speed of the air vehicle. The true torsional divergence speed can be obtained by a more detailed analysis. In the detailed analysis, one can determine the GJ and shear center location distribution along the semi span of the wing, and a similar slender beam model can be used to determine the torsional divergence speed based on the full half wing model.

It should also be noted that considering that the design dive speed is 100 m/s, the approximate estimate for the torsional divergence speed is a very high speed and this is an indication of the high torsional stiffness of the wing. Finally, the present work performed for the calculation of the torsional divergence speed of the air vehicle shows how a finite element model can be used to determine the sectional properties of the wing such as GJ distribution and shear center location which are very critical parameters in aeroelastic stability analysis.

CHAPTER 6

INTEGRAL MANUFACTURING OF A TORQUE BOX

6.1. Introduction

Composite structures are being increasingly used in the primary structures of aircraft. Because of their poor out-of-plane load transfer capacity, thin walled composite structures are stiffened by ribs or stringers [32]. In general, in building semi-monocoque composite structures stiffeners, ribs and skin structures are integrated to each other by adhesive bonding. Reliability of adhesive bonding is not predictable although very strong anaerobic structural adhesives are available in the market and they are frequently used in composite manufacturing. To strengthen the adhesively bonded regions extra composite layers are applied in fusion areas or metal doublers are applied by means of riveting. In manufacturing of METU TUAV and METU mini UAV “*Güventürk*” adhesive joining technique is used with some differences. As explained in Chapter 2.3.2, when manufacturing METU TUAV’s wing, spars and lower skin are manufactured integrally. But as shown in Figure 14b, the upper skin is adhesively joined to the upper surfaces of spars and ribs. This adhesive bonding technique introduces extra weight to structure. In METU TUAV, this is approximately 15% of the total weight of the wing. If a fully integrated and continuous upper skin-spar-rib-lower skin structure was manufactured, this extra weight could have been prevented. The composite skin-stiffener integrity problem is generally handled by making upper and lower parts integrally by themselves and then joining them with a different technique. The costs and complexity of these techniques stand in a wide range. In NASA’s “AST Composite Wing Program” [33], the integrity between skin and stiffeners are achieved by stitching process which is basically involves sewing high tensile thread through stacked ply layers to produce a preform with a 3D structure [12] as shown in Figure 54. Then the preform is resin infused by the help of vacuum bagging in an autoclave. When the investment costs

of autoclave and stitching machine are considered it can be seen that this procedure is not suitable for low cost small aircrafts or UAVs.

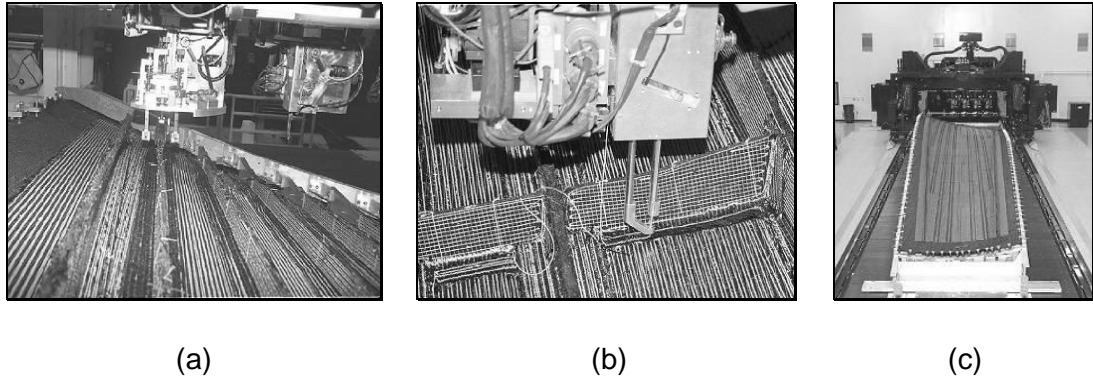


Figure 54: Stitching of (a) stringer to skin, (b) rib to skin, (c) skin with integral spar caps [33]

Another example of integrated manufacturing of skin-stiffener assembly is demonstrated by Lockheed Martin Space Systems (LMSS), to minimize the fabrication cost of one of the largest and most complex components of Trident II D5 missile system by using vacuum-assisted resin transfer molding (VARTM). Labor, time and overall cost were reduced with cost savings as high as 75% and 61-part assembly was manufactured at once therefore 376 fasteners were eliminated [34]. VARTM is also used to manufacture a fully integral skin-stringer assembly by Mahfuz et al [32]. The end product of their work is shown in Figure 55.

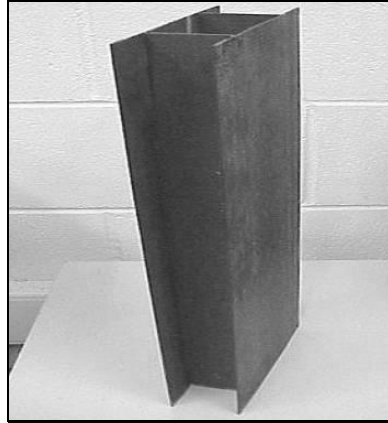


Figure 55: Integral composite skin-stringer assembly [32]

In this thesis similar manufacturing steps of Mahfuz et al [32] are followed to manufacture a composite box structure with some differences. At the end a fully skin-stringer integrated composite box structure which is manufactured using VARTM, is demonstrated.

6.2. Vacuum-Assisted Resin Transfer Molding (VARTM)

The VARTM process is a composite fabrication process by which a dry fiber preform is vacuum-bagged against a single-sided tool and is infused with resin that is drawn in a controlled manner into the evacuated preform [26]. The schematic of the VARTM process is shown in Figure 56 and photographs of a VARTM setup for manufacturing of a composite plate are shown in Figure 57 and in Figure 58. The resin is introduced to the system through ports or flow lines. The distribution medium covering the workpiece makes the resin easy to infiltrate to the preform and eliminates the dry spots. The peel ply on the preform is for easy removal of the distribution medium and vacuum bag from the workpiece. Spiral tubes are tubes that are cut in a spiral shape. Spiral tubes are generally placed all around laminate as shown in Figure 57, and they suck the air under the vacuum bag until the resin flows and wet all the laminate which is to be manufactured. Through the fittings at the end of these tubes, they are connected to the resin catch tank. The shape of the tubes allows the excess resin in the system to be sucked and transferred to the resin catch tank. Resin catch tank is connected to the vacuum pump which keeps it under vacuum all the time.

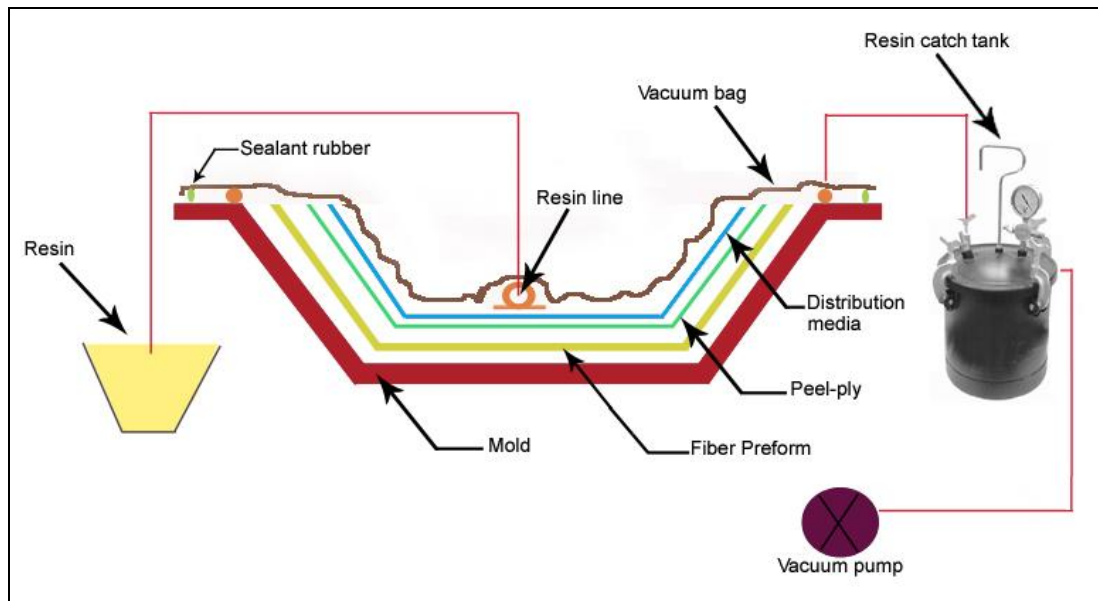


Figure 56: Schematic of the VARTM process



Figure 57: VARTM setup before covering with vacuum bag

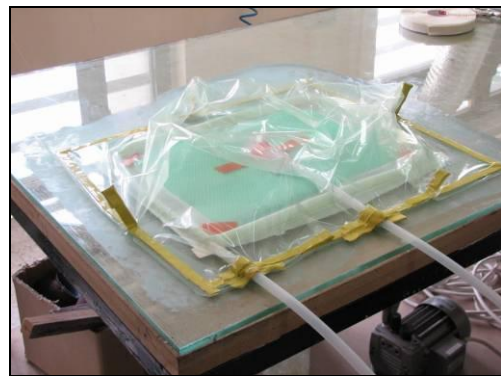


Figure 58: VARTM setup with vacuum bag and resin lines

The most advantageous property of VARTM is its cost effectiveness over the processes like resin transfer molding (RTM) and resin film infusion (RFI). There is no need for two sided metal molds as in RTM, vacuum bag becomes the top half of the mold. Therefore molding costs reduce significantly in VARTM but it should be noted that the dimensional accuracy of the end product from VARTM cannot be as accurate as the one from RTM since the vacuum bag is not rigid but it is flexible.

When compared to RFI, there is no need to an autoclave operation in VARTM which reduces the initial investment costs significantly. But again this advantage comes with a drawback. The pressure difference which is the driving force of resin infusion is obtained by vacuum bagging without an additional positive pressure as it is the case in autoclave operation. This drawback also reduces the fiber volume fraction when compared with RFI.

In addition, VARTM has many advantages over classical hand lay-up technique which is used in manufacturing of METU UAV's composite parts with vacuum bagging. In hand lay-up technique the amount of resin which is used to wet the fabric is not predictable and varies from person to person who applies the resin with brushes or rollers. In an ideal VARTM process, the excess resin brought into the system is collected by resin flow lines around the workpiece. Not like classical hand lay-up technique, the setup time of VARTM process is not limited by the curing time of resin since the resin is given to the system at the last step. Last but not the least; the VARTM process is much cleaner than hand lay-up, there is no interaction between resin and human, no splashes etc.

6.3. Manufacturing of a Cured Composite Box

The first step of the cured manufacturing is the preparation of the styrofoam molds. Hard styrofoam should be chosen as the mold material so that it will not collapse under vacuum. Also they can be hardened with epoxy to make their surface hard and smoother. This also prevents resin to penetrate into mold during infusion process. The foam molds hardened with epoxy are shown in Figure 59a.

The molds are then covered with distribution media. Under vacuum the resin will travel in the system through the easiest path. Distribution media forms this path around the molds. Mesh like plastic distribution media are cut and glued to the surface of the molds with a spray adhesive. This makes working with the molds easier. The molds covered with distribution media is shown in Figure 59b.

Over the distribution mesh peel ply is wrapped as the next step. Peel ply is a permeable cloth which is in contact with the preform and eases the removal of workpiece. Peel ply covered molds are shown in Figure 59c

Around the peel ply e-glass woven fabrics are rolled over tightly. During the rolling over the woven fabric “tac-strip” pieces are applied between the layers. Tac-strip is a fiberglass fabric mesh tape coated on both sides with a pressure sensitive adhesive. It stays inside the layers and become a member of the fabric stacks without hampering the structural properties. Fiberglass sticky tape holds the preform in one piece and avoids the movement of the preform around the mold. Woven fabric preforms around the molds are shown in Figure 59d.

A glass surface, which is used as the tool plate, is coated with a release agent. This surface will be the mold surface for the lower surface of the workpiece. A double sided adhesive tape is applied to the glass surface in order to hold the spiral tube through which trapped air under the vacuum bag and excess resin in the system will be sucked. A layer of distribution media is laid on the glass surface, or the tool plate, which will ease the wetting of the lower surface of the preform. The distribution media is covered with peel ply as it was done in molds. These steps are shown in Figure 59e and Figure 59f. In Figure 59e spiral tube is placed on top of a double sided tape in order not to move during the vacuuming operation. The air will be sucked from the two ends of the spiral tube through the end plastic L shaped joints.

On to the peel ply two layer of e-glass are laid and three preforms around molds are put together on top of these layers. Finally two more layers which will form the top surface of the workpiece are laid on these molds as shown in Figure 59g. Over the preform is a peel ply layer is put to ease the removal of the workpiece after the curing. As a final layer distribution mesh is laid on top of the peel ply.

It should be noted that there is always a peel ply layer between the preform and the distribution mesh.

In front of the preform a resin flow line is placed and similarly another resin flow line is placed on top of the preform. As it is shown in Figure 59h, the resin is brought into

the system through the plastic hoses and these hoses are pushed into the resin flow lines through the opening in the middle of the resin flow line which is made of some sort of rubber. Once the resin enters into the resin flow line by the help of the suction, which will be applied through the spiral tube, the edges of the resin flow line helps the resin to travel along the edge of the resin flow line so resin starts to infuse into the front edge of the preform homogenously.

Rubber sealant tape is applied around the workpiece and tubes are plugged into the flow lines and spiral tube as shown in Figure 59i and Figure 59j. Rubber sealant will be used to secure the vacuum bag and seal whatever remains inside the bag from the external environment. In Figure 59i the plastic hose inside the spiral tube is seen. The plastic hose is pushed into the spiral tube from the both ends and its periphery is sealed against the rubber sealant tape by the again using the same rubber sealant tape. In a similar fashion the plastic tubes are placed inside the resin flow lines, and sealed against the peripheral rubber sealant tape which is placed all around the workpiece and this is shown clearly in Figure 59j. The plastic hoses shown in Figure 59j will be inserted into the resin bucket to bring in resin into the system once the vacuum is applied and air inside the bag is sucked away from the spiral tube and its end hoses. However, before the application of the vacuum, the plastic tubes which will carry the resin are squeezed by the clamps as shown in Figure 59l.

As it is shown in Figure 59k the whole setup is then covered with vacuum bag and vacuum is applied to the system Figure 59m shows the system after the vacuum is applied. The applied vacuum in the bag compacts the preform and this is a perfect moment to seal check before the resin is introduced to the system. It should be again noted that as shown in Figure 59l, the end of two plastic tubes which are connected to the flow lines, are clamped at this moment so resin does not enter into the system. Therefore, any air escape can be monitored and leakage test can be conducted.

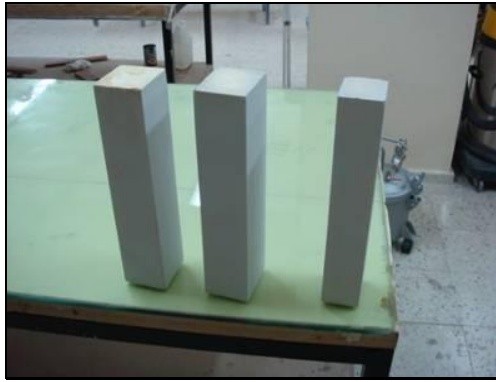
Then, the two clamped plastic tubes connected to the flow lines are immersed to the resin case and clamps are released. This way resin enters into the preform from the one end and due to the suction from the other end, the resin start to travel along the

workpiece. At this point, it should be noted that since the suction is applied from the lower surface, the resin which enters into the preform from the lower resin flow line will travel faster compared to the resin which enters into the preform from the upper resin flow line. This is because the resin distributed from the top resin flow line will be forced to travel around the three molds which are wrapped with composite fabric. Therefore, in order to match the arrival times of the resin entering into the preform from the bottom and top resin flow lines, the clamp of the top resin flow line is released earlier; the location of the resin front is observed. Then, the bottom clamp is released accordingly. The wetted preform is shown in Figure 59n and Figure 59o. Figure 59n and Figure 59o show that the whole workpiece is clamped along the sides to increase the compaction pressure during the curing process.

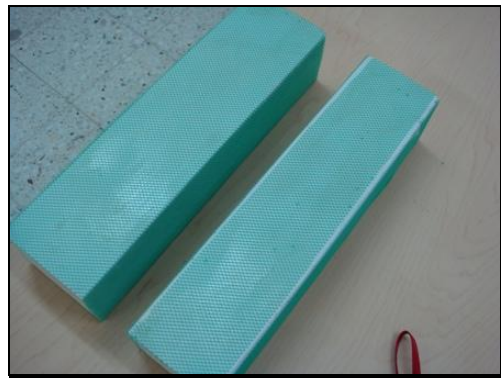
After curing process, the vacuum bag and peel ply and distribution mesh around the outer surface of the workpiece are all removed from the cured workpiece and workpiece is removed from the glass surface. At this point the foam molds are still a part of the workpiece. The workpiece before the removal of molds is shown in Figure 59p.

The last step is the removing the foam molds, peel ply and distribution media inside the composite box structure. It should be reminded that the foam molds were initially wrapped with peel ply and the distribution media for easy removal of the workpiece and for better resin distribution. The foam molds are removed using a synthetic thinner which basically melts the foam chemically. The remaining peel ply with the distribution mesh on it is then removed by the help of a chisel. The peel ply eases the removal operation very much and it does not let the distribution media to stick to the workpiece. The cleaned final product is shown in Figure 59q and Figure 59r.

As Figure 59q and Figure 59r show, with this operation it is possible to produce multi-cell box beam structures in one operation. This way the vertical webs and the horizontal upper and lower skins are integrally manufactured by the co-curing action. It is deemed that this method can also be applied to the production of sub-structures such as wings, control surfaces and horizontal and vertical tails in aerospace applications.



(a)



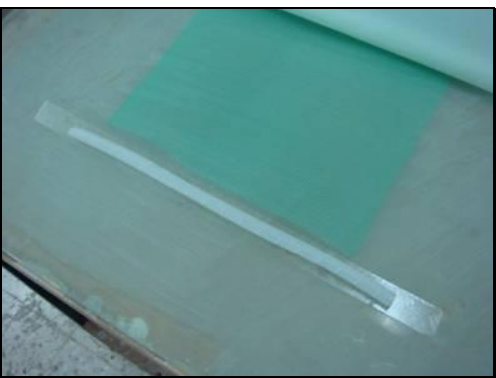
(b)



(c)



(d)



(e)

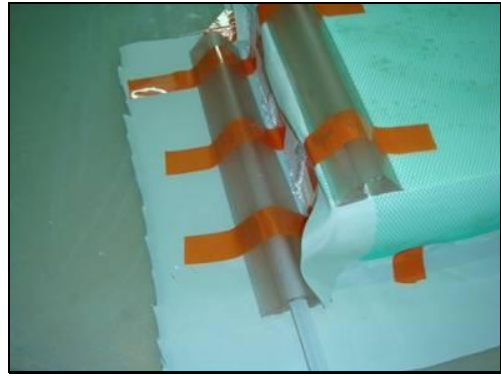


(f)

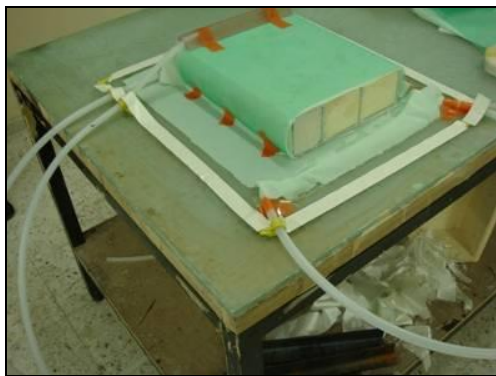
Figure 59: Manufacturing steps of a cocured composite box



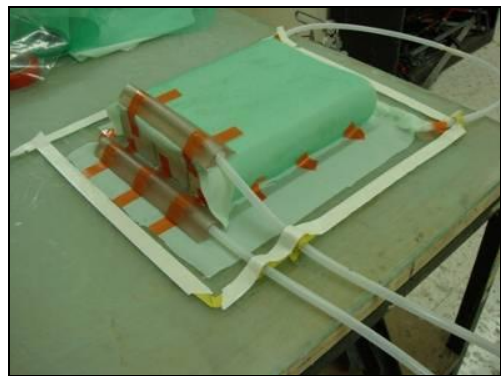
(g)



(h)



(i)



(j)



(k)



(l)

Figure 59: Manufacturing steps of a cocured composite box (continued)



(m)



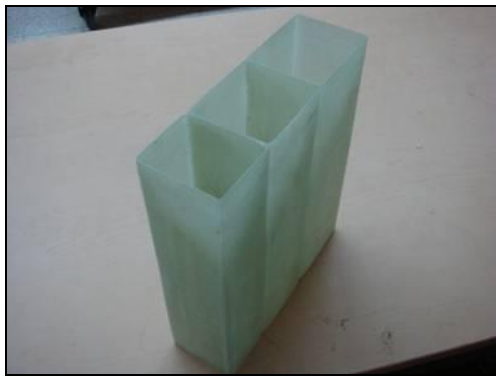
(n)



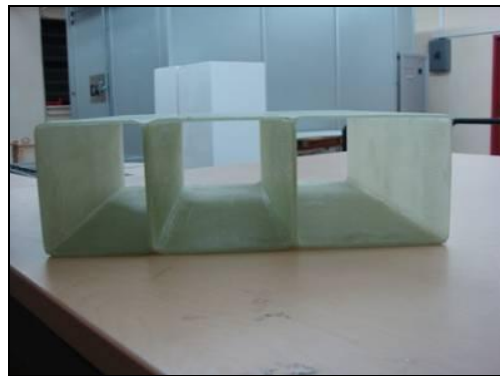
(o)



(p)



(q)



(r)

Figure 59: Manufacturing steps of a cocured composite box (continued)

CHAPTER 7

CONCLUSION

In this study structural design, analysis and composite manufacturing applications for a tactical UAV is introduced. Since wing is the most critical part of an aircraft, the study is focused on the composite wing of METU TUAV.

Firstly, the design features of METU TUAV are explained. In structural design, the structural requirements are determined from UAV Systems Airworthiness Requirements (USAR) [5] which is prepared by USAR Working Group. Structural design of the wing is introduced together with the composite manufacturing of the wing. $V-n$ diagram for the tactical UAV is established based on the limit loads specified in USAR and the design critical loads are decided to be calculated at the minimum maneuvering speed V_A and dive speed V_D . The manufacturing steps of the composite wing is introduced with sufficient detail to help the reader in following the analysis procedure which requires understanding of the internal structural layout and certain manufacturing details of the composite wing.

After determining the loading scenarios in structural design, aerodynamic loading around the wing is found via CFD analysis. The results are compared with the analytical studies which were done during conceptual design phase of METU TUAV. In order to show the effect of the computational mesh, a case study is also performed for CFD analysis and it is shown that a more fine CFD mesh is not needed for analysis. At the end of the CFD analysis, the nodal forces on the wing surface mesh are transferred to FEA mesh via interpolation.

The composite fabrics, which are used in manufacturing of METU TUAV, are in plain woven fabric form. Therefore, classical laminate theory cannot be applied directly to the composite materials that include woven fabrics. In order to find the mechanical

properties of plain woven composite materials used in the manufacturing, a detailed unit cell analysis is performed. A FORTRAN code is written to calculate the effective elastic properties of the plain weave composite fabric. The code calculates the effective elastic properties on the geometrical unit cell domain which repeats itself in the fabric. Unit cell is defined by certain shape functions which are typically used in the literature and trapezoidal numerical integration scheme was used to numerically get the effective elastic constants of the woven fabric.

After the aerodynamic load calculation and material characterization steps, the structural analysis of the METU TUAV's wing is performed. Linear static analysis of the wing is performed at two different loading conditions which are positive high angle of attack and positive low angle of attack. Results of static analyses are shown in details with contour plots and tables showing the margins of safety of different elements of the composite wing. Modal and frequency response analyses of the wing were also performed to investigate the dynamic properties of the wing. Finally, torsional divergence speed of METU TUAV is found by a simplified method based on slender beam model. Structural properties are extracted from the finite element model and aerodynamic properties such as the location of aerodynamic center are determined by using a software of ESDU database.

Based on the structural analyses results, it is concluded that the wing is safe based on static limit load analyses performed at minimum maneuvering and dive speeds. Deflection and dynamic analysis showed that the wing was relatively stiff, and this effect was also reflected in the approximate divergence speed which turned out to be quite high. Thus, before the first flight, sufficient level of confidence has been built up in the structural integrity of the wing structure.

In addition, co-cured composite manufacturing of structural members is explained in the last chapter. The merits of manufacturing multi-cell closed box beams with co-cured stiffener/spar and skin assembly is discussed. To manufacture a co-cured composite multi-cell box structure, a procedure is explained which uses vacuum assisted resin transfer molding (VARTM) technique. With the help of this procedure, a composite multi-cell box which is manufactured successfully in Aerospace Engineering Department of METU and the manufacturing steps are described in

detail with relevant pictures taken at the intermediate steps during the manufacturing.

The following studies are proposed as future work:

- CFD analysis of the wing can be improved by using a Navier-Stokes solver. Also half body and tail can be introduced to the new model; therefore fluid interactions around the whole aircraft can be investigated.
- Gust load analysis can be performed using the related airworthiness standards. This way time dependent stress analysis can be carried out.
- The co-cured composite manufacturing technique can be applied to an actual structural part of METU TUAV, such as vertical or horizontal tail, and these structures can be manufactured in one piece eliminating the need for secondary bonding
- A detailed static and dynamic aeroelastic analysis can be performed based on the existing finite element model.
- Mechanical properties of woven fabric composite can be found using finite element techniques and compared with the existing results found from unit cell analysis. Also mechanical tests can be performed to verify these results.
- Failure analyses of the composite wing structure can be performed. Initial failure and progressive failure analyses can be performed in order to substantiate the residual strength of the wing.

REFERENCES

1. Federation of American Scientists web site,
“<http://www.fas.org/irp/program/collect/uav.htm>”, as accurate of 28 April, 2008
2. Unmanned Vehicle Systems International web site, “http://www.uvs-info.com/Yearbook2007/158_UAS_Categories-Tables-Figures.pdf”, as accurate of 28 April, 2008
3. Raymer, Daniel P., “*Aircraft Design: A Conceptual Approach*”, AIAA Education Series, 1992.
4. Niu, M. C. Y., “*Airframe Structural Design*”, Conmilit Press LTD., 1988
5. USAR Working Group 2005. *UAV Systems Airworthiness Requirements (USAR) Version 3*.
6. Anderson, J.D., “*Aircraft Performance and Design*”, McGraw-Hill, 1999
7. Turgut, T., “*Manufacturing and Structural Analysis of a Lightweight Sandwich Composite UAV Wing*”, 2007
8. Abbot, I. H. and Von Doenhoff, A. E., “*Theory of Wing Sections*”, Dover Publications Inc., 1959, pp.522.
9. Netcomposites web site,
“<http://www.netcomposites.com/education.asp?sequence=43>”, as accurate of 28 April, 2008.
10. Naik, N. K. and Shembekar, P. S., “*Elastic Behavior of Woven Fabric Composites: I-Lamina Analysis*”, Journal of Composite Materials, Vol. 26, No. 15, 1992, pp. 2196-2225.
11. Shang Zhong Sheng and Suong Van Hoa., “*Three Dimensional Micro-Mechanical Modeling of Woven Fabric Composites*”, Journal of Composite Materials, Vol. 35, No.19, 2001, pp. 1701-1729
12. L. Tong, A.P. Mouritz and M.K. Bannister, “*3D Fibre Reinforced Polymer Composites*”, Elsevier, 2002, pp. 70.

13. Levent Onal and Sabit Adanur., *“Modeling of Elastic, Thermal, and Strength/Failure Analysis of Two-Dimensional Woven Composites-A Review”*, Applied Mechanics Reviews, Vol. 60, January 2007, pp. 37-49
14. National Wiper web site,
“http://www.nationalwiper.com/tools_and_links/glossary/default.html”, as accurate of 28 April, 2008.
15. The A to Z of Materials web site,
“http://www.azom.com/details.asp?ArticleID=1091#_Plain_Weave”, as accurate of 28 April, 2008.
16. Halpin, J.C., Jerine, K. and Whitney, J.M., *“The Laminate Analogy for 2- and 3-Dimensional Composites”*, Journal of Composite Materials, 5:36-49, 1971
17. Ishikawa, T. and T.-W. Chou. 1983. *“One Dimensional Micromechanical Analysis of Woven Fabric Composites,”* AIAA Journal, 21(12):1714-1721.
18. Ishikawa, T. and T.-W. Chou. 1982. *“Stiffness and Strength Behavior of Woven Fabric Composites,”* Journal of Materials Science, 17:3211-3220
19. Ishikawa, T. 1981. *“Anti-Symmetric Elastic Properties of Composite Plates of Satin Weave Cloth,”* Fibre Science and Technology, 15:127-145.
20. Tsu-Wei Chou, *“Micro-structural Design of Fiber Composites”*, Cambridge University Press, 2005, pp. 302.
21. Falzon, P.J., Herzberg, I., and Karbhari, V.M., 1996, *“Effects of Compaction on the Stiffness and Strength of Plain Weave Fabric RTM Composites,”* Journal of Composites Materials, 30, pp. 1210-1247
22. B.N. Cox and M.S. Dadkhah, *“The Macroscopic Elasticity of 3D Woven Composites,”* J. Comp. Mater., 29, 795-819 (1995).
23. Hashin, Z., *“Theory of Fibre Reinforced Materials,”* CR-1974, NASA, 1972.
24. Hashin, Z., *“Analysis of Composite Materials-A Survey,”* J. Appl. Mech., 50:481, 1983.
25. Lekhnitskii, S. G., *“Theory of Elasticity of an Anisotropic Body”*, Moscow: MIR Publishers, 1981.
26. Department of Defense Handbook, *“Composite Materials Handbook, Volume 2: Polymer Matrix Composites Material Properties”*
27. Aydın, S., Yardımcı, M.Y., Ramyar, K., *“Mechanical Properties of Four Timber Species Commonly Used in Turkey,”* Turkish J. Eng. Env. Sci. 31:19-27, 2007.

28. Aerospatiale Aeronautique, Composite Stress Manual, Z10-1/3
29. MSC. Nastran - Basic Dynamics Analysis User's Guide, MSC Software Corporation
30. Bisplinghoff, R.L., Ashley, H. and Halfman, R.L., "Aeroelasticity", Dover Publications, pp. 421-434, 1996.
31. Theodorsen, T., "General Theory of Aerodynamic Instability and the Mechanism of Flutter", NACA Report 496, 1935.
32. Mahfuz, H., Majumdar, P., Saha, M., Shamery, F. and Jeelani, S., "Integral Manufacturing of Composite Skin-Stringer Assembly and Their Stability Analysis," *Applied Composite Materials* 11: 155-171, 2004.
33. Karal, M., "AST Composite Wing Program – An Executive Summary," CR-2001-210650-NASA, 2001.
34. Tatum, S., "VARTM Cuts Costs", *Reinforced Plastics* 45(5), May 2001, 22.

APPENDIX A

INTERPOLATION OF CFD DATA INTO FINITE ELEMENT MODEL

- **Creating the Geometry**

Geometry of the wing can be created using any CAD program from which the geometry can be exported in general file formats, such as STEP (Standard for the Exchange of Product), IGES (Initial Graphics Exchange Specification). In this study, CATIA V5 is used as CAD program. The edges and zones on which different mesh properties wanted can be defined in the CAD program therefore manipulation with the geometry in the next step (preprocessing the CFD mesh) can be skipped.

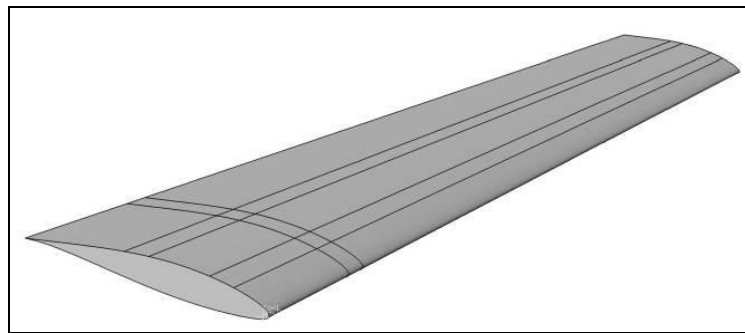


Figure 60: CAD model of the wing

It is observed that in most programs exporting the geometry in STEP file format gives better results than the other ones.

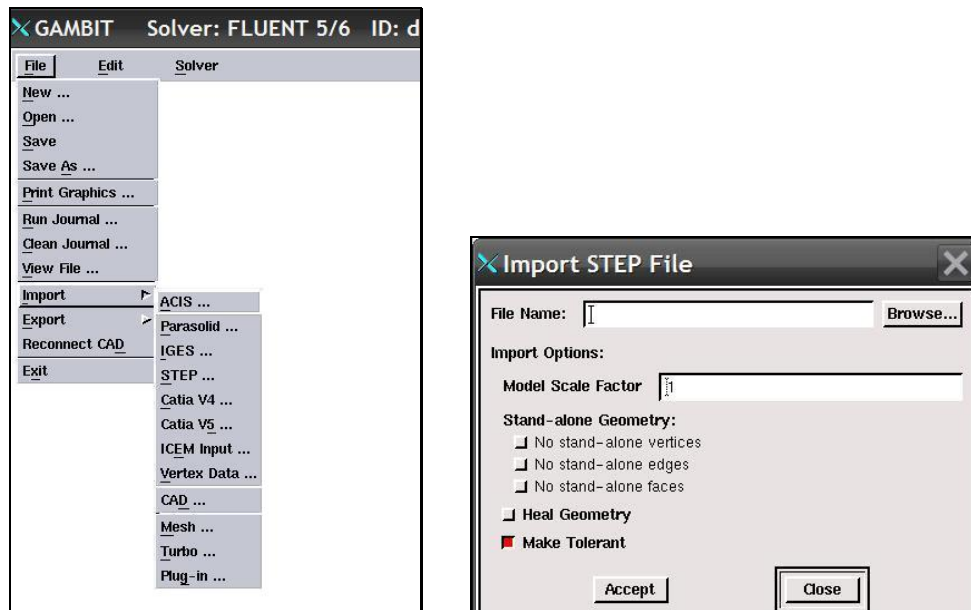
- **Creating the CFD Mesh Using GAMBIT**

In order to create the mesh that will be used in CFD solutions, a preprocessor GAMBIT is used. The first step in preprocessing is importing the geometry that was created in the CAD program.

In GAMBIT:

File → Import → STEP

Model Scale Factor= 0.001



(a)

(b)

Figure 61: STEP file importing in GAMBIT.

After importing the geometry, next step is to create the 3D solution domain. Solution domain may have different shapes such as rectangular prism, semi sphere etc. In this tutorial two nested rectangular prisms will be used as the solution domain. The inner domain will be much smaller (0.25%) than the outer domain but it will consist ten times more elements in it. The domain is nested in such a way because the pressure gradients are higher in the vicinity of the wing than the far zones.

In GAMBIT:

- Create the inner domain

Geometry → *Volume* → *Create Real Brick*

Width(X) = 3

Depth(Y) = 4

Height (Z) = 2

- Move the inner domain to its appropriate position

Geometry → *Volume* → *Move/Copy*

Global x = 0.5

Global y = -2

Global z = 0

- Create the outer domain

Geometry → *Volume* → *Create Real Brick*

Width(X) = 40

Depth(Y) = 15

Height (Z) = 16

- Move the outer domain to its appropriate position

Geometry → *Volume* → *Move/Copy*

Global x = 9

Global y = -7.5

Global z = 0

- Subtract the volumes from each other

Geometry → *Volume* → *Subtract*

Volume = volume3 (outer domain)

Subtract volume = volume2 (inner domain) while *retaining* the
volume2

Geometry → *Volume* → *Subtract*

Volume = volume2 (inner domain)

Subtract volume = volume1 (imported wing geometry)

- Clean the duplicate surfaces

Tools→ *Geometry Cleanup*→ *Clean Up Duplicate Surfaces*

Tolerance = Default

Update→ *Auto*

Creating edge meshes of the surface mesh on the wing is the next step. Note that, the following procedures may differ from geometry to geometry. Also computing power will determine how fine or coarse the mesh will be.

Mesh→ *Edge*→ *Edges* (select the edges of the wing)

Interval Size = 0.01

Mesh→ *Face*→ *Faces* (select the faces of the wing)

Elements = Tri

Type = Pave

Next step is creating the size functions and creating the volume mesh. The size functions will determine the growth rate of the volume mesh starting from the surface mesh. In the inner domain the growth will be smaller than the outer one since a finer mesh is wanted in the inner domain.

Tools→ *Size Function*→ *Create Size Function*

Type = Meshed

Faces = Wing Surface Faces

Volume = volume2 (inner domain)

Growth rate = 1.09

Mesh→ *Volume*→ *Volumes* (select the inner domain)

Elements = Tet/Hybrid

Type = TGrid

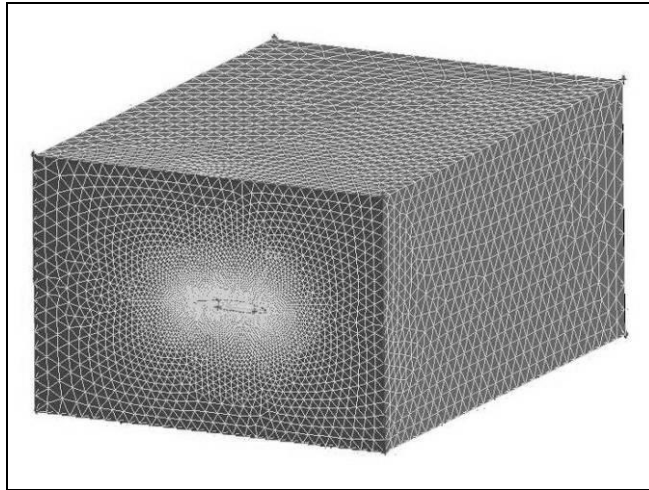


Figure 62: Inner CFD domain

Tools → *Size Function* → *Create Size Function*

Type = Meshed

Faces = Surfaces of the inner domain (5 surfaces)

Volume = volume3 (outer domain)

Growth rate = 1.2

Mesh → *Volume* → *Volumes (select the outer domain)*

Elements = Tet/Hybrid

Type = TGrid

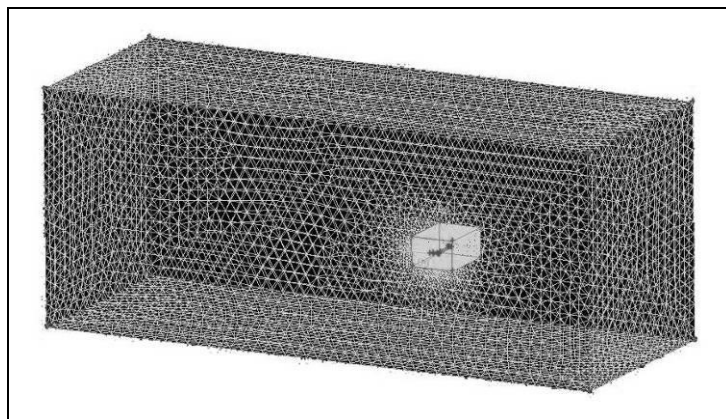


Figure 63: The whole CFD domain

The last step of the mesh generation will be defining the zones and boundary conditions.

Zones → *Specify Boundary Types*

- Select the wing surfaces and assign them WALL boundary condition
- Select the interfaces of inner domain and outer domain (5 surfaces) and assign them INTERIOR
- Assign other boundary conditions as shown in the figure below.

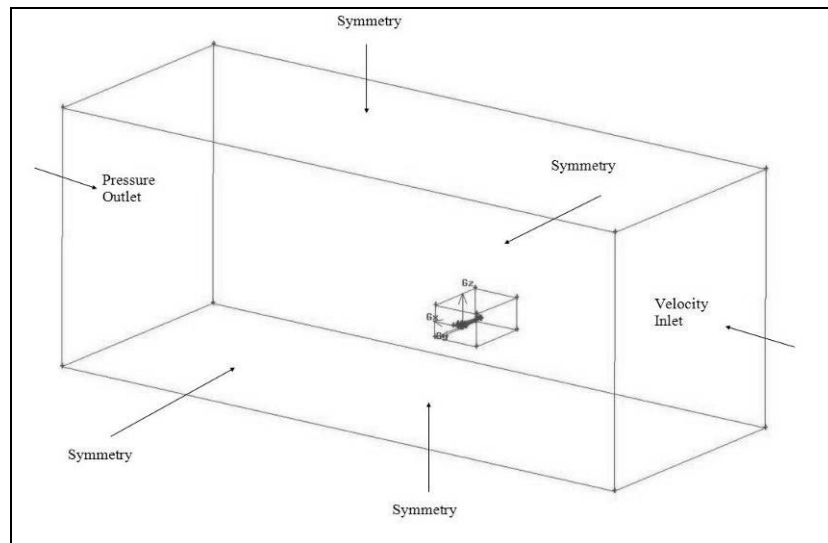


Figure 64: Boundary conditions for CFD analysis

Zones → *Specify Continuum Types*

Type = Fluid

Volumes = Select the inner and outer domains

Finally the resulting mesh can be exported.

File → *Export* → *Mesh*

- **Running the FLUENT Analysis**

Fluent → *Run* → *3D*

File → *Read* → *Case* → **.msh*

Grid → Check

Grid → Reorder → Domain

Define → Model → Solver

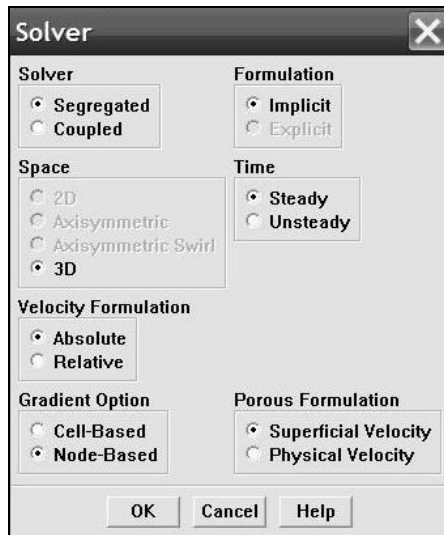


Figure 65: Selecting the solver properties in Fluent.

Define → Model → Viscous → Inviscid

Define → Boundary Conditions → Zone=Inlet → Type=Velocity Inlet

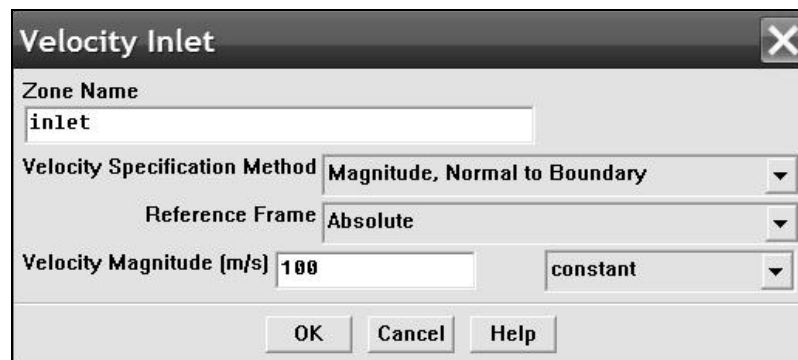


Figure 66: Velocity inlet boundary condition

Solve → Monitors → Residual Monitors

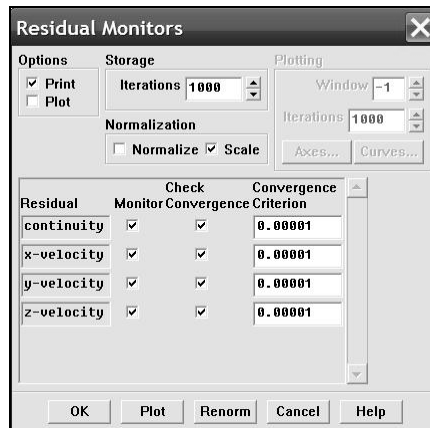


Figure 67: Opening the residual monitors

Solve → Controls → Solution Controls

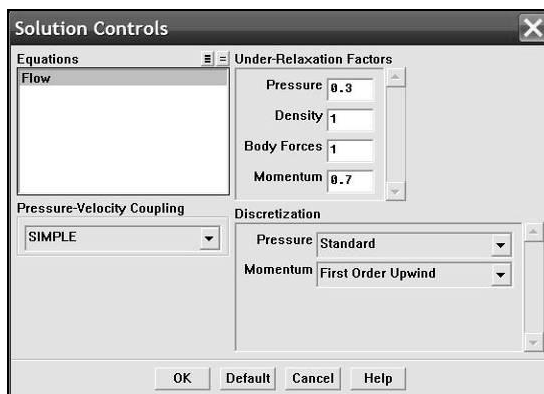


Figure 68: Solution control options

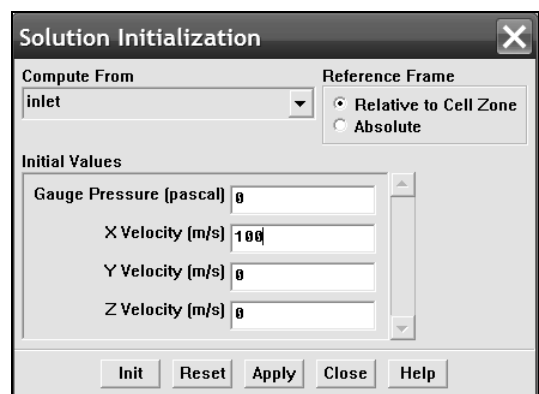


Figure 69: Solution initialization

Solve → Initialize → Init

Solve → Iterate

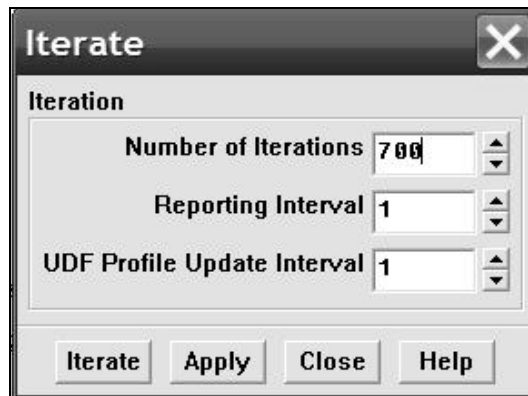


Figure 70: Starting the iteration process in Fluent

The iteration can be stopped after the residuals converged in first order upwind solution and the solution scheme can be changed to second order upwind solution for better accuracy. After the iterations are stopped, the nodal forces and corresponding surface meshes can be exported to Nastran.

- **Exporting the Nodal Forces**

So far, the CFD solution procedure in Gambit and Fluent is explained. In order to perform interpolation procedure a new volume mesh should be created. The surface meshes on wing surfaces should be created regarding the new FEM mesh that will be exported to FE program. The mesh intensity and properties should be chosen carefully keeping in mind the FE analysis. After creating new volume mesh from this surface mesh, it should be imported into Fluent. As explained in Chapter 3, the geometrical domains of the CFD solution mesh and new interpolation mesh should be identical.

First step is writing the interpolation data from CFD solution.

File → Interpolate → Write Data → Write

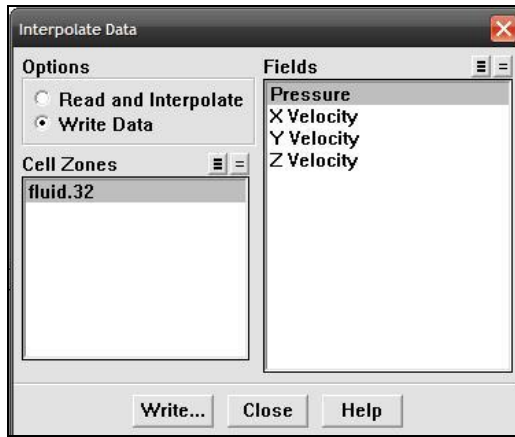


Figure 71: Writing the interpolation file

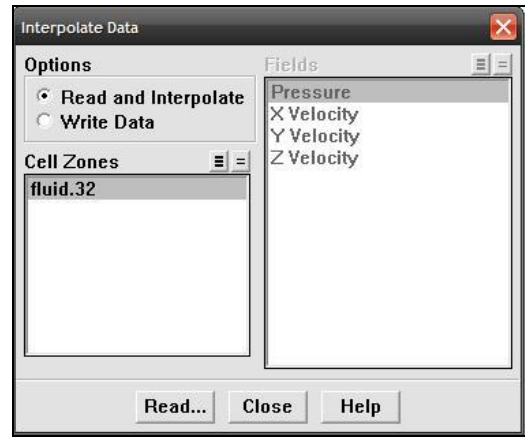


Figure 72: Reading the interpolation file

Next step is opening the new generated interpolation mesh which was created in Gambit and imported into Fluent.

In a new Fluent window:

File → Interpolate → Read and Interpolate → Read

Lastly the surface meshes which will form FE mesh are exported in Nastran *.bdf file.

File → Export

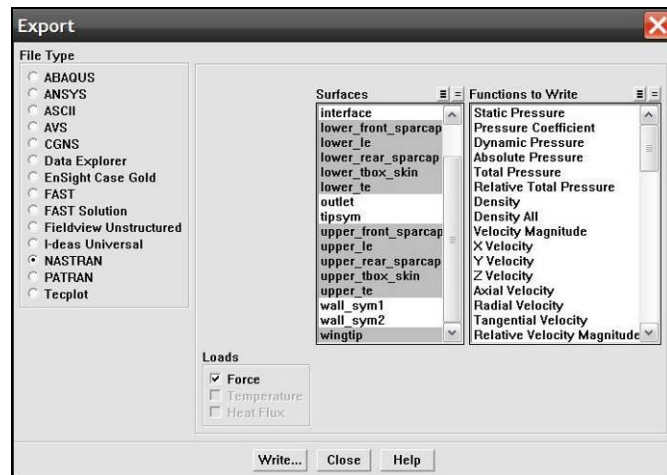


Figure 73: Exporting the CFD data to MSC.Patran/Nastran

The whole procedure is shown in a flow chart in Figure 74.

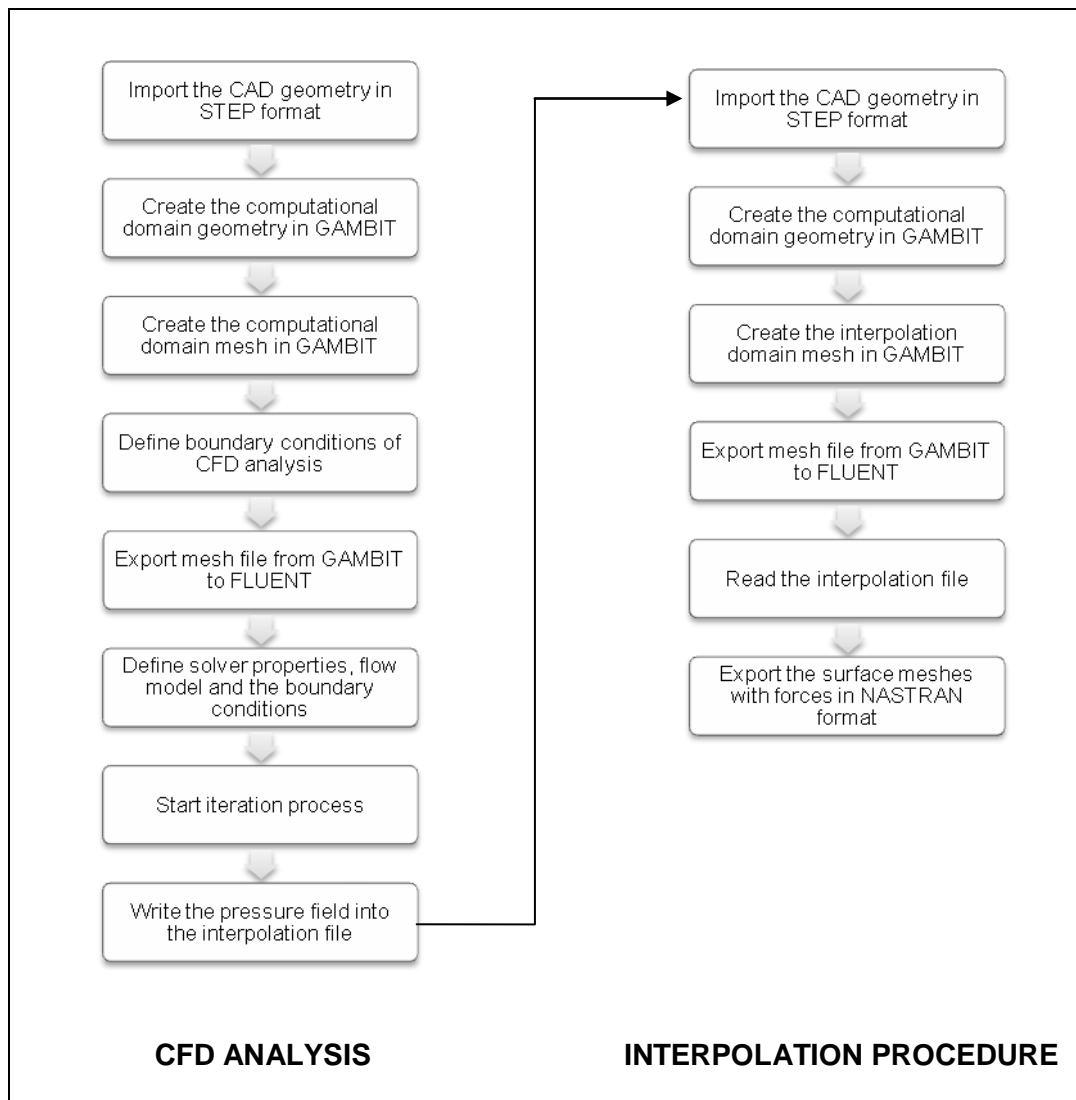


Figure 74: Flowchart of the procedure for interpolating CFD data into FE model